



Università degli Studi di Napoli *Federico II*

DOTTORATO DI RICERCA IN
FISICA FONDAMENTALE ED APPLICATA

Ciclo XXVII

Coordinatore: prof. Raffaele Velotta

Revealing Biomolecules Dynamics by UV Ultrafast Spectroscopy

Settore Scientifico Disciplinare FIS / 01

Dottorando
Mohammadhassan Valadan

Tutore
Prof. Raffaele Velotta

Anni 2012/2015

*To my wife, Mohadeseh,
and
to my parents and brother*

Acknowledgements

I wish to express my special appreciation and thanks to my advisor **Prof. Raffaele Velotta** for his kindness, patience, and precious advices. As well, I'd like to show my gratitude to **Prof. Carlo Altucci** for his notable guidance. Many thanks also to **Dr. Bartolomeo Della Ventura** and other colleagues in the Biophotonics Laboratory for their assistances.

I would like to extend thanks to **Prof. Majed Chergui**, for his kind hospitality and for the opportunity he provided me in the “Laboratory of Ultrafast Spectroscopy” at École polytechnique fédérale de Lausanne (EPFL) to perform experiments. Also I am thankful for valuable help of **Dr. Enrico Pomarico**, and other friends in LSU, EPFL.

Moreover, I thank **Dr. Roberto Improta** for his help in developing the theoretical model.

I must thank all of my friends that made Naples and this time a great experience. I'm thankful to all of them. Besides, there is a special thank for **Mr. Guido Celentano**.

I would also like to thank my parents and my brother for their love and support.

Most of all, I am grateful to my wife, **Mohadeseh Zandavifard**, for her endless love, kindness, and patience.

Contents

Acknowledgements	III
Contents	IV
Introduction	1
Chapter 1. Basic Concepts in Electronic Spectroscopy	4
1.1. Luminescence	6
1.2. Fluorescence, Phosphorescence and Electron Spin	7
1.3. Photoluminescent Energy Level Diagrams	8
1.4. UV-Visible Absorption Spectra	9
1.5. Absorbing species containing σ , π , and n electrons	12
1.5.1. $\sigma \rightarrow \sigma^*$ Transitions	12
1.5.2. $n \rightarrow \sigma^*$ Transitions	12
1.5.3. $n \rightarrow \pi^*$ and $\pi \rightarrow \pi^*$ Transitions	13
1.6. Absorption and Emission Rates	13
1.7. Deactivation Processes	14
1.7.1. Vibrational Relaxation	14
1.7.2. Internal Conversion	14
1.7.3. External Conversion	15
1.7.4. Intersystem Crossing	15
1.7.5. Phosphorescence	15
1.8. Variables that affect Fluorescence	16
1.8.1. Quantum Yield	16
1.8.2. Transition Types in Fluorescence	17

1.8.3. Fluorescence Quenching	17
1.9. Emission and Excitation Spectra	18
1.10. From Schrodinger equation to potential energy surface of molecules	20
1.10.1. Molecular modeling	23
1.10.2. Franck-Condon Principle	27
1.10.3. Conical Intersection	28
Chapter 2. Biomolecules and UV excitation	29
2.1. Excited-States in Biomolecules	30
2.2. Single-base excited states	32
2.2.1. Steady-State Experimental Absorption Spectra	35
2.2.2. Steady-State Experimental Fluorescence Spectra	36
2.2.3. Computed Fluorescence Spectra	37
2.2.4. Time-Resolved Fluorescence Experiments and Fluorescence Decay	39
2.2.5. Computed S_0 - S_1 Conical Intersection	41
2.3. Dark Excited States in Pyrimidines	44
2.3.1. $S_n\pi^*$ states	44
2.3.2. Triplets	46
2.4. 5-benzyluracil as the Model Systems for DNA-Protein Cross-Linking	46
Chapter 3. 5BU and 5,6BU Steady-State Measurements	48
3.1. Photocyclization of 5BU	49
3.2. Materials and methods for spectroscopy measurements	50
3.3. Molecular geometries in the ground state	51
3.4. Photophysical properties in the Frank Condon region	52
3.5. Optical characterization of the photocyclization process	53
3.6. Excited states decay channels	55
3.7. Fluorescence anisotropy and 5BU to 5,6BU transformation	56
3.8. Photocyclization Quantum Yield	57
3.9. Fluorescence Quantum Yield	60
3.10. Solvent Effect in Photocyclization	61

3.11.	<i>Global Picture for the Photophysics and Photochemistry of 5BU: Assignment of the experimental steady state spectra</i>	63
3.12.	<i>Excited State geometry optimizations</i>	66
Chapter 4.	<i>Time-resolved Measurements on 5BU</i>	69
4.1.	<i>Time-correlated single photon counting</i>	71
4.2.	<i>TCSPC technique</i>	72
4.2.1.	<i>Count Rates and Single Photon Statistics</i>	74
4.2.2.	<i>Timing Resolution</i>	76
4.2.3.	<i>Experimental Setup for Fluorescence Decay Measurements with TCSPC</i>	77
4.3.	<i>Deconvolution of fluorescence decay profiles</i>	78
4.4.	<i>Nanosecond-resolved fluorescence measurements via TCSPC on 5BU</i>	79
4.5.	<i>Analysis of the signal emitted by 5BU</i>	81
4.6.	<i>Fluorescence Up-Conversion</i>	83
4.7.	<i>Up-Conversion technique</i>	83
4.7.1.	<i>Sum frequency generation</i>	85
4.7.2.	<i>The up-conversion setup</i>	87
4.7.3.	<i>Femtosecond laser system</i>	88
4.7.4.	<i>Excitation and gate Beams</i>	89
4.7.5.	<i>Sample flow</i>	90
4.7.6.	<i>Emission collection and time-gating</i>	90
4.7.7.	<i>Data treatment</i>	91
4.7.8.	<i>Temporal Response of the setup</i>	92
4.8.	<i>Femtosecond-resolved fluorescence measurements via up-conversion technique on 5BU</i>	93
4.8.1.	<i>Sample preparation</i>	93
4.8.2.	<i>Experimental conditions</i>	93
4.8.3.	<i>Up-conversion results on 5BU</i>	94
4.8.4.	<i>Measurements of 5BU fluorescence lifetime at low concentration</i>	96
4.9.	<i>Interpretation of the Time-Resolved experiments</i>	98

Chapter 5.	<i>Temporal and Spectral Characterization of Femtosecond UV Pulses</i>	100
5.1.	<i>Femtosecond UV pulses</i>	101
5.2.	<i>Experimental setup</i>	103
5.3.	<i>Analysis of the results</i>	105
5.4.	<i>Pulse duration and chirp</i>	108
5.5.	<i>Spectral characterization</i>	111
5.6.	<i>Linear optical methods for characterization of femtosecond UV pulses</i>	113
	<i>Conclusions</i>	117
	<i>Bibliography</i>	119

Introduction

Establishing a stable covalent bond between proteins and nucleic acids, in molecular biology usually referred to as crosslinking, is a fundamental tool for the identification of the partners in the DNA-protein interaction, the latter being a vital biological process. Crosslinking with fs-UV lasers has been presented in the literature as a revolutionary technique to increase the otherwise low process yield of conventional methods based on chemical catalysts, conventional UV sources, or longer UV pulses. It is known that crosslinking induced in cells by ultrashort laser pulses has a twofold advantage over conventional methods: (i) it binds only species that are in proximity (“zero length” covalent bond) of the absorbed photons rather than favoring unspecific bonds amongst many possible species in the cell and (ii) it only takes place until the radiation is incident on the sample, thus paving the way for time-resolved studies of transient interactions. UV-based cross-link relies upon the large absorption cross section of DNA base in the UV region, although, good for our health, the probability for these photo-induced changes is not as big as the excitation rate since many of the photo-excited species will relax into the ground state in an ultrafast time scale, preventing any change or damage.

Using femtosecond lasers is a real step ahead to make the biomolecules photo-react in a reasonable amount, but they also offer the unique possibility for time-resolved

measurements thereby allowing the investigation of the basic mechanisms following the photo-activation. While irradiation with a relatively high intensity UV laser greatly increases the efficiency of protein-nucleic acid cross-linking, it is difficult, however, to investigate cross-linking in the presence of very complex molecules, namely DNA and protein, themselves. Therefore, in a reductionist approach, to mimic the bond formation between the DNA base and the nearby proteins the photocyclization in 5-Benzyluracil (5BU) has been proposed as a model system of crosslink reactions, in view of the simultaneous presence of the Uracil and Benzene playing the role of the DNA base and the aromatic residue of a protein, respectively.

In order to design an experiment aimed at the measurement of the dynamics of photocyclization, we studied the steady-state absorption and emission (fluorescence) properties of 5BU and 5,6-benzyluracil (5,6BU), the latter being produced by exposing 5BU to UV ultrashort laser pulses. We found that after some time we can assume that all 5BU is completely transformed into 5,6BU and modifications in the absorption and fluorescence spectrum, fluorescence anisotropy, fluorescence quantum yields, and excited state lifetimes are observed when 5BU is photocyclized thus becoming 5,6BU.

The high value of anisotropy in 5BU indicates that a large fraction of its fluorescence signal has a very short lifetime, in the range of few picoseconds; whereas in the case of 5,6BU, the main part of fluorescence has a much longer lifetime in the range of; few nanoseconds. The role of solvent is also studied in the photocyclization process and, in particular, we show that using water as the solvent, photocyclization rate is larger than that observed when methanol is used. Such a finding can be explained in terms of different configuration 5BU molecules assume in the solution, thereby providing hints on the paths leading to 5,6BU formation.

Time-resolved 5BU fluorescence has been measured in nanosecond and femtosecond regimes by "Time Correlated Single Photon Counting" and "Fluorescence up-conversion" techniques, respectively, finding a very good agreement with a theoretical model (Molecular dynamics modeling).

The results described so far allows one to design a possible experiment in which in a pump-probe scheme the photocyclization process can be followed in time. In such a setup an ultrashort UV laser pulse has to be split into two replica: One is used to trigger the interaction (excite the sample and start the photocyclization, for instance); the second pulse is then properly delayed to probe an optical observable like absorption or fluorescence, and

eventually monitor the reaction. Of course, laser pulse properties, especially the temporal characteristics, are then important in determining the time resolution of such experiments. A common technique to measure the temporal duration of ultrashort pulses is based on nonlinear phenomena such as second-harmonic-generation; one of the most used experimental schemes is based on noncollinear autocorrelation. Unfortunately, such an approach is not feasible in the UV frequency range because of no crystal allows light propagation in the deep UV. Thus, we used an alternative nonlinear process in autocorrelation measurements: an autocorrelator is set up based on Two-Photon Absorption (TPA). The TPA signal has been measured and the information on the pulse duration has been retrieved from the FWHM of the fitted function.

A deeper knowledge of the processes occurring in biomolecules and biological samples, as those reported in this thesis, might enable us to engineer them by preventing the undesirable ones or increasing the rate for the preferred routes.

Chapter 1

Basic Concepts in Electronic Spectroscopy

- 1.1. *Luminescence*
- 1.2. *Fluorescence, Phosphorescence and Electron Spin*
- 1.3. *Photoluminescent Energy Level Diagrams*
- 1.4. *UV-Visible Absorption Spectra*
- 1.5. *Absorbing species containing σ , π , and n electrons*
- 1.5.1. *$\sigma \rightarrow \sigma^*$ Transitions*
- 1.5.2. *$n \rightarrow \sigma^*$ Transitions*
- 1.5.3. *$n \rightarrow \pi^*$ and $\pi \rightarrow \pi^*$ Transitions*
- 1.6. *Absorption and Emission Rates*
- 1.7. *Deactivation Processes*
- 1.7.1. *Vibrational Relaxation*
- 1.7.2. *Internal Conversion*
- 1.7.3. *External Conversion*
- 1.7.4. *Intersystem Crossing*
- 1.7.5. *Phosphorescence*
- 1.8. *Variables that affect Fluorescence*
- 1.8.1. *Quantum Yield*
- 1.8.2. *Transition Types in Fluorescence*
- 1.8.3. *Fluorescence Quenching*
- 1.9. *Emission and Excitation Spectra*
- 1.10. *From Schrodinger equation to potential energy surface of molecules*
- 1.10.1. *Molecular modeling*
- 1.10.2. *Franck-Condon Principle*
- 1.10.3. *Conical Intersection*

1.1. Luminescence

Fluorescence and phosphorescence are types of molecular luminescence methods. A molecule of analyte absorbs a photon and excites a species. The emission spectrum can provide qualitative and quantitative analysis. The term fluorescence and phosphorescence are usually referred as photoluminescence because both are alike in excitation brought by absorption of a photon. Fluorescence differs from phosphorescence in that the electronic energy transition that is responsible for fluorescence does not change in electron spin, which results in short-lived electrons ($<10^{-5}$ s) in the excited state of fluorescence. In phosphorescence, there is a change in electron spin, which results in a longer lifetime of the excited state (second to minutes). Fluorescence and phosphorescence occurs at longer wavelength than the excitation radiation.

Fluorescence can occur in gaseous, liquid, and solid chemical systems. The simple kind of fluorescence is by dilute atomic vapors. A fluorescence example would be if a 3s electron of a vaporized sodium atom is excited to the 3p state by absorption of a radiation at wavelength 589.6 and 589.0 nm. After 10^{-8} s, the electron returns to ground state and on its return it emits radiation of the two wavelengths in all directions. This type of fluorescence in which the absorbed radiation is remitted without a change in frequency is known as resonance

fluorescence. Resonance fluorescence can also occur in molecular species. Molecular fluorescence band centers at wavelengths longer than resonance lines. The shift toward longer wavelength is referred to as the Stokes Shift [1].

1.2. Fluorescence, Phosphorescence and Electron Spin

Understanding the difference between fluorescence and phosphorescence requires the knowledge of electron spin and the differences between singlet and triplet states. The topics below lay out a general review of the rules and descriptions of electron spin and states.

The Pauli Exclusion Principle states that two electrons in an atom cannot have the same four quantum numbers (n, l, m_l, m_s) and only two electrons can occupy each orbital where they must have opposite spin states (spin pairing). Because of this spin pairing, most molecules do not exhibit a magnetic field and are diamagnetic. In diamagnetic molecules, electrons are not attracted or repelled by the static electric field. Free radicals are paramagnetic because they contain unpaired electrons have magnetic moments that are attracted to the magnetic field [1, 2].

Singlet and Triplet Excited State Singlet state is defined when all the electron spins are paired in the molecular electronic state and the electronic energy levels do not split when the molecule is exposed into a magnetic field. A doublet state occurs when there is an unpaired electron that gives two possible orientations when exposed in a magnetic field and imparts different energy to the system. A singlet or a triplet can form when one electron is excited to a higher energy level. In an excited singlet state, the electron is promoted in the same spin orientation as it was in the ground state (paired). In a triplet excited state, the electron that is promoted has the same spin orientation (parallel) to the other unpaired electron. The difference between the spins of ground singlet, excited singlet, and excited triplet is shown in Figure 1.1 Singlet, doublet and triplet is derived using the equation for multiplicity, $2S+1$, where S is the total spin angular momentum (sum of all the electron spins). Individual spins are denoted as spin up ($s = +1/2$) or spin down ($s = -1/2$). If we were to calculate the S for the excited singlet state, the equation would be $2(+1/2 + (-1/2))+1 = 1$, therefore making the center orbital in the figure a singlet state. If the spin multiplicity for the excited triplet state was calculated, we obtain $2(+1/2 + 1/2)+1 = 2(1)+1 = 3$, which gives a triplet state as expected.

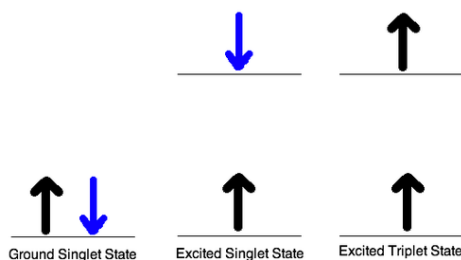


Figure 1.1: Spin in the ground and excited states

The difference between a molecule in the ground and excited state is that the electrons is diamagnetic in the ground state and paramagnetic in the triplet state. This difference in spin state makes the transition from singlet to triplet (or triplet to singlet) more improbable than the singlet-to-singlet transitions. This singlet to triplet (or reverse) transition involves a change in electronic state. For this reason, the lifetime of the triplet state is longer the singlet state by approximately 4 orders of magnitude. The radiation that induced the transition from ground to excited triplet state has a low probability of occurring, thus their absorption bands are less intense than singlet-singlet state absorption. The excited triplet state can be populated from the excited singlet state of certain molecules which results in phosphorescence. These spin multiplicities in ground and excited states can be used to explain transition in photoluminescence molecules by the Jablonski diagram [1, 2].

1.3. Photoluminescent Energy Level Diagrams

The Jablonski diagram that drawn below is a partial energy diagram that represents the energy of photoluminescent molecule in its different energy states. The lowest and darkest horizontal line represents the ground-state electronic energy of the molecule which is the singlet state labeled as S_0 . At room temperature, majority of the molecules in a solution are in this state.

There are numerous vibrational levels that can be associated with each electronic state as denoted by the thinner lines. Absorption transitions (red lines in Figure 1.2) can occur from the ground singlet electronic state (S_0) to various vibrational levels in the singlet excited vibrational states. It is unlikely that a transition from the ground singlet electronic state to the triplet electronic state because the electron spin is parallel to the spin in its ground state (Figure 1.1). This transition leads to a change in multiplicity and thus has a low probability of occurring which is a forbidden transition. Molecules also go through vibration relaxation to

lose any excess vibrational energy that remains when excited to the electronic states (S_1 and S_2) as demonstrated in orange in Figure 1.2. The knowledge of forbidden transition is used to explain and compare the peaks of absorption and emission [2].

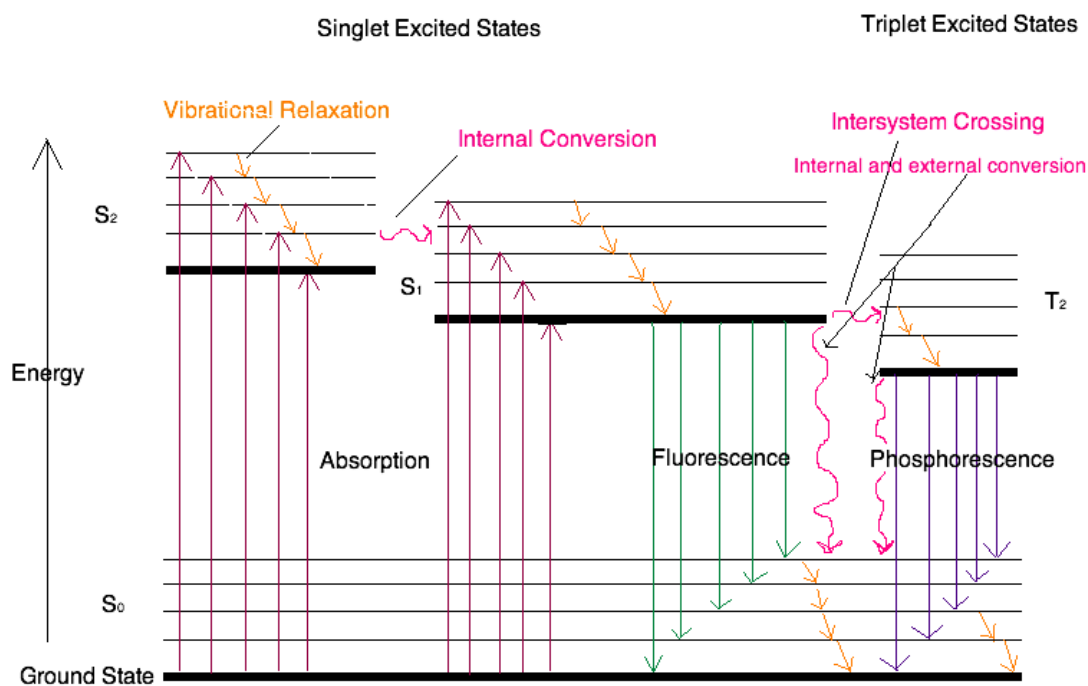


Figure 1.2: Partial Jablonski Diagram for Absorption, Fluorescence, and Phosphorescence: The upper lines represent the energy state of the three excited electronic states: S_1 and S_2 represent the electronic singlet state (left) and T_1 represents the first electronic triplet state (right). The upper darkest line represents the ground vibrational state of the three excited electronic state. The energy of the triplet state is lower than the energy of the corresponding singlet state.

1.4. UV-Visible Absorption Spectra

To understand why some compounds are colored and others are not we must make accurate measurements of light absorption at different wavelengths in and near the visible part of the spectrum. Commercial optical spectrometers enable such experiments to be conducted easily, and usually survey both the near ultraviolet and visible portions of the spectrum.

The visible region of the spectrum comprises photon energies of 36 to 72 kcal/mole (wavelength of about 400 to 800 nm), and the near ultraviolet region, to 200 nm, extends this

energy range to 143 kcal/mole. Ultraviolet radiation having wavelengths less than 200 nm is difficult to handle, and is seldom used as a routine tool for structural analysis.

The energies noted above are sufficient to promote or excite a molecular electron to a higher energy orbital. Consequently, absorption spectroscopy carried out in this region is sometimes called "electronic spectroscopy". Figure 1.3 is a diagram showing the various kinds of electronic excitation that may occur in organic molecules. Of the six transitions outlined, only the two lowest energy ones (left-most, colored blue) are achieved by the energies available in the 200 to 800 nm spectrum. As a rule, energetically favored electron promotion will be from the highest occupied molecular orbital (HOMO) to the lowest unoccupied molecular orbital (LUMO), and the resulting species is called an excited state.

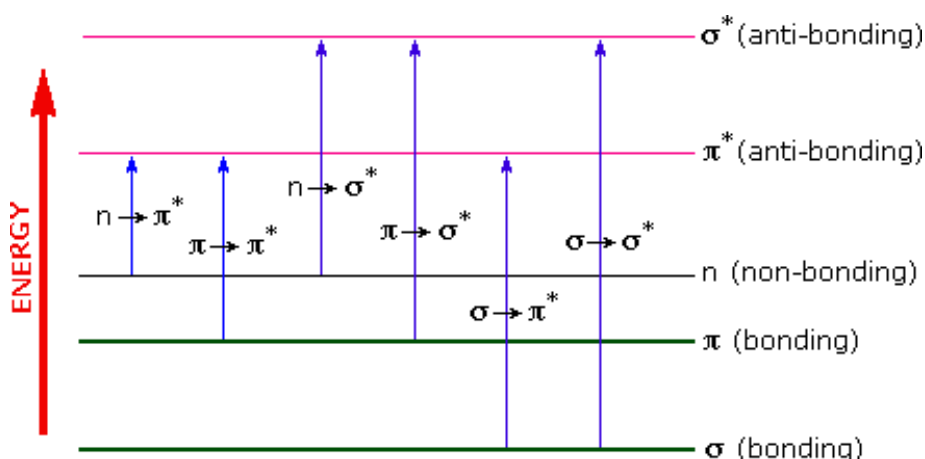


Figure 1.3: Different types of electronic excitation that may occur in organic molecules

When sample molecules are exposed to light having an energy that matches a possible electronic transition within the molecule, some of the light energy will be absorbed as the electron is promoted to a higher energy orbital. An optical spectrometer records the wavelengths at which absorption occurs, together with the degree of absorption at each wavelength. The resulting spectrum is presented as a graph of absorbance (A) versus wavelength. "Absorbance" usually ranges from 0 (no absorption) to 2 (99% absorption).

Because the absorbance of a sample will be proportional to the number of absorbing molecules in the spectrometer light beam (e.g. their molar concentration in the sample tube), it is necessary to correct the absorbance value for this and other operational factors if the spectra

of different compounds are to be compared in a meaningful way. The corrected absorption value is called "molar absorptivity", and is particularly useful when comparing the spectra of different compounds and determining the relative strength of light absorbing functions (chromophores). "Molar absorptivity" (ϵ) is defined as:

$$\epsilon = A / c l \quad (1.1)$$

where A = absorbance, c = sample concentration in moles/liter and l = length of light path through the sample in cm.

Indeed the entire vertical absorbance scale may be changed to a molar absorptivity scale once the information about the sample is in hand.

The only molecular moieties likely to absorb light in the 200 to 800 nm region, as some reported in Table 1.1, are π -electron functions and hetero atoms having non-bonding valence-shell electron pairs. Such light absorbing groups are referred to as chromophores. The oxygen non-bonding electrons in alcohols and ethers do not give rise to absorption above 160 nm. Consequently, pure alcohol and ether solvents may be used for spectroscopic studies.

Chromophore	Example	Excitation	λ_{\max} , nm	ϵ	Solvent
C=C	Ethene	$\pi \rightarrow \pi^*$	171	15,000	hexane
C \equiv C	1-Hexyne	$\pi \rightarrow \pi^*$	180	10,000	hexane
C=O	Ethanal	$n \rightarrow \pi^*$	290	15	hexane
		$\pi \rightarrow \pi^*$	180	10,000	hexane
N=O	Nitromethane	$n \rightarrow \pi^*$	275	17	ethanol
		$\pi \rightarrow \pi^*$	200	5,000	ethanol
C-X X=I	X=Br Methyl bromide	$n \rightarrow \sigma^*$	205	200	hexane
	Methyl Iodide	$n \rightarrow \sigma^*$	255	360	hexane

Table 1.1: Some typical "Molar absorptivity" values corresponding to different molecular orbital transitions

Molar absorptivities may be very large for strongly absorbing chromophores (>10,000) and very small if absorption is weak (10 to 100). The magnitude of ϵ reflects both the size of the chromophore and the probability that light of a given wavelength will be absorbed when it strikes the chromophore.

1.5. Absorbing species containing σ , π , and n electrons

Absorption of ultraviolet and visible radiation in organic molecules is restricted to certain functional groups (chromophores) that contain valence electrons of low excitation energy. The spectrum of a molecule containing these chromophores is complex. This is because the superposition of rotational and vibrational transitions on the electronic transitions gives a combination of overlapping lines. This appears as a continuous absorption band.

1.5.1. $\sigma \rightarrow \sigma^*$ Transitions

An electron in a bonding σ orbital is excited to the corresponding antibonding orbital. The energy required is large. For example, methane (which has only C-H bonds, and can only undergo $\sigma \rightarrow \sigma^*$ transitions) shows an absorbance maximum at 125 nm. Absorption maxima due to $\sigma \rightarrow \sigma^*$ transitions are not seen in typical UV-Vis. spectra (200 - 700 nm)

1.5.2. $n \rightarrow \sigma^*$ Transitions

Saturated compounds containing atoms with lone pairs (non-bonding electrons) are capable of $n \rightarrow \sigma^*$ transitions. These transitions usually need less energy than $\sigma \rightarrow \sigma^*$ transitions. They can be initiated by light whose wavelength is in the range 150 - 250 nm. The number of organic functional groups with $n \rightarrow \sigma^*$ peaks in the UV region is small.

1.5.3. $n \rightarrow \pi^*$ and $\pi \rightarrow \pi^*$ Transitions

Most absorption spectroscopy of organic compounds is based on transitions of n or π electrons to the π^* excited state. This is because the absorption peaks for these transitions fall in an experimentally convenient region of the spectrum (200 - 700 nm). These transitions need an unsaturated group in the molecule to provide the π electrons.

Molar absorptivities for $n \rightarrow \pi^*$ transitions are relatively low, and usually range from 10 to 100 $\text{L mol}^{-1} \text{cm}^{-1}$. On the other hand, $\pi \rightarrow \pi^*$ transitions normally give molar absorptivities between 1000 and 10,000 $\text{L mol}^{-1} \text{cm}^{-1}$.

1.6. Absorption and Emission Rates

Table 1.2 compares the absorption and emission rates of fluorescence and phosphorescence. The rate of photon absorption is very rapid. Fluorescence emission occurs at a slower rate. Since the triplet to singlet (or reverse) is a forbidden transition, meaning it is less likely to occur than the singlet-to-singlet transition, the rate of triplet to singlet is typically slower. Therefore, phosphorescence emission requires more time than fluorescence [2, 3].

Absorption/ Emission	Rate (seconds)	Comments
Photon Absorption	10^{-14} to 10^{-15}	Fast
Fluorescence emission	10^{-5} to 10^{-10}	Fast (singlet to singlet transition)
Phosphorescence Emission	10^{-4} to 10	Slow (forbidden transition)

Table 1.2: Comparison of Absorption and Emission Rates.

1.7. Deactivation Processes

A molecule that is excited can return to the ground state by several combinations of mechanical steps that will be described below and shown in Figure 1.2. The deactivation process of fluorescence and phosphorescence involve an emission of a photon radiation as shown by the straight arrow in Figure 1.2. The wavy arrows in this figure are deactivation processes without the use of radiation. The favored deactivation process is the route that is most rapid and spends less time in the excited state [2, 3].

1.7.1. Vibrational Relaxation

A molecule might be promoted to several vibrational levels during the electronic excitation process. Collision of molecules with the excited species and solvent leads to rapid energy transfer and a slight increase in temperature of the solvent. Vibrational relaxation is so rapid that the lifetime of a vibrational excited molecule ($<10^{-12}$) is less than the lifetime of the electronically excited state. For this reason, fluorescence from a solution always involves the transition from the lowest vibrational level of the excited state. Since the space of the emission lines are so close together, the transition of the vibrational relaxation can terminate in any vibrational level of the ground state.

1.7.2. Internal Conversion

Internal conversion is an intermolecular process of molecule that passes to a lower electronic state without the emission of radiation. It is a crossover of two states with the same multiplicity meaning singlet-to-singlet or triplet-to-triplet states. The internal conversion is more efficient when two electronic energy levels are close enough that two vibrational energy levels can overlap as shown in between S_1 and S_2 .

For some molecules, the vibrational levels of the ground state overlaps with the first excited electronic state, which leads to fast deactivation.

1.7.3. External Conversion

Deactivation of the excited electronic state may also involve the interaction and energy transfer between the excited state and the solvent or solute in a process called external conversion. Low temperature and high viscosity leads to enhanced fluorescence because they reduce the number of collision between molecules, thus slowing down the deactivation process.

1.7.4. Intersystem Crossing

Intersystem crossing is a process where there is a crossover between electronic states of different multiplicity as demonstrated in the singlet state to a triplet state (S_1 to T_1) in the Figure 1.2. The probability of intersystem crossing is enhanced if the vibration levels of the two states overlap. Intersystem crossing is most commonly observed with molecules that contain heavy atom such as iodine or bromine. The spin and orbital interaction increase and the spin become more favorable. Paramagnetic species also enhances intersystem crossing, which consequently decreases fluorescence.

1.7.5. Phosphorescence

Deactivation of the electronic excited state is also involved in phosphorescence. After the molecule transitions through intersystem crossing to the triplet state, further deactivation occurs through internal or external conversion or phosphorescence. In phosphorescence, the excited state lifetime is inversely proportional to the probability that the molecule will transition back to the ground state. Since the lifetime of the molecule in the triplet state is large (10^{-4} to 10 second or more), transition is less probable which suggest that it will persist for some time even after irradiation has stopped. Since the external and internal conversion compete so effectively with phosphorescence, the molecule has to be observed at lower temperature in highly viscous media to protect the triplet state.

1.8. Variables that affect Fluorescence

After discussing all the possible deactivation processes, we review the variables that affect the emissions to occur. Molecular structure and its chemical environment influence and determine whether a substance will fluoresce and how much intense are these emissions.

1.8.1. Quantum Yield

The quantum yield or quantum efficiency is used to measure the probability that a molecule will fluoresce or phosphoresce. For fluorescence and phosphorescence is the ratio of the number of molecules that luminescent to the total number of excited molecules. For highly fluoresce molecules, the quantum efficiency approaches to one. Molecules that do not fluoresce have quantum efficiencies that approach to zero.

Fluorescence quantum yield (ϕ) for a compound is determined by the relative rate constants (k) of various deactivation processes by which the lowest excited singlet state is deactivated to the ground state. The deactivation processes including fluorescence (k_f), intersystem crossing (k_i), internal conversion (k_{ic}), predissociation (k_{pd}), dissociation (k_d), and external conversion (k_{ec}) allows one to qualitatively interpret the structural and environmental factors that influence the intensity of the fluorescence. They are related by the quantum yield equation:

$$\phi = \frac{k_f}{k_f + k_i + k_{ec} + k_{ic} + k_{pd} + k_d} \quad (1.2)$$

Using this equation as an example to explain fluorescence, a high fluorescence rate (k_f) value and low values of the all the other relative rate constant terms ($k_f + k_i + k_{ec} + k_{ic} + k_{pd} + k_d$) will give a large ϕ , which suggest that fluorescence is enhanced. The magnitude of k_f , k_d , and k_{pd} depend on the chemical structure, while the rest of the constants k_i , k_{ec} , and k_{ic} are strongly influenced by the environment [1, 2, 3].

1.8.2. Transition Types in Fluorescence

Fluorescence rarely results from absorption of ultraviolet radiation of wavelength shorter than 250 nm because radiation at this wavelength has sufficient energy to deactivate the electron in the excited state by predissociation or dissociation. The bond of some organic molecules would rupture at 140 kcal/mol, which corresponds to 200-nm of radiation. For this reason, $\sigma \rightarrow \sigma^*$ transition in fluorescence are rarely observed. Instead, emissions from the less energetic transition will occur which are either $\pi^* \rightarrow \pi$ or $\pi^* \rightarrow n$ transition.

Molecules that are excited electronically will return to the lowest excited state by rapid vibrational relaxation and internal conversion, which produces no radiation emission. Fluorescence arises from a transition from the lowest vibrational level of the first excited electronic state to one of the vibrational levels in the electronic ground state. In most fluorescent compounds, radiation is produced by a $\pi^* \rightarrow \pi$ or $\pi^* \rightarrow n$ transition depending on which requires the least energy for the transition to occur.

Fluorescence is most commonly found in compounds in which the lowest energy transition is $\pi \rightarrow \pi^*$ (excited singlet state) than $n \rightarrow \pi^*$ which suggest that the quantum efficiency is greater for $\pi \rightarrow \pi^*$ transitions. The reason for this is that the molar absorptivity, which measures the probability that a transition will occur, of the $\pi \rightarrow \pi^*$ transition is 100 to 1000 fold greater than $n \rightarrow \pi^*$ process. The lifetime of $\pi \rightarrow \pi^*$ (10^{-7} to 10^{-9} s) is shorter than the lifetime of $n \rightarrow \pi^*$ (10^{-5} to 10^{-7}) [2].

1.8.3. Fluorescence Quenching

The intensity of fluorescence can be decreased by a wide variety of processes. Such decreases in intensity are called quenching. Quenching can occur by different mechanisms. Collisional quenching occurs when the excited-state fluorophore is deactivated upon contact with some other molecule in solution, which is called the quencher. In the case of Collisional quenching, the fluorophore is returned to the ground state during a diffusive encounter with the quencher. The molecules are not chemically altered in the process [3].

A wide variety of molecules can act as collisional quenchers. Examples include oxygen, halogens, amines, and electron-deficient molecules like acrylamide. The mechanism of quenching varies with the fluorophore–quencher pair. For instance, quenching of indole by

acrylamide is probably due to electron transfer from indole to acrylamide, which does not occur in the ground state. Quenching by halogen and heavy atoms occurs due to spin-orbit coupling and intersystem crossing to the triplet state.

Aside from collisional quenching, fluorescence quenching can occur by a variety of other processes. Fluorophores can form nonfluorescent complexes with quenchers. This process is referred to as static quenching since it occurs in the ground state and does not rely on diffusion or molecular collisions. Quenching can also occur by a variety of trivial, i.e., non-molecular mechanisms, such as attenuation of the incident light by the fluorophore itself or other absorbing species.

1.9. Emission and Excitation Spectra

One of the ways to visually distinguish the difference between each photoluminescence is to compare the relative intensities of emission/excitation at each wavelength. An example of the three types of photoluminescence (absorption, fluorescence and phosphorescence) is shown for phenanthrene in the spectrum shown in figure 1.4; In the spectrum, the luminescent intensity is measure in a wavelength is fixed while the excitation wavelength is varied. The spectrum in red represents the excitation spectrum, which is identical to the absorption spectrum because in order to fluorescence emission to occur, radiation needs to be absorbed to create an excited state. The spectrum in blue represent fluorescence and green spectrum represents the phosphorescence [3].

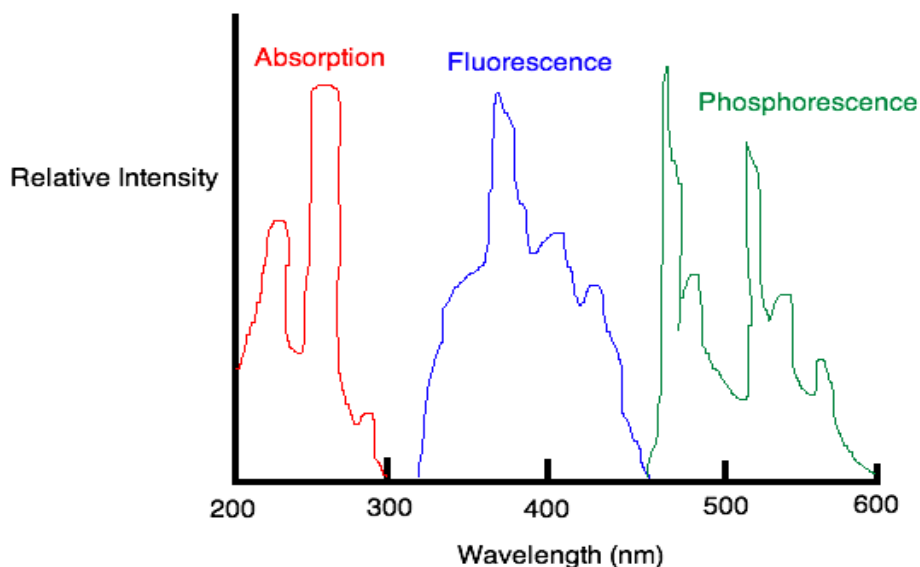


Figure 1.4: Wavelength Intensities of Absorption, Fluorescence, and Phosphorescence

Fluorescence and Phosphorescence occur at wavelengths that are longer than their absorption wavelengths. Phosphorescence bands are found at a longer wavelength than fluorescence band because the excited triplet state is lower in energy than the singlet state. The difference in wavelength could also be used to measure the energy difference between the singlet and triplet state of the molecule.

Figure 1.5 is a schematic of a typical fluorimeter that uses a source beam for fluorescence excitation and a pair of photomultiplier tubes as detectors. The source beam is split near the source into a reference beam and a sample beam. The reference beam is attenuated by the aperture disk so that its intensity is roughly the same as the fluorescence intensity. Both beams pass through the primary filter or monochromator, with the reference beam being reflected to the reference photomultiplier tube. The sample beam is focused on the sample by lenses and causes fluorescence emission. The emitted radiation passes through a second filter/monochromator and then is focused on the sample photomultiplier tube. The electrical outputs from the two transducers are then processed by an analog to digital converter to compute the ratio of the sample to reference intensities, which can then be used for qualitative and quantitative analysis. To obtain an emission spectrum, the excitation monochromator is fixed and the emission monochromator varies. To obtain an excitation spectrum, the excitation monochromator varies while the emission monochromator is fixed.

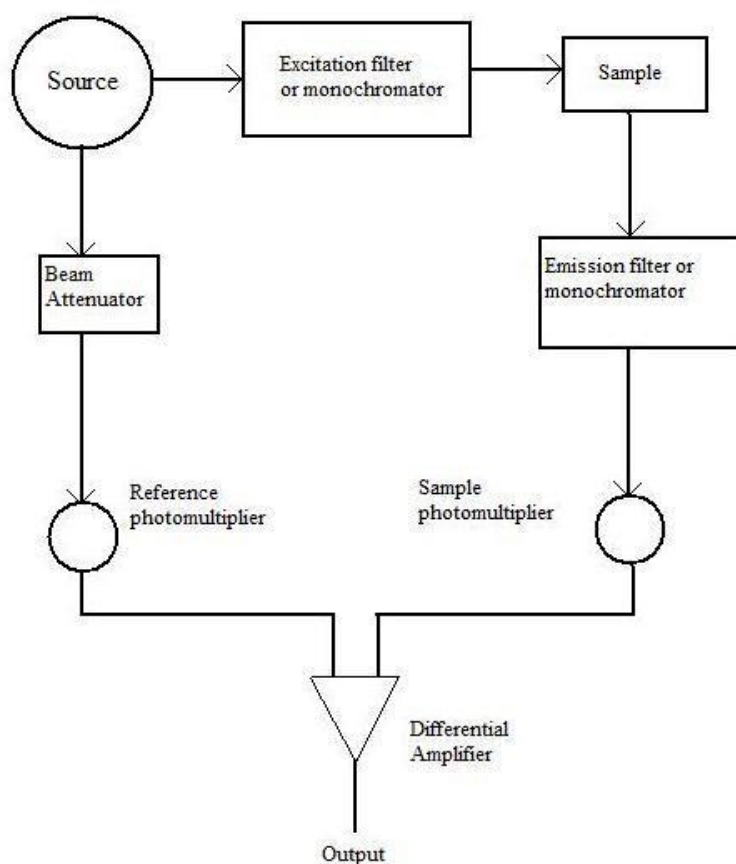


Figure 1.5: Schematic of Fluorescence Spectrometer

1.10. From Schrodinger equation to potential energy surface of molecules

Recent advances in time-resolved spectroscopic techniques have provided fundamental insights about the photophysical behavior of complex molecules in solution. These can be nicely completed and understood by means of ab initio computer simulations techniques, a powerful tool allowing to describe the characterization of molecular systems properties at the atomistic level via the numerical integration of the molecular Schrodinger equation. The basic concepts and fundamental equations necessary to describe a molecular system at the ab initio level will be reviewed in this section in order to briefly discuss the results obtained on the 5BU using these methods [4, 5].

In the following, the attention will be focused on situations in which atoms can be considered as made of charged pointlike quantum particles, nuclei and electrons, and are sufficiently close to form stable molecules. Let us consider hence the general molecule composed of N_N atoms, the Cartesian coordinates and momenta of the N_e electrons will be denoted as $(\mathbf{r}_j, \mathbf{p}_j)$ and of the N_N nuclei as $(\mathbf{R}_n, \mathbf{P}_n)$. The Hamiltonian operator of such a molecule has the form:

$$\hat{H}_{mol} = \hat{T}_N + \hat{T}_e + \hat{W}_{ee} + \hat{V}_{eN} + \hat{V}_{NN} \quad (1.3)$$

in which T_e is the kinetic energy of the electrons, T_N is the kinetic energy of the nuclei, and the other terms in the Hamiltonian take into account for the Coulomb interactions between all the particles: W_{ee} is the pair repulsive interaction between electrons, V_{NN} between nuclei and V_{eN} is the attractive interaction between electrons and nuclei.

Within this model, all the quantum mechanical stationary properties of a molecule can be extracted from the solution of the time-independent Schrodinger equation

$$\hat{H}_{mol} \Psi_n(r, \sigma, R) = \mathcal{E}_n \Psi_n(r, \sigma, R) \quad (1.4)$$

and its time dependent version

$$i\hbar \frac{\partial}{\partial t} \Psi(r, \sigma, R, t) = \hat{H}_{mol} \Psi_0(r, \sigma, R, t) \quad (1.5)$$

where the multi-index notation $r \equiv (\mathbf{r}_1, \dots, \mathbf{r}_{N_e})$, $\sigma \equiv (\sigma_1, \dots, \sigma_{N_e})$, $R \equiv (\mathbf{R}_1, \dots, \mathbf{R}_{N_N})$ for the electrons coordinates, electrons spin and nuclei coordinates has respectively been used.

Addressing the direct solution of Eq. (1.5), is a task far too complex in almost all practical cases but the adiabatic approximation can be used to simplify much the problem: the large mass difference between electrons and nuclei $\left(\frac{m_e}{M_n} < 10^{-3}\right)$ implies that the electronic degrees of freedom can be considered, with a good level of accuracy, to be able to respond almost instantaneously to the changes in the nuclear configuration. This approximation efficiently allows, in many situations, to separate adiabatically the motion of these two molecular subsystems.

To see how this works it is convenient to define the so called electronic Hamiltonian:

$$\hat{H}_{el}(r; R) = \hat{H}_{mol} - \hat{T}_N - \hat{V}_{NN} = \hat{T}_e + \hat{W}_{ee} + \hat{V}_{eN}(R) \quad (1.6)$$

in which the dependence on the nuclear coordinates is just carried parametrically in the external potential operator $\hat{V}_{eN}(R)$. The eigenfunctions corresponding to this operator are called adiabatic electronic states and are also parametrically dependent on the nuclear coordinates. Leaving aside the electron's spin, these states can hence be defined as

$$\hat{H}_{el}(r; R)\phi_n(r; R) = E_n(R) \phi_n(r; R) \quad (1.7)$$

The set of functions $\{\phi_n(r; R)\}_{n \in \mathbb{N}}$ is a complete basis in the electronic Hilbert space for every given molecular nuclear configuration that for every molecular system can be chosen to be real without loss of generality. Hence the molecular wave function can be expanded in this basis set as follows:

$$\Psi(r, R) = \sum_n \chi_n(R) \phi_n(r; R) \quad (1.8)$$

The adiabatic approximation can be now used to neglect all the terms involving the derivative of adiabatic states with respect to the nuclear coordinates:

$$\frac{\partial}{\partial R} \phi_n(r; R) \simeq 0 \quad (1.9)$$

this is in fact true in all the cases in which the electrons can be assumed to be moving so fast compared to the nuclei to see them almost frozen. In this case a standard form of the stationary Schrodinger equation can be derived

$$i\hbar \frac{\partial}{\partial t} \chi_n(R, t) = \hat{H}_n \chi_n(R) \quad (1.10)$$

in which

$$\hat{H}_n = T_N + E_n \quad (1.11)$$

and the function $E_n(R)$, an hypersurface in the space of nuclear coordinates, plays the role of potential energy surface (PES) on the which the nuclear motion is located.

So, within the adiabatic approximation, the nuclear and electronic degrees of freedom are decoupled. A suitable (numerical) solution of Eq. 1.7 represents the first ingredient to address the full molecular problem. The Density Functional Theory approach to solve the electronic problem will be briefly reviewed in next subsection. Then, assuming the knowledge of electronic adiabatic states as known quantities, the computational methods used to address equation 3 will be discussed.

1.10.1. Molecular modeling

Much chemical information about the behavior of a given molecular system can be extracted without really solving eq. 1.10 but just analyzing the characteristics of a given state PES. In this section some of these fundamental chemical and physical quantities will be derived and discussed assuming to have somehow acquired the knowledge of all necessary adiabatic PESs. To this end it is convenient to define the gradient of the PES as

$$\nabla U_n^{(ad)}(R) \equiv \left\{ \frac{\partial}{\partial R_1} U_n^{(ad)}(R), \dots, \frac{\partial}{\partial R_{3N_N}} U_n^{(ad)}(R) \right\} \quad (1.11)$$

The negative of this vector points in the direction of the steepest descent of the PES and corresponds to the force acting on a classical particle in the PES. Another quantity of primary interest is the $3N_N \times 3N_N$ force constant matrix, or Hessian matrix, the elements of which are defined as

$$K_{ab} \equiv \frac{\partial^2 U_n^{(ad)}(R)}{\partial R_a \partial R_b} \quad \{a, b = 1, \dots, 3N_N\} \quad (1.12)$$

The points R^* in the nuclear configurational space for which the gradient of a given PES vanishes

$$\nabla U_n^{(ad)}(R) \Big|_{R=R^*} = 0 \quad (1.13)$$

are called *stationary* points. The problem of the search of stationary points for a given real multivariable function via iterative methods has a long history going back to Newton and

Gauss. Many efficient numerical algorithms are available nowadays to locate stationary points of PESs with many degrees of freedom. These algorithms use as input parameters:

- An initial guess point in the nuclear configurational space (i.e. a starting nuclear structure)
- The PES value at each iteration step
- The PES gradient and hessian matrix (or some its approximated form, due to the big computational effort required for its calculation on every intermediate step).

Stable states of molecular systems correspond to global and local minima on their ground state PES. As explicative example a diatomic molecule can be taken in consideration. In Figure 1.6.a is reported a typical ground state PES as function of the bond length in a diatomic molecule. The minimum of $U_0(R)$ at R_{eq} gives the equilibrium distance between the two atoms. As a consequence of the quantum mechanical zero-point energy motion, the lowest possible energy of the molecule is above the bottom of the potential minimum of a quantity corresponding to the lowest nuclear bound state energy in this potential. The molecule is said to be stable if the difference between this zero-point energy and the energy of the separate atoms, $U_0(\infty)$, is finite. This energy is called dissociation energy (D_0 in Figure 1.6.a).

For polyatomic molecules the presence of multiple minima on the ground state PES is often encountered. These minima in $U_0(R)$ correspond to different isomers of the given molecule¹. To change isomeric form, the molecule has to pass a maximum of the potential curve that corresponds to a saddle point of $U_0(R)$ in which the Hessian matrix will have just one negative eigenvalue. These points are called *transition states*. A standard example of such situation is the umbrella vibration of NH_3 but more generally, it happens for every molecule in which intramolecular hydrogen transfer are possible.

Once the two minima of the ground state PES, that can be conveniently identified as A and B, have been found, in order to learn more about the path of an isomerization reaction, the PES values along possible paths connecting the two stable states can be investigated. For polyatomic molecules it is of course not desirable (and not computationally feasible) to compute the PES as a function of all internal coordinates. Quite often however only a few coordinates are important to describe the reaction. Then it becomes possible to take into

¹ the case of a chemical reaction involving more than one molecule is equivalent to this case if the coordinates of all the molecules involved are taken in consideration

account only the motion along a set of so called *reaction coordinates* ξ_i , a set of functions of the nuclear coordinates

$$\xi_i = \xi_i(R) \quad (18)$$

by means of which the states A and B are unambiguously identified by two distinct values of the reaction coordinates ξ_i , namely $\xi_i(A)$ and $\xi_i(B)$. The *minimum energy path* connecting the states A and B, the minimum potential barrier to be crossed and its associated transition state can be then for example identified by means of a set of constrained stationary point search aimed at reconstructing the function

$$\tilde{U}_0^{(ad)}(\lambda_i) \equiv \min_{\xi_i(R)=\lambda_i} U_0^{(ad)}(R) \quad \lambda_i \in \{\xi_i(A), \xi_i(B)\} \quad (1.14)$$

As explicative example in Figure 1.6.b is reported the case in which a one dimensional reaction coordinate is taken into account.

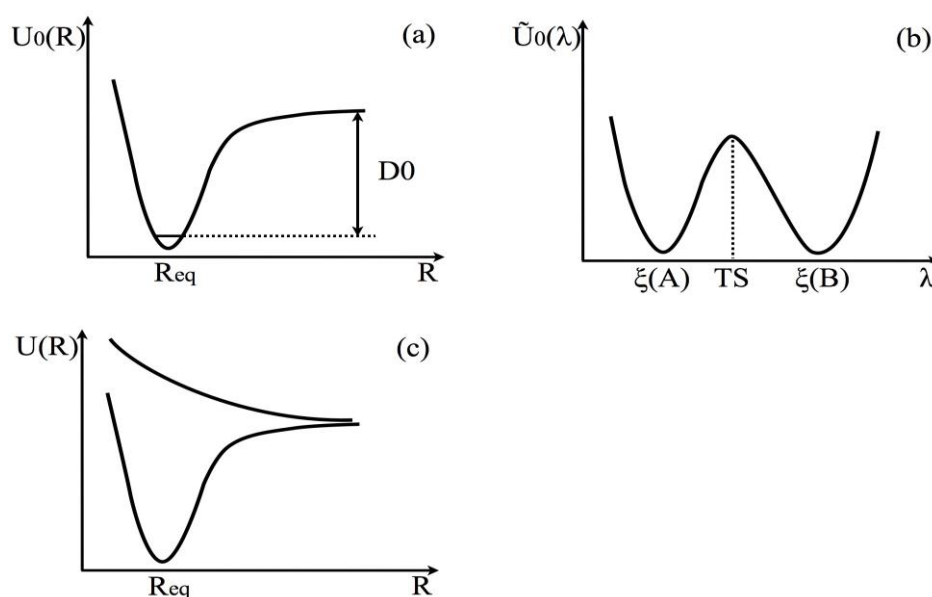


Figure 1.6: Schematic view of typical PESs for some explicative cases are reported in the different panels. In (a) the ground state PES of a diatomic molecule is depicted: R is the bond distance, R_{eq} the equilibrium distance between the two atoms and D_0 the dissociation energy. In (b) is taken in consideration a typical case in which a one dimensional reaction coordinate is taken into account to characterize an isomerization reaction; in (c) a typical case for ground and first excited state PESs of a diatomic molecule is reported. If the molecule is excited on the first electronic adiabatic state, for example, upon interaction with of an external light field, dissociation can occur.

Finally, a case typically encountered when excited states PESs are considered can be mentioned. In Figure 1.6.c is schematically reported the ground state and a possible excited adiabatic PESs for a diatomic molecule as function of the atoms bond length. In this case the excited state PES has no minimum. This implies that if the nuclei, e.g. after the absorption of a photon, start to “ride” the excited surface, the molecule will simply dissociate (photodissociation).

When case in which a sample of molecules is shined with light of frequency resonant with the excitation frequencies $\Omega_n(R)$ in regions of the nuclear configurational space corresponding to some stable nuclear state, electronic transitions from the ground state PES to the excited PES $E_n(R)$ can possibly occur. The large mass difference between electrons and nuclei can be used also in this case to consider the dynamic time scale of such electronic transitions very fast compared to the nuclear motion time scale. It means that the nuclear coordinates and momenta changes involved during the time of an electronic transition can be, with good approximation, disregarded. Referring to the explicative cartoon reported in Figure 1.7 this implies that the electronic transitions are *vertical* and the nuclei are frozen during the excitation process. This scheme for the description of electronic optical transitions is known as *Frank-Condon principle* and the form Frank-Condon region is usually used to refer the excited PES in the vicinity of a stable nuclear configuration.

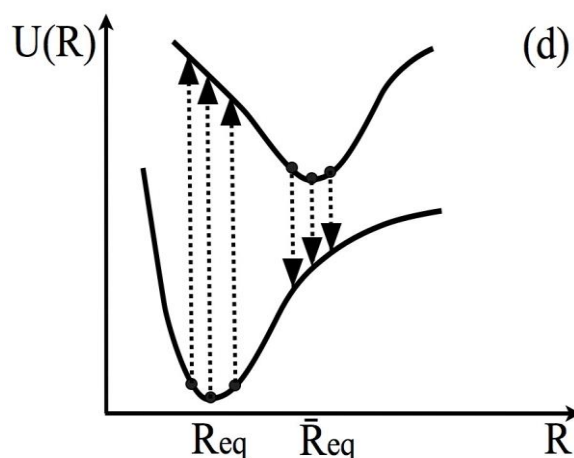


Figure 1.7: Scheme relative to the case in which a biatomic molecule is excited on the first electronic adiabatic state, for example, upon interaction with of an external light field. Different possible vertical transition are shown from the ground state to the first excited (absorption) and vice versa (fluorescence) as possible excitation and de-excitation events corresponding to different nuclear bond distances.

1.10.2. Franck-Condon Principle

The Franck-Condon Principle describes the intensities of vibronic transitions, or the absorption or emission of a photon. It states that when a molecule is undergoing an electronic transition, such as ionization, the nuclear configuration of the molecule experiences no significant change. This is due in fact that nuclei are much more massive than electrons and the electronic transition takes place faster than the nuclei can respond. When the nucleus realigns itself with the new electronic configuration, the theory states that it must undergo a vibration change [4, 5].

The nucleus in a molecule has Coulombic forces acting on it from the electrons and other nuclei of the system. Once a molecule undergoes the electronic transition, the resulting Coulombic forces serve to change the energy of the molecule. This change brings it from the ground state to an excited state and results in the nuclei changing its vibrational state. This vibrational structure of an electronic transition shows that the absorption spectrum consists of many lines instead of a single sharp electronic absorption line.

In other words, according to the Born–Oppenheimer approximation, the motions of electrons are much more rapid than those of the nuclei (i.e. the molecular vibrations). Promotion of an electron to an antibonding molecular orbital upon excitation takes about 10^{-15} s, which is very quick compared to the characteristic time for molecular vibrations (10^{-10} – 10^{-12} s). This observation is the basis of the Franck–Condon principle: an electronic transition is most likely to occur without changes in the positions of the nuclei in the molecular entity and its environment. The resulting state is called a Franck–Condon state, and the transition is called vertical transition, as illustrated by the energy diagram of Figure 1.8 in which the potential energy curve as a function of the nuclear configuration (internuclear distance in the case of a diatomic molecule) is represented.

The IUPAC definition is as follows: The Franck-Condon Principle has both a Classical and Quantum application. Classically, the Franck–Condon principle is the approximation that an electronic transition is most likely to occur without changes in the positions of the nuclei in the molecular entity and its environment. The resulting state is called a Franck–Condon state, and the transition involved, a vertical transition. The quantum mechanical formulation of this principle is that the intensity of a vibronic transition is proportional to the square of the overlap integral between the vibrational wavefunctions of the two states that are involved in the transition.

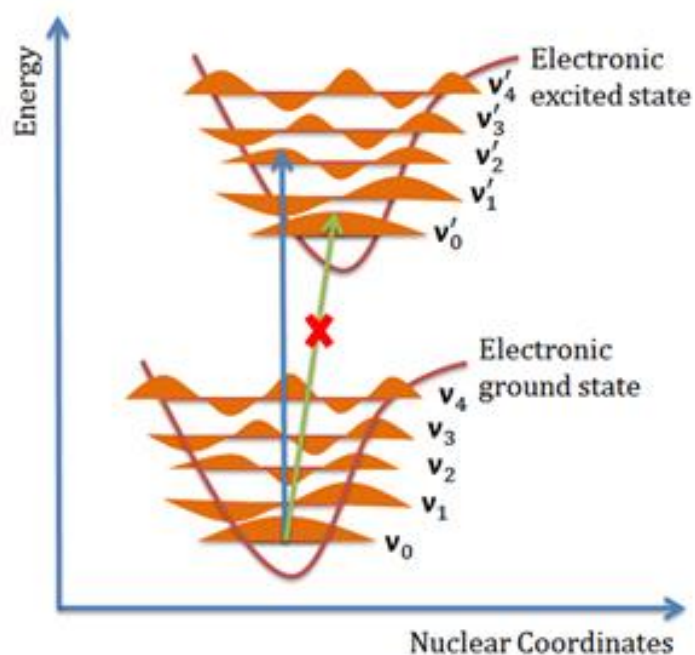


Figure 1.8: Franck-Condon energy diagram

1.10.3. Conical Intersection

A conical intersection of two potential energy surfaces is the set of molecular geometry points where the two potential energy surfaces are degenerate and the non-adiabatic couplings between these two states are non-vanishing. In the vicinity of conical intersections, the Born-Oppenheimer approximation breaks down, letting non-adiabatic processes to happen. The location and characterization of conical intersections are as a result essential to the understanding to a wide range of reactions, such as photo-reactions, explosion and combustion reactions, etc.

The conical intersections are also called molecular funnels or diabolic points. This comes from the very important role they play in non-radiative de-excitation transitions from excited electronic states to the ground electronic state of molecules. For example, the stability of DNA with respect to the UV irradiation is due to such conical intersection [6]. The molecular wave packet excited to some electronic excited state by the UV photon follows the slope of the potential energy surface (PES) and reaches the conical intersection from above. At this point the very large vibronic coupling induces a non-radiative transition; which leads the molecule back to its electronic ground state.

Chapter 2

Biomolecules and UV Excitation

- 2.1. *Excited-States in Biomolecules*
- 2.2. *Single-base excited states*
 - 2.2.1. *Steady-State Experimental Absorption Spectra*
 - 2.2.2. *Steady-State Experimental Fluorescence Spectra*
 - 2.2.3. *Computed Fluorescence Spectra*
 - 2.2.4. *Time-Resolved Fluorescence Experiments and Fluorescence Decay*
 - 2.2.5. *Computed S_0 - S_1 Conical Intersection*
- 2.3. *Dark Excited States in Pyrimidines*
 - 2.3.1. *$S_n\pi^*$ states*
 - 2.3.2. *Triplets*
- 2.4. *5-benzyluracil as the Model Systems for DNA-Protein Cross-Linking*

2.1 Excited-States in Biomolecules

Ultraviolet light is strongly absorbed by DNA, producing excited electronic states that sometimes initiate damaging photochemical reactions. Fully mapping the reactive and nonreactive decay pathways available to excited electronic states in DNA is a quest. Progress toward this goal has accelerated rapidly in recent years, in large measure because of ultrafast laser experiments. There are studies concerning the nature and dynamics of excited states in DNA model systems in solution. Nonradiative decay by single, solvated nucleotides occurs primarily on the subpicosecond timescale. Surprisingly, excess electronic energy relaxes one or two orders of magnitude more slowly in DNA oligo- and polynucleotides. Highly efficient nonradiative decay pathways guarantee that most excited states do not lead to harmful reactions but instead relax back to the electronic ground state. Understanding how the spatial organization of the bases controls the relaxation of excess electronic energy in the double helix and in alternative structures is one of the most exciting challenges in the field.

Electronic excitation of DNA by solar ultraviolet (UV) light can produce harmful photoproducts such as the thymine dimer. Excitation is efficient because of the substantial UV absorption cross sections of the DNA nucleobases: adenine, guanine, cytosine, and thymine (Figure 2.1). The vast majority of excitations do not initiate photoreactions as evidenced by the quantum yields of photo lesion formation, which are generally much less

than 1%. The altered structures and base pairing properties of photoproducts can interfere with the work of polymerases and disrupt normal cellular processing of DNA. This interference can lead to mutations, genomic instability, and carcinogenesis [7]. In organisms exposed to solar UV light, DNA constantly accrues photochemical damage that must be continually repaired. Disruption of the equilibrium between damage and repair can lead to skin cancer—the cancer with the highest rate of incidence in many nations [8]. The importance of this biological problem has fueled interest in excited electronic states of nucleic acids for over 50 years.

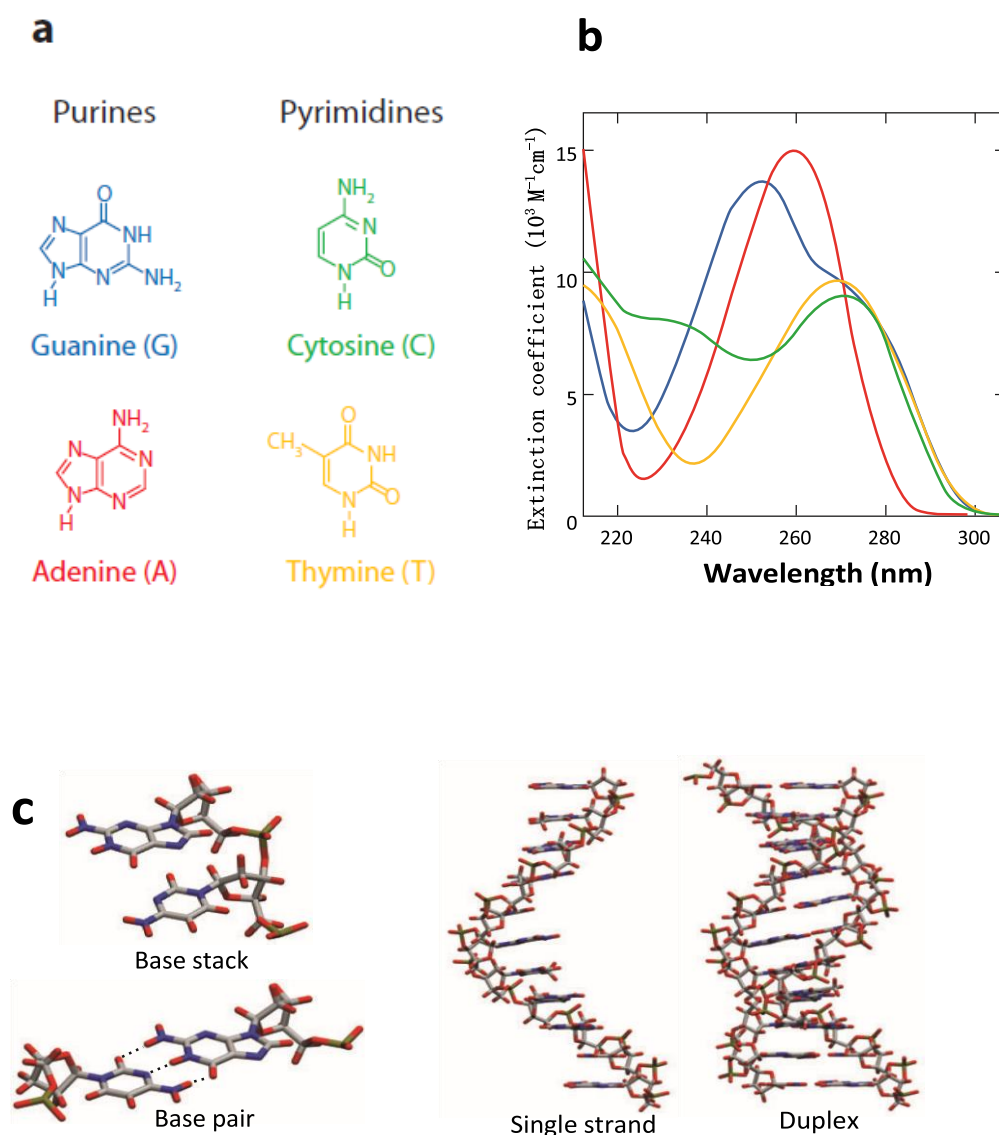


Figure 2.1: (a) Chemical structures and (b) UV absorption spectra of the DNA bases. (c) Basic assemblies of nucleobases.

Interest in DNA photophysics has intensified in recent years as powerful spectroscopic and computational techniques have provided unprecedented new insights into nonradiative decay mechanisms. The goal of understanding how excess electronic energy evolves in DNA at the molecular level appears increasingly within reach. This energy relaxes via a multitude of pathways that include photon emission, nonradiative transitions to the ground or intermediate electronic states, and reactive decay to photoproducts. Highly efficient nonradiative decay to the electronic ground state (S_0) significantly lowers the rate of DNA damage, thereby reducing the workload of an organism's repair machinery [9].

2.2 Single-base excited states

The intense UV absorption by DNA at 260 nm arises from the strongly allowed $S\pi\pi^*$ transitions of the nucleobases [10,11]. Single bases in aqueous solution have small fluorescence quantum yields of $\sim 10^{-4}$ [12, 13], indicating that the vast majority of excited states decay nonradiatively.

Ultrafast passage between electronic states is commonplace when a wave packet moves into the vicinity of a conical intersection (CI), and it was proposed in 2000 that CIs are responsible for the subpicosecond fluorescence lifetimes of the nucleobases [14]. In a pioneering computational study, Ismail et al. [15] subsequently described a nearly barrierless decay pathway from the Franck-Condon region of cytosine to S_0 via a pair of CIs. Since then, CIs have been located for all of the natural bases and many of their derivatives at various levels of theory [16]. These studies have firmly established that ultrafast internal conversion (IC) occurs because CIs can be accessed from the Franck-Condon region via near-barrierless pathways. Most studies calculate minimum energy pathways through static potential energy landscapes, but dynamical studies capable of following a photoexcited wave packet as a function of time are beginning to appear [17–20].

Nucleobase CIs are often accessed via out-of-plane deformations initiated by twisting about double bonds. For pyrimidine bases, many studies have shown that torsion about the C5-C6 bond is a key deactivation step [15, 21–24]. The excited-state energy is relatively insensitive to ring puckering, but the ground state is strongly destabilized by

the loss of π -bond stabilization (aromaticity). As a result, the ground-state energy rises sharply along the ring-deformation coordinate, eventually meeting the comparatively flat excited-state surface in a CI. Many physical chemists will recognize this pathway from classic work on the nonradiative decay of photoexcited ethene. Similar bond-twisting pathways have been located for purine bases [25, 26].

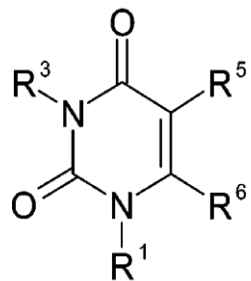
To have a better understanding of the photoexcited processes occurring in the double helix, a large number of experimental and theoretical studies have thus been devoted to characterize the photophysical behavior of their building blocks (nucleobases, nucleosides, and nucleotides). All the bases absorb strongly in the UV region, and thus, a significant amount of energy is deposited in the absorbing excited state. However, such as in the case of nucleic acids, the nucleobases appear to be remarkably stable toward photodegradation, suggesting that any possible photochemical processes are efficiently prevented by a fast nonradiative decay to the ground state.

Indeed, femtosecond time-resolved fluorescence and transient absorption studies agree in assigning subpicosecond lifetimes to the bright excited state of nucleobases in room-temperature aqueous solution, implying very efficient internal conversion processes [2]. In particular, fluorescence upconversion experiments [28-32] on the monomeric DNA constituents have revealed that the fluorescence decays are extremely fast (<1 ps) and cannot be described by single exponentials, hinting at complex nonradiative deactivation processes occurring in the excited states.

A very fruitful approach to shed light on the ground-state recovery mechanism has been to compare the excited-state behavior of different derivatives of the nucleobases. Already protonation/deprotonation may have a strong effect on the excited-state lifetime. Guanosine in acid solution (pH = 2-3) becomes protonated on the 7-position, which increases the lifetime from the subpicosecond range to about 200 ps [28, 33, 34]. It is also well-known that substitution of the side groups may have a substantial influence on the excited-state properties, affecting the lifetime drastically. The most well-known example is 2-aminopurine, an adenine analogue with the amino group shifted from the 6- to the 2-position. For this reason, the excited state lifetime increases by more than a factor of thousand from the picosecond to the nanosecond range [35]. Less drastic but still important effects have been observed for cytidine, where methylation on the 5-position increases the excited-state lifetime by a factor of 10 [36, 37].

The static and dynamical behaviors of the excited states of uracil and 10 of its derivatives have also been characterized by means of femtosecond fluorescence upconversion and quantum chemical calculations.

Uracil and the closely related thymine (5-methyluracil) are the simplest nucleobases present in RNA and in DNA, respectively. They may therefore serve as “reference compounds” for a combined experimental and theoretical study. Furthermore, getting a closer insight on the excited-state features of the six-member pyrimidines could also help understanding the behavior of the purine bases (adenine and guanine). A measure of the uracil excited-state lifetime using femtosecond transient absorption spectroscopy was reported [38]. The excited-state lifetime was found to be less than 200 fs, in principle, limited by the time resolution of the apparatus.



	R ¹	R ³	R ⁵	R ⁶
U	H	H	H	H
1MU	Me	H	H	H
3MU	H	Me	H	H
T	H	H	Me	H
6MU	H	H	H	Me
1,3DMU	Me	Me	H	H
1MT	Me	H	Me	H
5FU	H	H	F	H
5CIU	H	H	Cl	H
TFT	H	H	CF ₃	H
5F1,3DMU	Me	Me	F	H

Table 2.1: Schematic structure of the substituted some Uracils, where R¹, R², R³, and R⁴ denote the different substituents corresponding to the table

These 11 uracil derivatives have been selected in order to cover substitution at different positions and of different chemical nature (electronegativity, weights, etc.), while multiple substitutions allow to verify the presence of additive and/or cooperative effects.

2.2.1. Steady-State Experimental Absorption Spectra

The absorption spectra of five chosen uracils (U), 6-methyluracil (6MU), 1,3-dimethyluracil (1,3DMU), thymine (T), and 5-fluorouracil (5FU), in aqueous solution are shown in Figure 2.2.

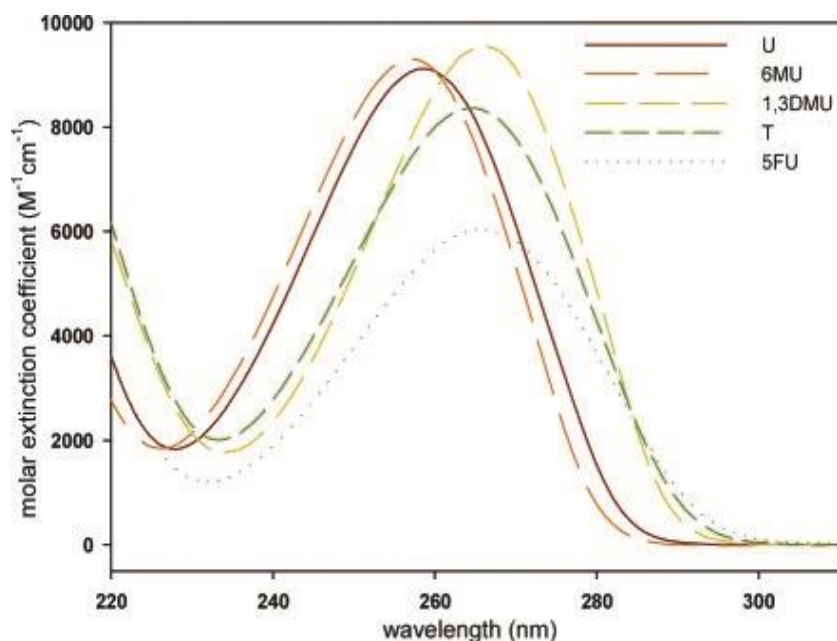


Figure 2.2: Steady-state absorption spectra of five uracils in roomtemperature aqueous solutions: uracil (U), 6-methyluracil (6MU), 1,3dimethyluracil (1,3DMU), thymine (T), and 5-fluorouracil (5FU); [24].

The comparison of the results obtained for the 11 studied compounds allows us to highlight some interesting features regarding their absorption spectra:

First, for what concerns methyl-substituted compounds, they are increasingly red-shifted in the order (on a wavelength scale)

$$6\text{MU} < \text{U}/3\text{MU} < \text{T} < 1,3\text{DMU} < 1\text{MU} < 1\text{MT}$$

Methyl substitution in positions 1 and 5 leads to a noticeable red shift of the absorption maxima. As a matter of fact, both thymine and 1-methyluracil peaks are red-shifted with respect to that of uracil. The effect of the methyl substituent in positions 1 and 5 seems to be additive, as shown by the maximum of 1-methylthymine, that is more red-shifted with

respect to uracil. On the other hand, methyl substituent in positions 3 and 6 does not lead to significant red shift of the absorption maxima. Actually, the 6-methyluracil peak is slightly blue-shifted with respect to the uracil one.

Moreover, absorption spectra of 5-substituted compounds are increasingly red-shifted in the order (on a wavelength scale)

$$\text{TFT} < \text{U} < \text{T} < \text{5FU} < \text{5CIU}$$

2.2.2. Steady-State Experimental Fluorescence Spectra

In figure 2.3 the Steady-state fluorescence spectra of five chosen uracils (U), 6-methyluracil (6MU), 1,3-dimethyluracil (1,3DMU), thymine (T), and 5-fluorouracil (5FU), in room-temperature and in aqueous solution obtained for excitation at 255 nm, are shown.

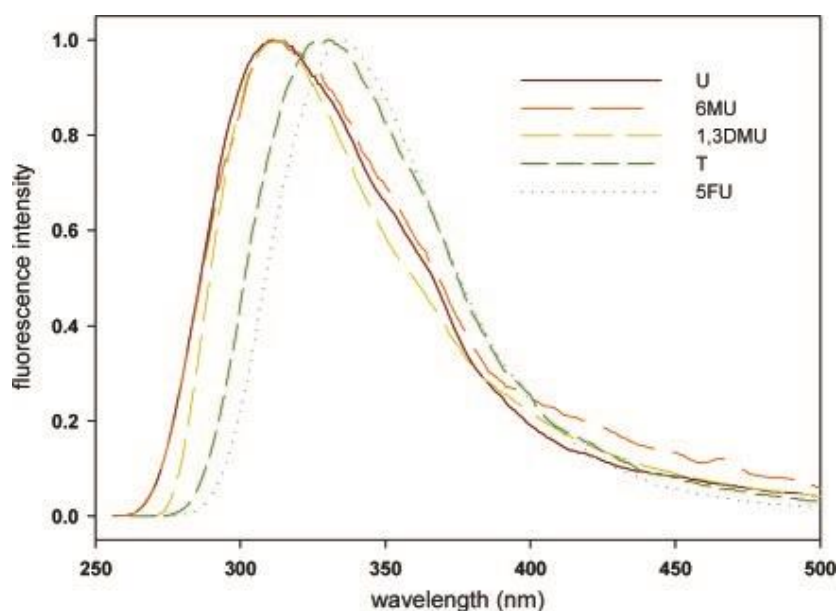
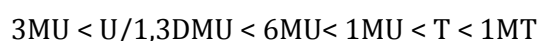


Figure 2.3: Steady-state fluorescence spectra of five uracils in room temperature aqueous solutions: uracil (U), 6-methyluracil (6MU), 1,3dimethyluracil (1,3DMU), thymine (T), and 5-fluorouracil (5FU); [24].

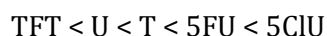
All the compounds examined exhibit a very large Stokes shift (~ 1 eV, $\sim 8 \times 10^3$ cm⁻¹), suggesting significant changes of the excited state geometry. Actually, since the emission maxima do not follow the same trend as the absorption maxima, the Stokes shifts vary a lot, ranging from about 6000 cm⁻¹ for 1,3-dimethyluracil to more than 8100 cm⁻¹ for 5-fluorouracil.

For what concerns methyl-substituted uracil derivatives, the emission peaks are increasingly red-shifted in the order (on a wavelength scale)



Two subsets can be recognized in the above compounds. Although they were separated by more than 1000 cm⁻¹ in absorption, the peaks of the compounds bearing a 5-methyl substituent (1MT and thymine) are very close and more than 1000 cm⁻¹ red-shifted with respect to the remaining five. Those latter exhibit emission peaks very close (within 500 cm⁻¹), while the absorption maxima were dispersed.

The emission peaks of 5-substituted derivatives of uracil are increasingly red-shifted in the order (on a wavelength scale)



This is the same trend as for the absorption peaks. However, also in this class of compounds, the Stokes shift is not uniform, being larger for 5-halo-substituted compounds and much smaller for uracil and trifluorothymine. From a phenomenological point of view, the strong correlation of absorption and fluorescence spectra suggests that the 5-substituent affects ground-state and relaxed excited-state electronic structures in a similar (but not identical) way.

2.2.3. Computed Fluorescence Spectra

In the theoretical analysis, geometry optimization in aqueous solution is done [24] and stable local energy minima in the proximity of the Franck-Condon (FC) point for all the compounds, except for 6-methyluracil. For this compound, excited-state geometry optimization leads directly toward a region of the PES where the S₀ and S₁ state are close

to be isoenergetic (i.e., close to the S₀/S₁ conical intersection). TD-DFT geometry optimizations predict significant distortion from planarity of the pyrimidine ring that assumes a “boat-like” conformation, with N3 and C6 out of the plane defined by N1, C2, C4, and C5 that are indeed close to being coplanar (Figure 2.4).

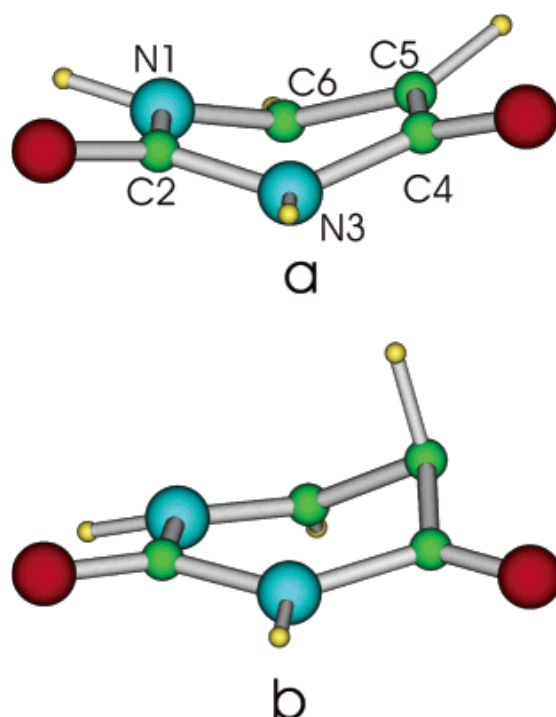


Figure 2.4: Geometry of uracil (a) in the minimum of π/π^* electronic state (b) in the S₁/S₀ conical intersection.

While N3 is significantly pyramidalized in all of the compounds, in thymine and 5-fluorouracil, the geometry around C6 is still close to being planar (H-C6-N1-C5 improper dihedral angles being 172 and 176°, respectively). The geometry of the carbonyl moieties is also very close to planarity. Not surprisingly, the largest variations of the bond lengths involve the lengthening of C5-C6, C4-O8, and N3-C4 bond distances and the shortening of C4-C5 bond distance, in line with the bonding/antibonding character of HOMO and LUMO with respect to those bonds.

The significant geometry distortion upon electron excitation is in line with the diffuseness of the jet-cooled absorption spectra [39], and the computed geometry shifts are similar to that obtained at the DFT/MRCI level [40] in the gas phase.

When only bulk solvent effects are included, the computed fluorescence energies are much lower than the experimental maxima, suggesting that some important effect has not been taken properly into account by calculations. Since previous studies on uracil excited state shows that the coordination geometry of the first solvation shell remarkably depends on the electronic state of the solute [41], excited state geometry optimization have been done including four explicit water molecules. The coordination geometry of the water molecules in the excited state is actually quite different from that predicted for the ground state. The computed fluorescence energy is then much closer to the experimental one, and the relative energy ordering is similar to that predicted by experiments (with the exception of 1,3-dimethyluracil), supporting the reliability of the excited-state geometry minima determined.

Before comparing experimental and computational results, it is also important to remember that a lot of caution has to be used when analyzing the fluorescence peak values for the compounds with ultrashort fluorescence lifetimes. Steady-state spectra may be dominated by fluorescence from non-relaxed excited-state conformations and thus blue-shifted and broadened. Experiments show indeed that, on the average, compounds having longer characteristic fluorescence times tend to exhibit larger Stokes shifts. When such fast reactions are studied as in the present case, the dynamical behavior of solvent molecules, that is, the time necessary to adopt the optimal coordination geometry for the excited state, should also play a relevant role.

2.2.4. Time-Resolved Fluorescence Experiments and Fluorescence Decay

Fluorescence decays were recorded for $\sim 2.5 \times 10^{-3}$ mol/dm³ aqueous solutions at 330 nm after 267 nm excitation [24]. The resulting decay curves for uracil, 6-methyluracil, 1,3dimethyluracil, 5-methyluracil (thymine), and 5-fluorouracil are shown in Figure 2.5.

Also the 330 fs (FWHM) Gaussian apparatus response function is displayed in figure 6. As can be seen, the fluorescence decays of the first three compounds are extremely fast, barely longer than the apparatus function. The fluorescence decays of two 5-substituted compounds, on the other hand, are much longer.

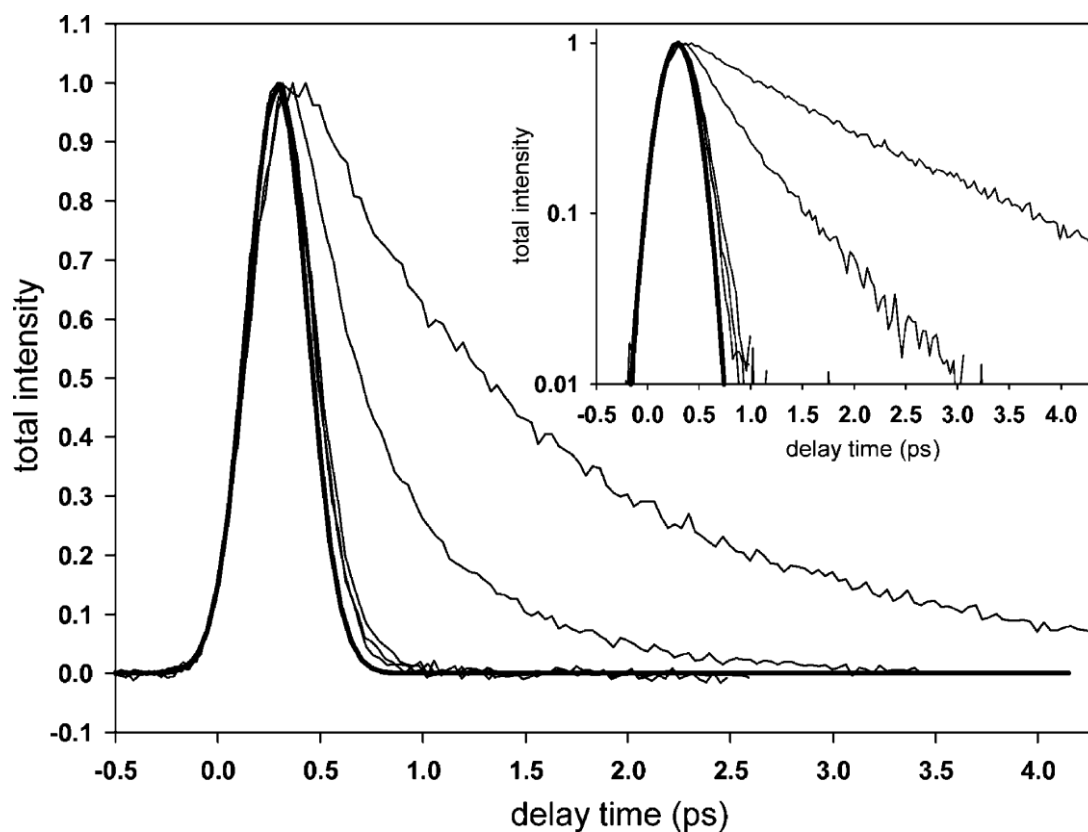


Figure 2.5: Fluorescence decays at 330 nm after excitation at 267 nm of five uracils in room-temperature aqueous solutions ($\sim 2.5 \times 10^{-3}$ mol/dm³): (in increasing order) uracil, 6-methyluracil, 1,3-dimethyluracil, 5-methyluracil (thymine), and 5-fluorouracil. Also shown is the 330 fs Gaussian apparatus function. The insert shows the same curves on a semi-log scale; [24].

A full comparative analysis of the fluorescence decays of the 11 derivatives reveals that uracil, 1-methyluracil, 3-methyluracil, 6-methyluracil, and 1,3-dimethyluracil possess very rapid decays. A mono-exponential model was used for the parameter estimation, and the fluorescence lifetimes were found to be about 100 fs.

It can be seen that the only position that affects significantly the excited-state lifetime is C5. A biexponential model was used for the parameter estimation, and the fluorescence lifetimes were found to contain one ultrafast component varying between 100 and 700 fs and one much slower component. With increasing lifetime the order is

$$U < \text{TFT} < 5\text{CIU} < \text{T} \sim 1\text{MT} < 5\text{F1,3DMU} < 5\text{FU}$$

Notably, the fluorescence of thymine and 1-methylthymine, which are methylated on the 5 position, decays about 4 times slower than the fluorescence of uracil and the 1-, 3-, and 6-methylated derivatives. In particular, 5-fluorination makes the excited-state lifetime substantially longer, for both uracil and 1,3DMU.

2.2.5. Computed S_0 - S_1 Conical Intersection

To understand how the nature of the substituents affect the fluorescence lifetime, the S_1/S_0 conical intersection (CI) have been located for three representative compounds, namely, uracil, thymine, and 5-fluorouracil. One of the key motions to reach the S_1/S_0 conical intersection is the pyramidalization at C5 (Figure 2.6) [24, 42], while an out of plane motion of the H5 hydrogen atom (or of the C5 substituent) leads the C5 substituent toward a “pseudo perpendicular” arrangement with respect the molecular plane (Figure 2.4).

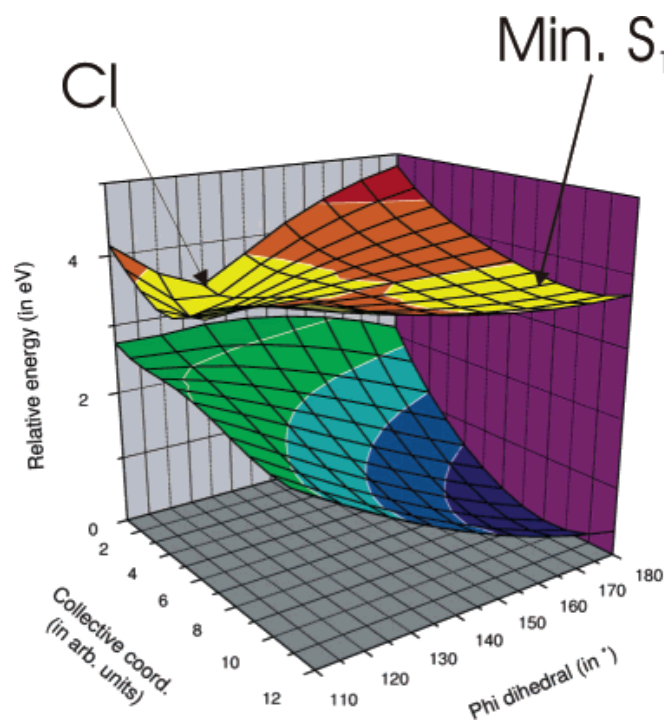


Figure 2.6: S_0 and S_1 potential energy surfaces (in eV) in the region connecting the minimum of the π/π^* state and the S_0/S_1 conical intersection for uracil; [24].

With the aim of exploring more thoroughly the excited-state PES in the region connecting the FC to the CI, some bidimensional (2D) maps of the S_1 surface are computed.

Restricting the $3N-6$ dimensional space to a 2D one is clearly arbitrary, and a purposely tailored study of the vibrational modes connecting the FC region to the CI should be necessary in order to unambiguously assess the dynamical motion on the S_1 PES. As a first step in this direction, on the basis of these computational results [24], it is chosen to focus on the out of plane motion of the C5 substituent (φ improper dihedral). The second “collective” coordinate x (giving account also for the C5 pyramidalization) is instead defined imposing that all the other internal coordinates move in a synchronous way. Inspection of Figure 7 supports the reliability of the conical intersection structure. In the region of the configurations space close to the CI point, the S_0 and the S_1 PESs are extremely close (energy difference ≈ 0.2 eV ($\approx 1.6 \times 10^3$ cm $^{-1}$)) both in the gas phase and in aqueous solution. Also, when the effect of dynamical correlation solvent effect are included, it is confirmed that the conical intersection is reached by out of plane motion of the C5 substituent. For uracil, the S_1 PES in the region connecting Min S_1 and CI (Figure 2.7) is flat, and the height of the energy barrier separating Min- S_1 and CI is small (~ 0.1 eV, $\sim 8 \times 10^2$ cm $^{-1}$), in line with the very small fluorescence lifetime.

The results obtained for thymine and 5-fluorouracil are similar, but the height of the barrier between Min- S_1 and CI is larger than in uracil. Its value can be estimated to ~ 0.2 eV ($\sim 1.6 \times 10^3$ cm $^{-1}$) for thymine and in the range 0.5-1 eV ($(4-8) \times 10^3$ cm $^{-1}$) for 5-fluorouracil. These results show that, for thymine and, even more, for 5-fluorouracil, the out of plane motion is more difficult than for uracil.

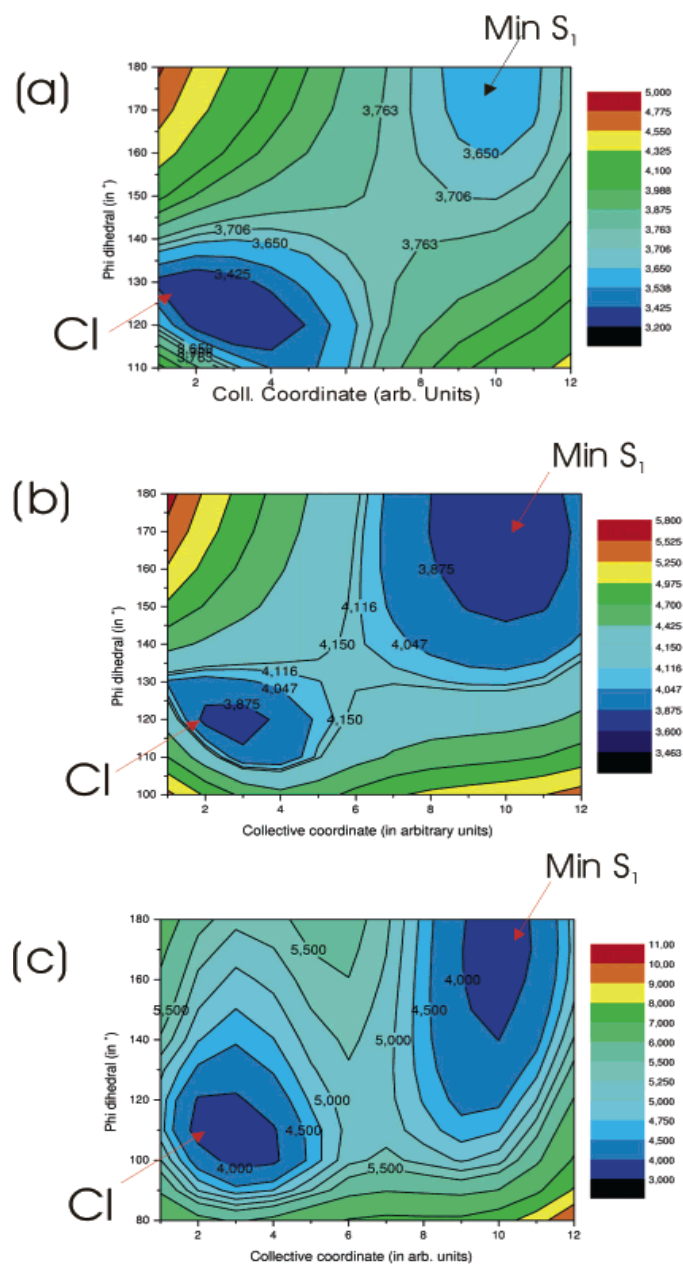


Figure 2.7: S₁ potential energy surfaces (in eV) connecting the minimum of the π/π^* state and the S₀/S₁ conical intersection: (a) uracil; (b) thymine; (c) 5-fluorouracil. PCM/TD-PBE0/6-31G(d) calculations in aqueous solution; [24]

2.3 Dark Excited States in Pyrimidines

Excited states are classified as dark or bright according to whether they are reached by transitions from S_0 that have small or large oscillator strengths, respectively. In addition to the bright $S\pi\pi^*$ states, all nucleobases have excited states with $Sn\pi^*$ character as well as triplet states ($Tn\pi^*$ and $T\pi\pi^*$) [9-11, 16, 43-46]. These states are dark and have been extremely difficult to characterize by conventional spectroscopic techniques. Although excitation of S_0 molecules overwhelmingly populates the bright $S\pi\pi^*$ states, dark states can be subsequently reached via IC. Direct spectroscopic evidence of the dark states has been accumulating for pyrimidine bases, as reviewed in the following subsections.

2.3.1. $Sn\pi^*$ states

There is debate about whether passage to S_0 occurs directly through a single CI or indirectly through two or more CIs in a cascade involving an intermediate $Sn\pi^*$ state [47-50]. This debate, which has largely concerned deactivation pathways for gas-phase nucleobases, has become highly relevant to solution-phase dynamics since the surprising discovery that a large fraction of the population excited to the lowest $S\pi\pi^*$ state decays to the lowest-energy $Sn\pi^*$ state in water [51] and other solvents [52].

Hare et al. discovered by means of transient absorption measurements that the initial excited state population bifurcates for 1-cyclohexyluracil in a variety of solvents [52] and for various pyrimidine bases in aqueous solution [51]. For 1-cyclohexyluracil, 60% of excited molecules decay on an ultrafast timescale to S_0 , and the remainder relax orders of magnitude more slowly via a long-lived trap state [52]. The trap state is dark, as indicated by the absence of long-time emission from pyrimidine bases (23, 40, 41), and is assigned to the lowest-energy $Sn\pi^*$ state [52]. In water, between 10% and 50% of photoexcited pyrimidine bases decay via a $Sn\pi^*$ state [51]. The lifetime of the $Sn\pi^*$ state of 1-cyclohexyluracil is highly sensitive to solvent, ranging from 26 ps in water to 2.2 ns in acetonitrile [52]. In contrast, $S\pi\pi^*$ lifetimes depend only modestly on the solvent [53, 54].

The discovery that electronic energy relaxes on a picosecond timescale much of the time in photoexcited pyrimidine bases shows that ultrafast IC is not the sole factor responsible for DNA's photostability. In water, Hare et al. [51] observed lifetimes of between 10 and 150 ps for different pyrimidine bases. Additionally, they reported that the $Sn\pi^*$ lifetime is significantly longer for pyrimidine nucleosides than for free bases. They also proposed that excess vibrational energy in the $Sn\pi^*$ state accelerates IC to the ground state.

According to this hypothesis, ribosyl substitution extends the $S_n\pi^*$ lifetime by reducing the excess vibrational energy that promotes nonradiative decay.

Femtosecond time-resolved infrared (IR) experiments are providing many new insights into DNA excited states, including the elusive dark states [55-57]. UV pump/IR probe experiments provide a particularly powerful way to study excited-state dynamics [58]. Electronic absorption bands frequently overlap, making transients from UV/UV or UV/visible experiments difficult to interpret. In contrast, vibrational bands are narrower and have much greater structural sensitivity. Quinn et al. [56] measured lifetimes of 33 and 37 ps for a band at 1574 cm^{-1} in dCyd (2deoxycytidine) and dCMP (2-deoxycytidine 5-monophosphate), respectively. These decays agree within experimental uncertainty with the $S_n\pi^*$ lifetime of CMP (cytidine 5-monophosphate) measured in Hare et al.'s [51] UV/UV experiments. A broad vibrational band at 1760 cm^{-1} due to a carbonyl stretch in the $S_n\pi^*$ state of 1-cyclohexyluracil is also found (Figure 2.8) [59]. The lifetime of this band in acetonitrile and methanol.

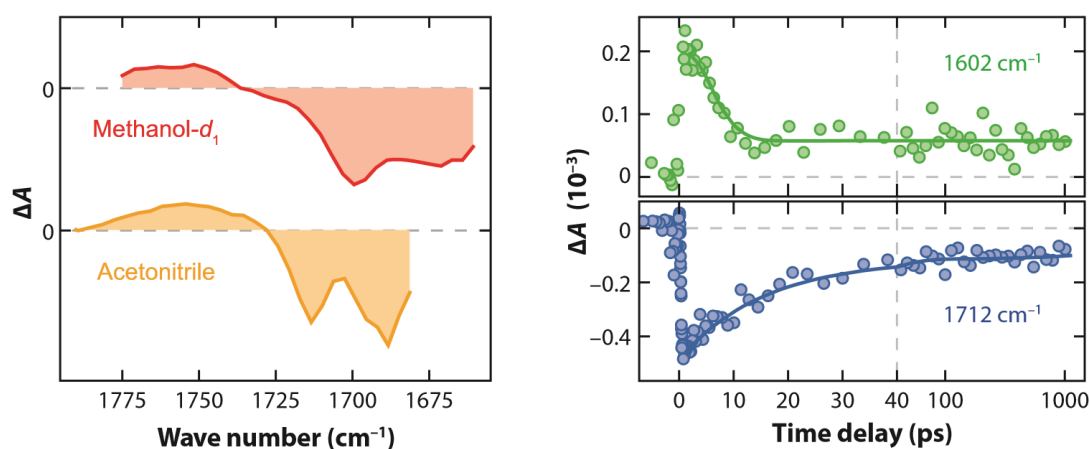


Figure 2.8: Mid-IR transient absorption is advantageous for probing dark-state dynamics. (a) Transient IR difference spectra of 1-cyclohexyluracil show a broad positive band at 1760 cm^{-1} assigned to the $S_n\pi^*$ state in methanol- d_1 (top) and acetonitrile (bottom). (b) The long-lived transient at 1602 cm^{-1} is assigned to the lowest triplet state of thymine in acetonitrile- d_3 (top), which is fully formed just 10 ps after photoexcitation. The bleach recovery signal at 1712 cm^{-1} for 1-cyclohexyluracil in acetonitrile exhibits complex kinetics (bottom); [59].

2.3.2. Triplets

Hare et al. [52] observed that the long-time 1-cyclohexyluracil signals are quenched in the presence of oxygen and assigned them to the lowest triplet state. Observing intersystem crossing (ISC) dynamics is difficult in aqueous solution because triplet yields are less than a few percent [60]. However, yields are much greater in less polar, aprotic solvents [52, 61]. Based on the observation of vibrational cooling by hot triplet states, Hare et al. [52] concluded that the triplet states are formed within the first few picoseconds after photoexcitation, even in solvents in which long-lived $S\pi\pi^*$ states are found. The same conclusion was reached in a later study of ISC by pyrimidine bases in water [51]. The most compelling evidence for rapid ISC comes from UV/IR experiments on thymine in acetonitrile that directly monitored the prompt appearance of vibrational bands assigned to the $T\pi\pi^*$ state [57].

The appearance of triplet states after no more than a few picoseconds seems to indicate that ISC takes place from the short-lived $S\pi\pi^*$ state, as suggested by some theoretical studies [62, 63]. However, Hare et al.'s [52] result showing that 60% of the $S\pi\pi^*$ population returns directly to the ground state in all solvents, independent of the triplet quantum yield, make this mechanism unlikely. In contrast, the $S\pi\pi^*$ yield depends on the solvent and is inversely proportional to the triplet yield, suggesting that ISC to the $T\pi\pi^*$ state occurs from the $S\pi\pi^*$ state. Because ISC does not occur during the entire $S\pi\pi^*$ lifetime, Hare et al. proposed that ISC to the triplet state occurs only in $S\pi\pi^*$ molecules with excess vibrational energy. In this model, vibrational cooling in the $S\pi\pi^*$ state rapidly reduces the internal energy, and ISC effectively halts within a few picoseconds. This model explains the low triplet yields observed in hydrogen-bonding solvents with their high vibrational cooling rates, compared to polar, aprotic solvents, in which vibrational cooling occurs more slowly [52].

2.4 5-benzyluracil as the Model Systems for DNA–Protein Cross-Linking

UV irradiation of protein-nucleic acid complexes results in the cross-linking of the protein to the nucleic acid. The use of this reaction to study protein nucleic acid interactions has been limited because it is very inefficient and is accompanied by extensive protein and

nucleic acid damage [64]. The resulting complicated reaction mixtures also make it difficult to identify specific amino acid/base cross-links; Ser-T, Cys-T, Lys-T, and Tyr-T are the only cross-links so far characterized [65-67]. Therefore a simple model systems to explore the cross-linking of tyrosine, phenylalanine, and tryptophan to the pyrimidine bases is quite beneficial.

Irradiation with a high-intensity UV laser significantly increases the efficiency of protein-nucleic acid cross-linking [68]. However, it is difficult to investigate the involved processes in the presence of competing protein and nucleic acid degradation. So model systems seems to be really valuable to provide an ideal case on which one is able to evaluate the importance of a biphotonic excitation, or likewise, other photo-induced reaction mechanisms. These advantages are because of the cleaner photochemistry nature of such models.

A model-building strategy is involved in attaching the pyrimidine base to the tyrosine, phenylalanine, and tryptophan side chains, using a short linker to mimic the proximity and orientation in DNA-protein complexes; Sun et al. have proposed and synthesized 5-benzyluracil as a simple model in which the photocyclization resembles the photo-cross-linking of DNA to protein [69] as depicted in Figure 2.9. Biphotonic excitation is also found to contribute little to the yield of these reactions, even when using high-intensity irradiation.

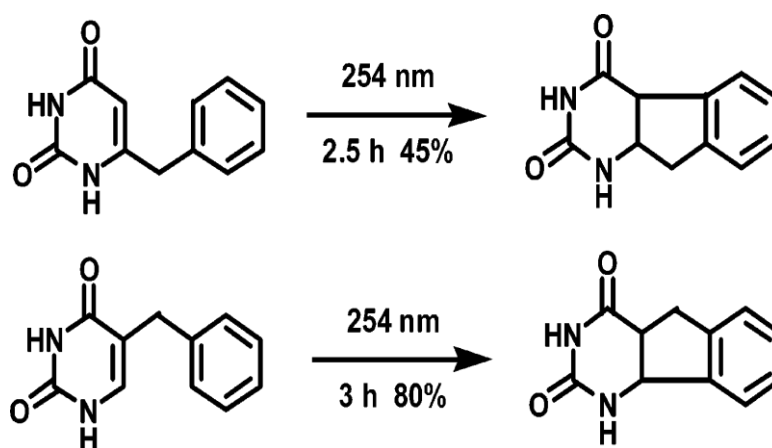


Figure 2.9: 5-benzyluracil and 6-benzyluracil as Simple model systems to explore the photo-cross-linking between the pyrimidine bases and the side chains of the aromatic amino acids: mimicking DNA-Protein cross-linking; [69].

Chapter 3

5BU and 5,6BU Steady-State Measurements

- 3.1. *Photocyclization of 5BU*
- 3.2. *Materials and methods for spectroscopy measurements*
- 3.3. *Molecular geometries in the ground state*
- 3.4. *Photophysical properties in the Frank Condon region*
- 3.5. *Optical characterization of the photocyclization process*
- 3.6. *Excited states decay channels*
- 3.7. *Fluorescence anisotropy and 5BU to 5,6BU transformation*
- 3.8. *Photocyclization Quantum Yield*
- 3.9. *Fluorescence Quantum Yield*
- 3.10. *Solvent Effect in Photocyclization*
- 3.11. *Global Picture for the Photophysics and Photochemistry of 5BU: Assignment of the experimental steady state spectra*
- 3.12. *Excited State geometry optimizations*

3.1. Photocyclization of 5BU

The analysis of the molecular mechanisms underlying UV-induced DNA-protein cross-link (UV-CL in the following) is a difficult task with a microscopic description being far from completion [70]. In an effort to improve the comprehension of such a fundamental process Sun et al. investigated experimentally the cross-linking of tyrosine, phenylalanine, and tryptophan to the pyrimidine bases relying on a simple model-building strategy [69]: They attached the pyrimidine base to the tyrosine, phenylalanine, and tryptophan side chains, using a short and chemically inert linker to mimic the proximity and orientation in DNA-protein complexes. The quantum yield (QY) for UV-CL of such simple models was more than one order of magnitude lower than the QY of thymine dimer formation; moreover, no significant two photon contribution was verified [69]. While such a simple model is surely distant from the complexity of an actual DNA-protein cross-link “in vivo”, it can nevertheless provide useful insights into the molecular mechanism underlying the formation of a covalent bond between DNA bases and protein aminoacids. In particular, the UV-induced photocyclization of 5-benzyluracil (5BU) leading to may well describe possible structures related to the cross-linking of phenylalanine to DNA. Moreover, the 5BU photoreaction, involving a cyclization, can also be contextualized in the study of the dynamics of the ring closure [71-73], which is widely investigated in the perspective of realizing effective molecular switches [74].

The goal of this chapter is to characterize the photophysical and photochemical properties of 5-benzyluracil (5BU) and 5,6-benzyluracil (5,6BU) in methanol (MeOH) solution, with steady state electronic spectroscopy. Experimentally, we have characterized absorption and fluorescence (including its anisotropy) of 5BU and 5,6BU, the latter produced by UV femtosecond pulses photo-absorption, measuring the fluorescence QY as well as the QY of 5,6BU production in methanol. Aqueous solution is also used to check the role of solvent in the photocyclization process. This way we'll gain insight on the photophysical and photochemical properties of the two molecules by identifying the electronic states involved in the absorption and emission spectra and the relevant microscopic conformations of reactant and product.

3.2. Materials and methods for spectroscopy measurements

5BU powder (purchased from ALCHEMY Fine Chemicals & Research, Italy) was dissolved in methanol 99,8% HPLC grade. The absorbance spectra were acquired with a UV/VIS spectrophotometer device using a quartz cuvette with optical length of 1 cm. The spectra were acquired in the range 210-300 nm at several concentrations, both for 5BU and 5,6BU, verifying the linearity of the response. The fluorescence emission spectra were measured with a LS55 Perkin Elmer spectrofluorometer. The excitation wavelength was 265 nm and the fluorescence was collected in the range 290-380 nm. The optical path of the fluorescence photons in the cuvette was approximately 1 mm. The same device, with automatic polarizers both in excitation and emission, was used to carry out anisotropy measurements. The measurements were corrected for the grating efficiency factor. 5,6BU was obtained by UV photoirradiation of 5BU by a femtosecond laser system (Light Conversion, Lithuania). This device operates at 258 nm (fourth harmonic of 1032 nm, fundamental wavelength of the IR source PHAROS), about 200 fs pulse duration, 2 kHz repetition rate thereby delivering 340 mW average power (170 μ J/pulse). The sample was constantly stirred with a magnetic bar to have a homogenous solution while irradiating.

The characterization of the final product after UV laser pulse irradiation of the 5BU was essential to verify the occurrence of the photocyclization process and the consequent complete transformation of 5BU into 5,6BU in the appropriate conditions of irradiations. To this end High-performance liquid chromatography (HPLC) and Nuclear Magnetic Resonance (NMR) spectroscopy of the pure and irradiated 5BU are carried out.

For the spectral measurements of the photoproduct, 5,6BU samples obtained after 1 minute irradiation of 5BU solutions with (340 mW average power) UV laser pulses. Such samples were used since we verified that these samples contained only 5,6BU.

3.3. Molecular geometries in the ground state

In Figure 3.1 the ground state structures of the 5BU and 5,6BU in MeOH are reported. In the case of 5BU in Methanol, the structure shows appreciable differences from the geometry obtained in gas phase. It implies then the role of solvent in its structure; this distortion is due to a solvent induced internal rotation around the hinge connecting the two chromophore moieties.

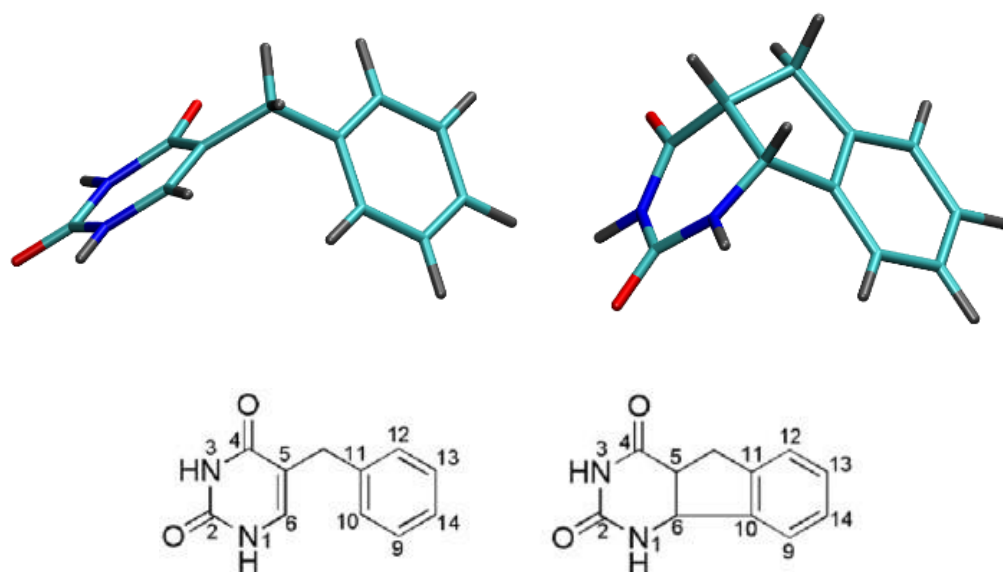


Figure 3.1: Stick representation of the solvated ground state molecular geometries of 5BU (left) and 5,6BU (right). Carbon atoms are colored in cyan, oxygen in red, nitrogen in blue and hydrogen in gray.

3.4. Photophysical properties in the Frank Condon region

The UV electronic absorption spectra of 5BU and 5,6BU in Methanol were experimentally recorded to characterize the principal electronic transitions. The measured absorption profiles of the molecules are reported in Figure 3.2. The data reflect the dramatic electronic structure changes that occur after cyclization.

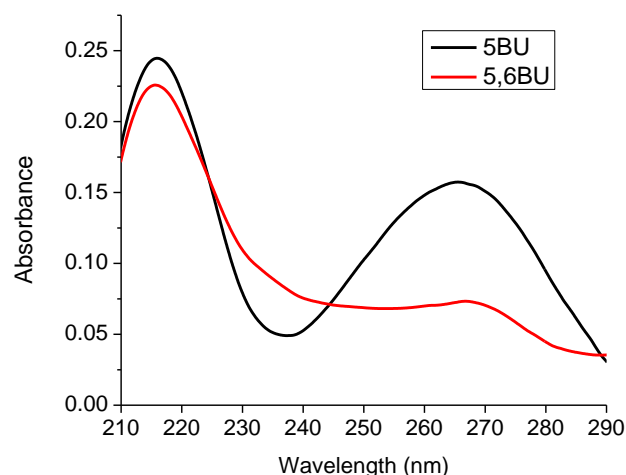


Figure 3.2: Absorption spectra of 5BU (black) and 5,6BU (red).

To analyze the spectrum of 5BU let us recall that this molecule is chemically composed of two chromophores: the benzene (model of aromatic amino acid) and the uracil/thymine moieties. Calculations show that the electronic transitions involve mainly the uracil fragment. This is particularly true for the first two transitions, i.e. those contributing to the absorption spectrum in the lower energetic band. Their character originates from the typical uracil bright $\pi\pi^*$ and dark $n\pi^*$ transitions [75], while no intrachromophore transitions are observed for the benzene moiety in this energy range. This is because the only transition of benzene accessible in our experimental conditions is the lowest $\pi\pi^*$ electronic transition [76] which has oscillator strength much lower than the bright uracil $\pi\pi^*$ transition and, hence, its contribution to the absorption spectrum of 5BU is negligible. The computed uracil transition energies in 5BU are slightly red shifted compared to the ones relative to pure uracil in similar solutions [77] due to the perturbation induced by the chemical bridging to the second chromophore (benzene). In addition to these intrachromophore transitions, we also observe charge transfer (CT)

excitations from the benzene to the uracil moiety, which contribute to the lower energy band centered at 265 nm in the experimental spectrum.

Interestingly, for the uracil we observe two absorption lines both with mixed $\pi\pi^*$ and $n\pi^*$ character and similar oscillator strengths instead of the two separate bright uracil $\pi\pi^*$ and dark $n\pi^*$ transition observed in gas phase calculations [76]. The origin of the mixing is mainly due to the solvent induced quasi-degeneracy of the $\pi\pi^*$ and dark $n\pi^*$ transitions.

Concerning 5,6BU, an unequivocal assignment of the electronic transitions in the range between 250-300 nm (that includes the laser wavelength, 260 nm) is not possible because of the weak absorption around 240 nm, which just results in a shallow shoulder in the computed spectrum not resolved experimentally (at room temperature). The first excited state transition is the closest and brightest in that spectral region but, together with this transition, higher energy excitations can be activated.

The cyclization process induces a change in the π -conjugated system of the uracil moiety (disappearance of the enonic group) with consequent loss of the $\pi\pi^*$ transition observed in isolated uracil and 5BU. Characteristics of the 5,6BU are therefore the intrachromophore aromatic $\pi\pi^*$ transition in the benzene moiety (at 240 nm with an oscillator strength of roughly one third of the $\pi\pi^*$ transition in uracil) and the $n\pi^*$ transition of uracil

3.5. Optical characterization of the photocyclization process

We started the optical characterization of 5BU and 5,6BU by measuring their absorption spectra as a function of the irradiation time. The achieved results are plotted in Figure 3.3.

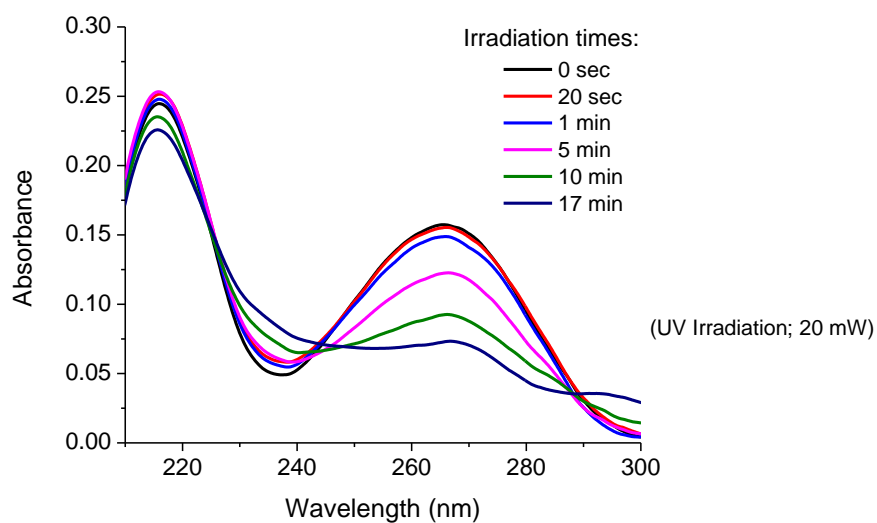


Figure 3.3: Absorbance of irradiated 5BU. The irradiation time is shown in the legend: 0 sec corresponds to 5BU and 17 min corresponds to 5,6BU.

The change of 5BU into 5,6BU can be considered complete after 17 minutes irradiation with 20 mW laser average power (or equivalently after 60 seconds in the case of irradiation with 340 mW laser average power); since no more significant changes in the spectra are detectable with longer irradiation times.

Similarly to what was done for absorption, fluorescence emission spectra were measured as a function of irradiation time, so that the change of 5BU into 5,6BU could be again followed as a function of the irradiation time. Compared to the absorption, the change in the spectral features is much more striking. Figure 6 shows that a significant shift of the peak from 310 nm to 360 nm occurs when 5BU is photocyclized into 5,6BU (dotted line $t=0$ s versus solid line $t=60$ s, irradiation with 340 mW laser average power, in Figure 3.4).

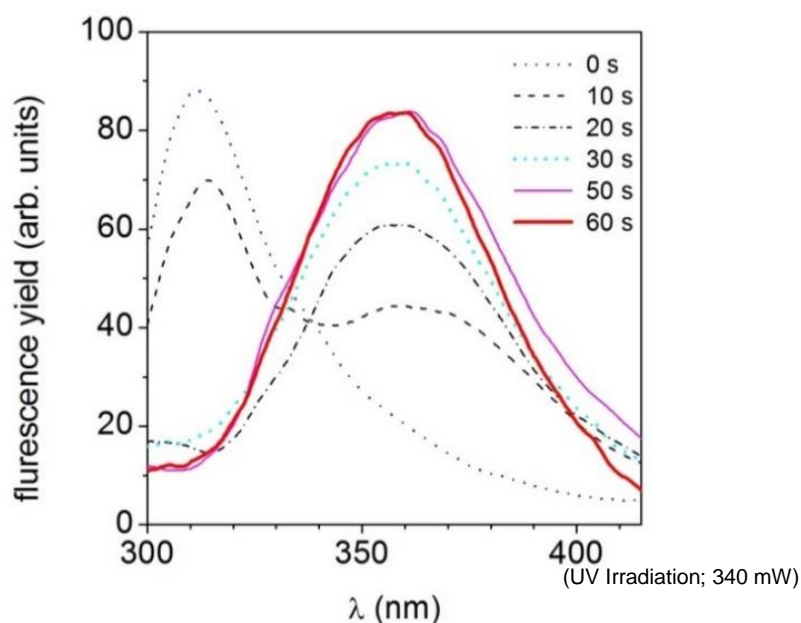


Figure 3.4: Fluorescence of irradiated 5BU ($\lambda_{exc}=265$ nm). The irradiation time is shown in the legend: dotted, 0 s; dashed 10 s; dash-dotted, 20 s; short-dashed 30s, thin solid line 50 s and thick solid line 60 s. 0 s corresponds to 5BU and 60 s corresponds to 5,6BU.

3.6. Excited states decay channels

In general it is known from several quantum chemical calculations [78] that the excited state ultrafast decay of DNA/RNA bases is favored by the existence of barrierless paths that lead to very efficient non radiative decay processes via conical intersections (CI) with the ground state. Moreover, recent non-adiabatic molecular dynamics studies in gas phase [79] have shown that, after excitation to the $\pi\pi^*$ state, the pyrimidine nucleobases remain mainly trapped into a shallow energy minimum for a time of the order of few picoseconds before finding their way to a CI with the ground state through a non-radiative path. In calculations on 5BU there is a relaxation path on the $\pi\pi^*$ state leading to a stable intermediate state in which a molecular distortion similar to that observed in uracil and thymine occurs.

Finally, it is important to stress that the covalent bond formation between the carbons C6 and C10 in 5BU does not coincide with the generation of the final product 5,6BU. The full reaction mechanism requires an additional tautomerization reaction, causing a proton (or hydrogen) to be transferred from the carbon atom C10 to the carbon atom C5. We believe that, in this

step, the solvent plays an important role in the formation of the final cyclized product, possibly via a solvent assisted proton (or hydrogen) transfer, as hypothesized also by Sun et al [69].

3.7. Fluorescence anisotropy and 5BU to 5,6BU transformation

To gain insight into the electronic relaxation time scale of the 5BU and 5,6BU we also measured the fluorescence anisotropy through the polarization coefficient [80] $A=(I_{\parallel}-I_{\perp})/(I_{\parallel}+I_{\perp})$ as a function of the laser irradiation time. In the definition of the polarization coefficient I_{\parallel} and I_{\perp} are the fluorescence yield polarized parallel and orthogonal to the polarization direction of the incident beam, respectively. The results are reported in Figure 3.5 and show that $A\approx 0.5$ at $t=0$, i.e. when only 5BU is in the solution, and reduces to approximately 0.17 for long irradiation time when 5BU is completely photocyclized (i.e. for 5,6BU).

The high value of anisotropy found for 5BU suggests the presence of a systematic error, increasing the anisotropy absolute values. However for our aim to conclude the photocyclization quantum yield, the absolute values are not important; the decay of anisotropy as a function of irradiation time is the key information we need to calculate the decay constant.

Then, fitting these experimental results with an exponential decay model of the form $f(t) = a + b \exp(-t/\tau)$, leads to $\tau = 20.9 \pm 0.6$ seconds; which is the characteristic time for 5BU to 5,6BU transformation.

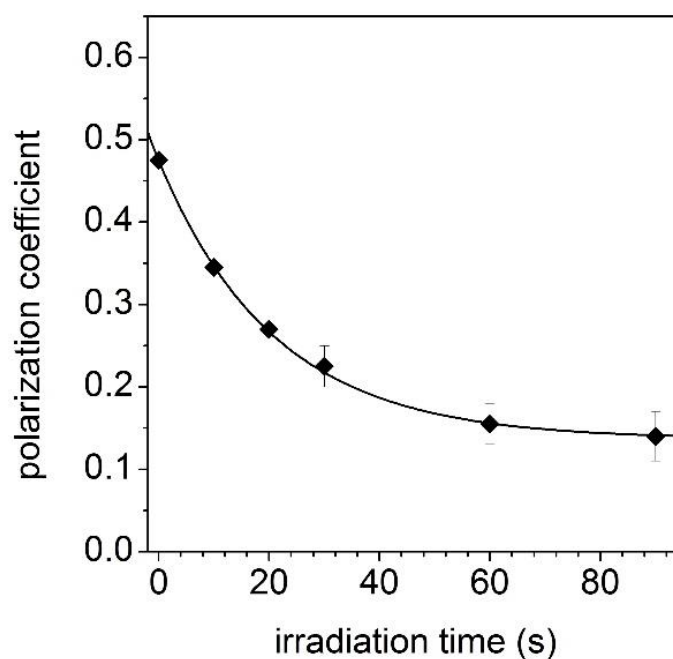


Figure 3.5: Anisotropy of the fluorescence emission as a function of the irradiation time measured at $\lambda=320$ nm. At $t=0$ s only 5BU is present which photocyclizes to 5,6BU when irradiated. The continuous line is the best fit with the function $f(t) = a + b \exp(-t/\tau)$ (see main text) that leads to $\tau=20.9 \pm 0.6$ s. The error bars come from the uncertainty in the measurement of the fluorescence yield propagated in the equation for the polarization coefficient.

3.8. Photocyclization Quantum Yield

The features observed in the fluorescence spectra reported in Figure 6 allow an indirect measurement of the photocyclization QY (p_{pc} in the following), via the knowledge of the characteristic time for 5BU \rightarrow 5,6BU transformation. To show this, we report the fluorescence yield in the 355-365 nm range as a function of the irradiation time in Figure 11. This plot shows that the collected fluorescence signal saturates after approximately 1 minute of irradiation at 0.34 W. This behavior can be explained by considering the occurrence of the reaction $h\nu + 5BU \rightarrow 5,6BU$ together with the conservation of the number of molecules; hence we have

$$\frac{d}{dt} N_{pc}(t) = \frac{N_{5BU}(t)}{\tau}$$

$$N_{5BU}(t) + N_{pc}(t) = N_{5BU}(0) \quad (3.1)$$

where t is the irradiation time and N_{5BU} and N_{pc} are the concentration of 5BU and 5,6BU, respectively. In Eqs. (3.1) τ is the characteristic time for the transformation of 5BU into 5,6BU and is given by

$$\tau = \frac{1}{f_L p_{abs} p_{pc}} \quad (3.2)$$

where f_L is the repetition rate of the laser (2 kHz), p_{abs} is the probability that a molecule absorbs one photon in a single laser pulse and p_{pc} is the probability that the excited molecule will photocyclize (i.e. p_{pc} is the photocyclization quantum yield).

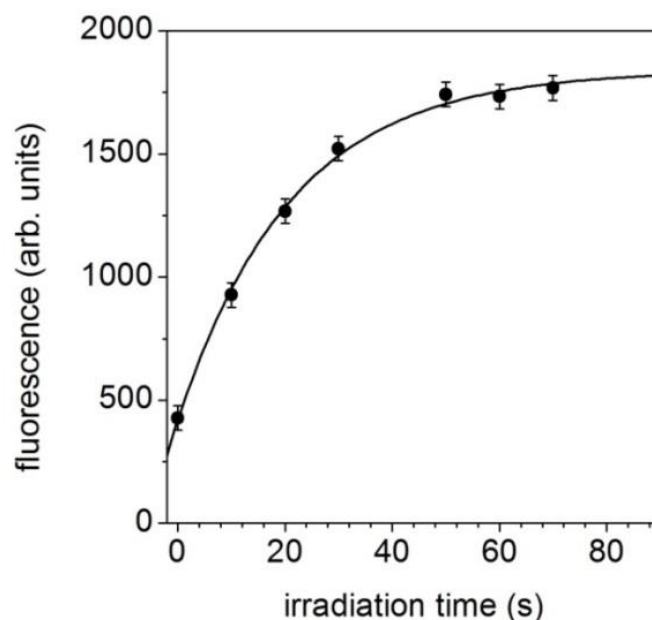


Figure 3.6: Fluorescence yield of the irradiated solution in the range 355-365 nm as a function the irradiation time. The continuous line is the best fit with the function $f(t) = a + b \exp(-t/\tau)$ that leads to $\tau = 21.3 \pm 1.4$ s.

The assumption $\tau \gg \tau_{eq}$, τ_{eq} being the time required for homogenizing the solution, is necessary for the validity of Eqs. (3.1) and is well fulfilled in our conditions, i.e. we can reasonably assume that the gradient in the 5,6BU concentration between irradiated and not irradiated volume is negligible.

Since the fluorescence signal is proportional to the concentration and the latter can be easily derived from Eqs. (3.1), we have the following relation for the overall fluorescence detected in the wavelength range 355-365 nm:

$$FY(t) = k_{inst} N_{5BU}(0) \left[FY_{pc} - (FY_{pc} - FY_{5BU}) \exp\left(-\frac{t}{\tau}\right) \right] \quad (3.3)$$

In Eq. (3) FY_{pc} and FY_{5BU} are the fluorescence quantum yields of 5,6BU and 5BU, respectively, k_{inst} is an instrumental constant. The best fit of the experimental data in Figure 3.6 with a function like that in Eq. (3.3) allows us to estimate the characteristic photocyclization time as $\tau = 21.3 \pm 1.4$ seconds.

To check the validity of this estimate we considered also the dependence of the polarization coefficient, A , on the irradiation time (see Figure 3.5) that follows a law similar to Eq. (3.3), i.e. we have

$$A(t) = A_{pc} - (A_{pc} - A_{5BU}) \exp\left(-\frac{t}{\tau}\right) \quad (3.4)$$

where A_{5BU} and A_{pc} are the polarization coefficients of the 5BU and 5,6BU, respectively. The best fit of the experimental results in Figure 10 allows us to estimate the characteristic photocyclization time as $\tau = 20.9 \pm 0.6$ s in very good agreement with the estimation through fluorescence yield. From the two independent measurements we have the combined estimation of this time as $\tau = 21.2 \pm 0.6$ s.

Apart from p_{pc} , the only remaining unknown quantity in Eq. (3.2) is p_{abs} , which can be estimated as follows. Far from the saturation (linear absorption) the probability that a photon in a single laser pulse is absorbed by a molecule is proportional to the number photons in that laser pulse, N_f , and to the absorption cross section σ_{abs} , i.e.

$$p_{abs} = \frac{N_f \sigma_{abs}}{S} = \frac{E_{pulse} \sigma_{abs}}{h\nu S} \quad (3.5)$$

where S is the effective area illuminated by the laser. In our conditions, this area coincides with the section of the cuvette since the mixing is fast enough to consider the solution homogeneous. We have measured the absorptivity ε of the 5BU to be $11,900 \text{ Mol}^{-1} \cdot \text{cm}^{-1}$, which

in turn provides $\sigma_{abs}[\text{cm}^2] = 3.82 \times 10^{-21} \varepsilon [\text{Mol}^{-1} \text{cm}^{-1}] = 4.5 \times 10^{-17}$. Since we have $E_{pulse} = 170 \mu\text{J}$, $h\nu = 4.8 \text{eV}$ ($\lambda = 258 \text{nm}$) and $S = 1 \text{cm}^2$, the probability that in our experimental condition a photon is absorbed by a 5BU molecule is $P_{abs} = 10^{-2}$ in one laser pulse. From Eq. (3.2) by considering $f = 2 \text{kHz}$ we have $p_{pc} = 2.4 \times 10^{-3}$ in excellent agreement with Sun et al [69].

3.9. Fluorescence Quantum Yield

The fluorescence Quantum Yield (QY) of 5BU and 5,6BU is provided by [81]:

$$QY_X = QI_R \frac{I_X \cdot OD_R \cdot n_X^2}{I_R \cdot OD_X \cdot n_R^2} \quad (3.6)$$

where OD stands for the optical density (absorbance), I for the fluorescence intensity and n for the refraction index, the subscript X and R referring to the molecule whose QY has to be measured and to the reference, respectively. Since 5BU is diluted in methanol and the reference molecule (tryptophan) in water, we have $n_X \approx n_R$, and hence

$$QY_X = QI_{Try} \frac{Slope_X}{Slope_{Try}} \quad (3.7)$$

In Eq. (3.7) *Slope* refers to the slopes in Figure 3.7, X standing for 5BU or 5,6BU. By using tryptophan as the reference molecule and its fluorescence quantum yield, $QY_{Try} = 0.13 \pm 0.01$, as reported in literature [81], we have $QY_{5BU} = 0.11 \pm 0.02$ and $QY_{5,6BU} = 0.38 \pm 0.02$. These values represent the first measurements of the fluorescence quantum yields for 5BU and 5,6BU. QY for both molecules are four order of magnitude higher than fluorescence QY for thymine and uracil [82].

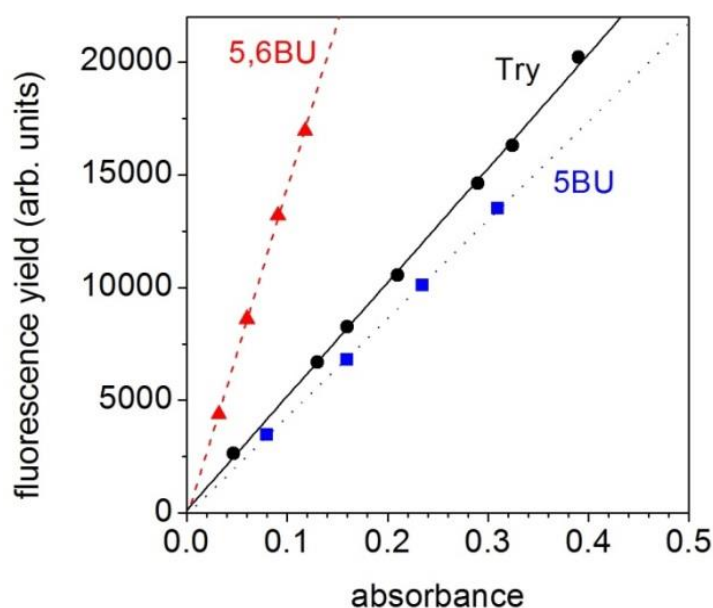


Figure 3.7: Fluorescence vs absorbance for 5BU, 5,6BU and Tryptophan ($\lambda_{exc}=278$ nm), the latter used as standard.

3.10. Solvent Effect in Photocyclization

We already mentioned that the role of solvent in the configuration of 5BU molecules is essential. To have a look at this parameter, and to check the role of solvent in the photocyclization process, we also prepared samples of 5BU, solved in Water. The absorbance spectrum of this solution is then measured; showing similar profile as 5BU in Methanol.

The samples are then irradiated; and once again, similar to the case of 5BU in Methanol solutions, the absorbance at 265 nm reduces as a function of irradiation time, i.e. when more 5BU molecules are transformed to 5,6BU (Figure 3.8 and 3.9). This reduction of absorbance value is then stopped when all 5BU molecules are photocyclized; afterward there will be no change in the reduced value of absorbance.

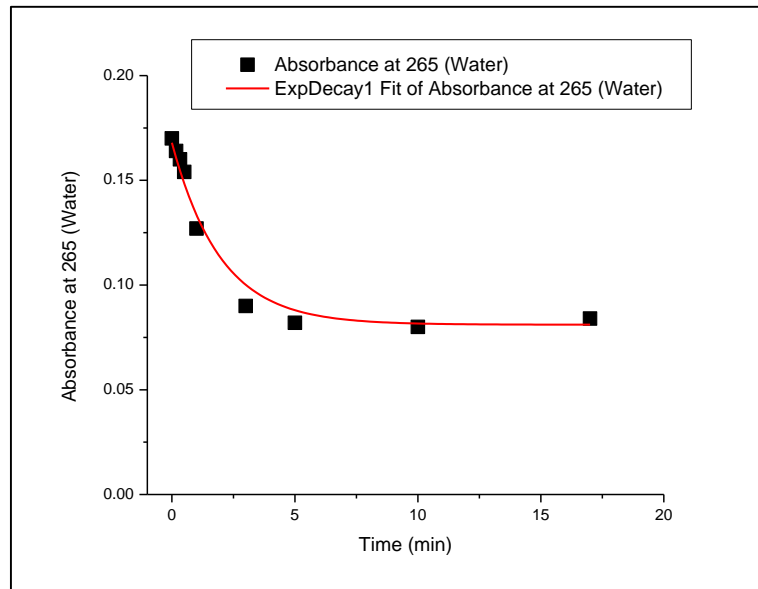


Figure 3.8: Reduction of absorbance value at 265 nm for the solution of 5BU in Water. $\tau_{(\text{Water})} = 2 \pm 0.4$ min

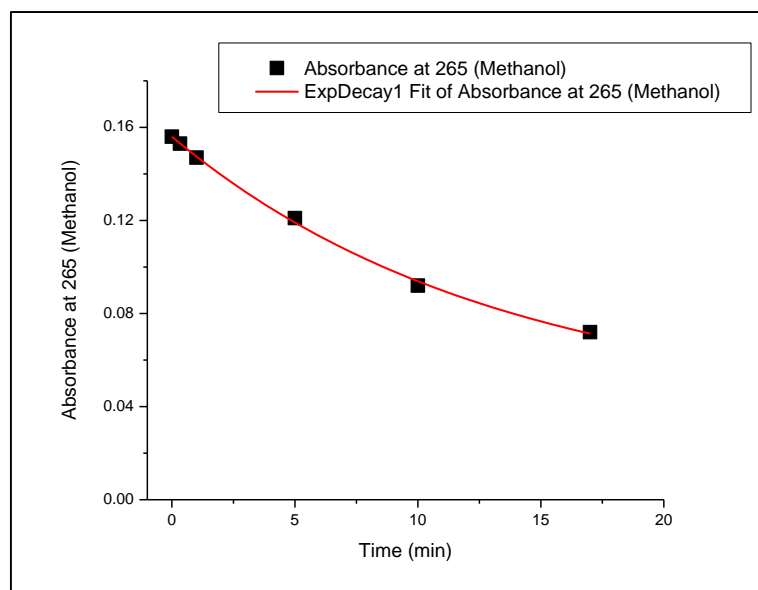


Figure 3.9: Reduction of absorbance value at 265 nm for the solution of 5BU in Methanol. $\tau_{(\text{Methanol})} = 13 \pm 2$ min

However there is an evident difference in the reduction behaviors; it happens faster for the 5BU solution in water, compared to the case of having Methanol as the solvent. Fitting on the experimental results with an exponential decay model, we can deduce characteristic times of

5,6BU formation. The fitting results show that this characteristic time is 13 ± 2 minutes in the case of methanol solution, and 2 ± 0.4 when the solvent is water (the irradiation is at the same laser average power).

In this experiment, the laser average power is 15 mW. Looking at the Eq (3.5), it is clear that the photon absorption probability in a single laser pulse by a molecule, p_{abs} , is proportional to the average power of the laser beam. Therefore $p_{\text{abs}} = 6 \times 10^{-4}$ for both experiments in Methanol and water.

Using Eq. (3.2), photocyclization probability after excitation, p_{pc} , is 2.1×10^{-3} in the case of 5BU in Methanol solution where $\tau = 13$ minutes. In the same irradiation condition, meaning the same p_{abs} , the transformation characteristic time, τ , is 2 minutes for the solution of 5BU in Water, which gives rise to a value of 1.4×10^{-2} for the photocyclization probability.

In fact these set of measurements reveal that the photocyclization process is favored in water. This can be explained with the fact that 5BU molecules have folded configuration in water and the two moieties, benzene and uracil, stay in a closer distance to each other. This is due to hydrophobic property of benzene part in 5BU; which repulse water molecules. Having such folded configuration is then make it easier for the carbon atoms C6 and C10 to bond (Figure 3.1).

3.11. Global Picture for the Photophysics and Photochemistry of 5BU: Assignment of the experimental steady state spectra

In order to get a more detailed description of the photophysical and photochemical behavior of 5BU we resorted to Quantum Mechanics calculations, by using DF/TD-DFT calculations employing M052X and CAMB3LYP functionals. Solvent effects are included by means of the PCM model and explicitly considering two CH₃OH molecules of the first solvation shell, see Figure 3.10.

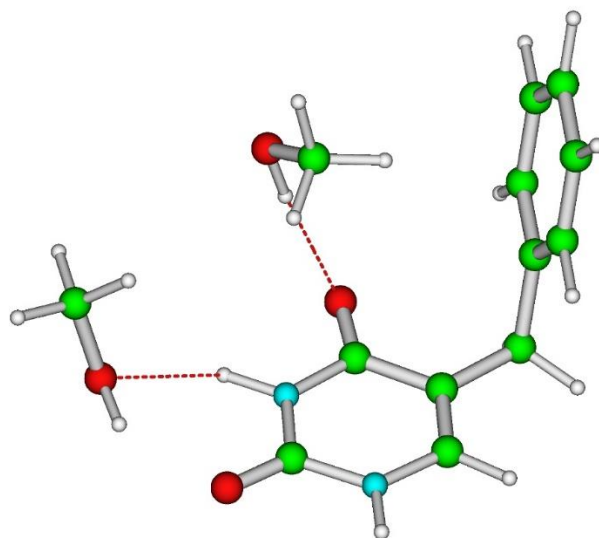


Figure 3.10: Computational model used to study 5BU in methanol solution

The computed absorption profiles of the molecules are reported in Figure 3.11. Confirming the results obtained by using other functionals and without considering specific solute.-solvent interactions [83], the compute spectra reflect the dramatic electronic structure changes that occur after cyclization. Although the calculated bands show a systematic blue shift, the overall agreement between theory and experiments is sufficient to allow an unequivocal assignment of the transitions.

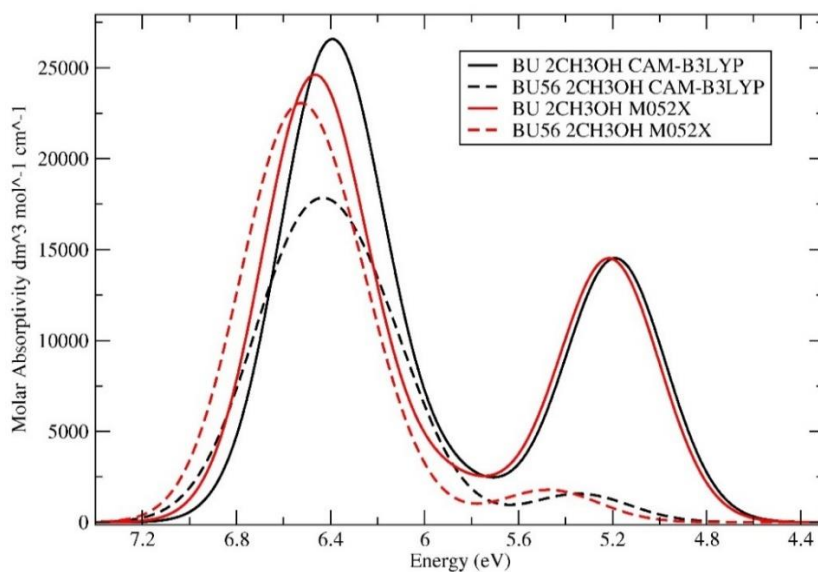


Figure 3.11: Computed absorption spectra for 5BU and 56-BU in methanol solution, on models including 2 CH₃OH molecules. Each stick transitions have been broadened by a gaussian with HWFM 0.25 eV.

	Description	CAM-B3LYP		M052X	
		S ₀ min	orthogonal	S ₀ min	orthogonal
S₁	$\pi\pi^*$ of Uracil with small B→U CT character	5.18(0.27)	5.19(0.25)	5.20(0.20)	5.27(0.19)
S₂	$n\pi^*$ of Uracil with small B→U CT character	5.36(0.00)	5.39(0.02)	5.22(0.07)	5.34(0.07)
S₃	$\pi\pi^*$ of B with small B→U CT character	5.43(0.00)	5.45(0.01)	5.56(0.00)	5.57(0.01)
S₄	B→U CT	5.88(0.04)	5.79(0.03)	5.89(0.04)	5.90(0.03)

Table 3.1 Vertical excitation energy (in eV) of the 4 lowest energy excited states computed for 5BU• 2 CH₃OH in methanol solution at the PCM/TD-DFT/6-31G(d) calculations. Oscillator strength is given in parentheses.

As reported in Table 3.1, the lowest energy absorption band of 5BU is mainly due to a strong $\pi\pi^*$ transition, similar to that found for Uracil and Thymine, though some participation of $\pi\pi$ orbitals of the Benzene Moiety can be recognized, especially when the two rings are stacked. In any case when the two rings are constrained in an “orthogonal” arrangement no dramatic change of the predicted spectra is found (see the columns of Table 3.1 labeled as “orthogonal”). There are three other less intense transitions in the proximity of the spectroscopic state. One can be described an $n\pi^*$ transition, involving the transfer of an electron from the Lone pair of the C4=O group towards a π^* orbital of Uracil (the LUMO). A second one is essentially a $\pi\pi^*$ transition localized over the benzene ring. Please note that coupling between Uracil and Benzene transitions is found also in these two latter states, modulated by the orientation of the two rings. Finally, S₄ can be described as a Benzene→Uracil Charge Transfer (CT) state.

3.12. Excited State geometry optimizations

The results of the excited state geometry optimizations of S₁ strongly depend on the mutual orientation of the two rings. When optimizing the “orthogonal” conformation, we obtain a picture similar to those already found for Thymine. after photoexcitation, a steep path leads to a flat region of the PES, where the pyrimidine ring maintains a planar geometry, while the

most significant geometry shifts mainly involve the bond lengths and bond angles of the ethylenecarbonyl moiety (O8C4C5C6 atoms) [84, 85]. C4C5 distance decreases by 0.03 Å, C4O8 increases by 0.03 Å, and, especially, the C5C6 bond length increases by 0.1 Å in line with the bonding/antibonding character of HOMO and LUMO with respect to the C5C6 double bond ($S\pi\pi^*$ -min*-pla). In $S\pi\pi^*$ -min*-pla, the oscillator strength is rather high and the calculation of the emission energy at 4.34 eV suggests that the region around $S\pi\pi^*$ -min*-pla is the main cause of the maximum of the fluorescence spectrum at 310 nm. In the following in order to make easier the comparison with experiments we shall also report λ_{corr} values, obtained by red-shifting the computed emission energy by the same difference between the computed values and the maximum of the absorption band.

On the other hand, frequency calculations at $S\pi\pi^*$ -min*-pla show the existence of an imaginary frequency and that this structure is a saddle-point in a path leading to the absolute minimum of $S\pi\pi^*$ ($S\pi\pi^*$ -min), where the pyrimidine ring takes a bent conformation (see Figure 3.12), with N3 and C6 out of the plane defined by N1, C2, C4, and C5 that are indeed close to being coplanar. $S\pi\pi^*$ -min and $S\pi\pi^*$ -min*-pla are almost isoenergetic (their energy difference is <0.05 eV), the bond lengths and bond angles of these two minima also being similar [84]. Red-shifted emission ($\lambda_{\text{corr}} \sim 350$ nm) is associated to this region.

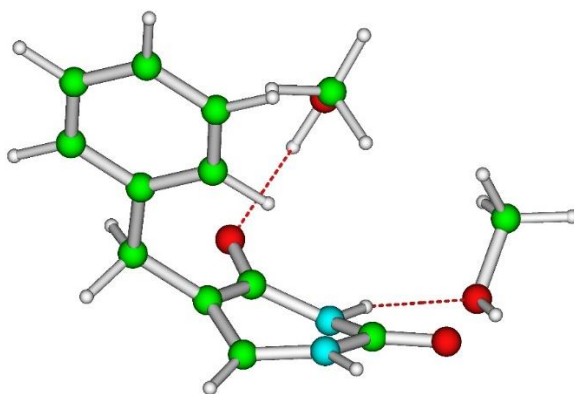


Figure 3.12: Schematic drawing of the nonplanar minimum of the lowest energy $\pi\pi^*$ state localized on Uracil moiety

$S\pi\pi^*$ -min is separated by a very small energy barrier (0–100 cm^{-1}) from a crossing region with S_0 [84, 86–88]. In analogy with what found for Uracil and Thymine, one of the key motions to reach this Conical Intersection (CI) is the pyramidalization at C5, while an out-of-plane motion leads the benzene ring toward a “pseudo-perpendicular” arrangement with respect to the molecular plane (figure 3.13). PCM/TD-DFT calculations on 5BU 2H3OH in methanol indicate

that $S_{\pi\pi^*}$ and S_0 surfaces are extremely close at this Conical Intersection, confirming that this crossing region also exists in solution.

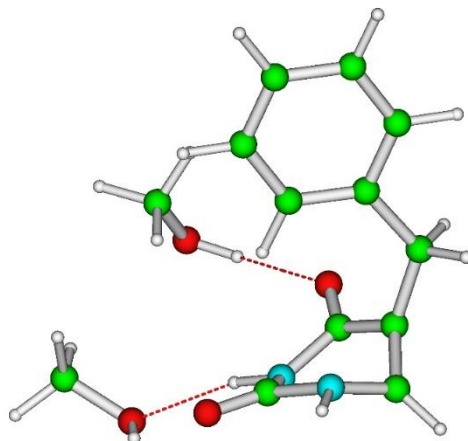


Figure 3.13: Schematic drawing of a representative structure of the Crossing region between S_0 and the lowest energy $\pi\pi^*$ state localized on Uracil moiety

On the opposite, when the two rings are close to a face-to-face arrangement a barrierless decay to another crossing region is found, characterized by a close approach of the two rings (see Figure 3.14).

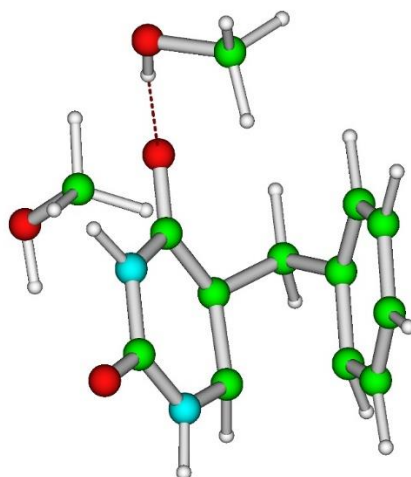


Figure 3.14: Schematic drawing of a representative structure of the Crossing region between S_0 and $\pi\pi^*$ state delocalized on Uracil and Benzene moieties in the path leading to photocyclization (photochemical path)

Ground state geometry optimization soon after the crossing region leads indeed to the photodimerization (photocyclization) product shown in Figure 3.15, which then decays to 56BU by H- atom transfer on a longer time-scale.

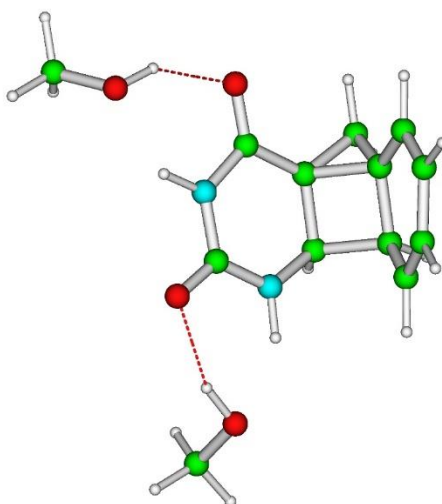


Figure 3.15 Schematic drawing of the photoproduct formed by photodimerization before that H-transfer leads to 56BU

Geometry optimization of S_2 shows that, after crossing S_1 , the system decay to an $\pi\pi^*$ minimum, with a stronger Benzene \rightarrow Uracil Charge Transfer character than in the FC region. This minimum is not much more stable than the CI with S_1 (energy gap < 0.5 eV). Since radiationless excited state deactivation via a CI with S_0 is not predicted to be easy for this state, we can hypothesize the dynamic picture discussed in the following section.

Chapter 4

Time-resolved Measurements on 5BU

**By Time-Correlated Single Photon Counting
and Fluorescence Up-Conversion techniques**

- 4.1. *Time-correlated single photon counting*
- 4.2. *TCSPC technique*
 - 4.2.1. *Count Rates and Single Photon Statistics*
 - 4.2.2. *Timing Resolution*
 - 4.2.3. *Experimental Setup for Fluorescence Decay Measurements with TCSPC*
- 4.3. *Deconvolution of fluorescence decay profiles*
- 4.4. *Nanosecond-resolved fluorescence measurements via*
- 4.5. *Analysis of the signal emitted by 5BU*
- 4.6. *Fluorescence Up-Conversion*
- 4.7. *Up-Conversion technique*
 - 4.7.1. *Sum frequency generation*
 - 4.7.2. *The up-conversion setup*
 - 4.7.3. *Femtosecond laser system*
 - 4.7.4. *Excitation and gate Beams*
 - 4.7.5. *Sample flow*
 - 4.7.6. *Emission collection and time-gating*
 - 4.7.7. *Data treatment*
 - 4.7.8. *Temporal Response of the setup*
- 4.8. *Femtosecond-resolved fluorescence measurements via up-conversion technique on 5BU*
 - 4.8.1. *Sample preparation*
 - 4.8.2. *Experimental conditions*
 - 4.8.3. *Up-conversion results on 5BU*
 - 4.8.4. *Measurements of 5BU fluorescence lifetime at low concentration*
- 4.9. *Interpretation of the Time-Resolved experiments*

4.1. Time-Correlated Single Photon Counting

Time-resolved fluorescence spectroscopy is a powerful analysis tool in fundamental physics as well as in the life sciences. Implementing it in the time domain requires recording the time dependent intensity profile of the emitted light upon excitation by a short flash of light, typically a laser pulse. While in principle, one could attempt to record the time decay profile of the signal from a single excitation-emission cycle, there are practical problems preventing such a simple solution in most cases. First of all, the decay to be recorded is very fast. Typical fluorescence from commonly used organic fluorophores lasts only some hundred picoseconds to some tens of nanoseconds. In order to recover not only fluorescence lifetimes but also the decay shape, typically in order to resolve multi-exponential decays, one must be able to temporally resolve the recorded signal at least to such an extent, that the decay is represented by some tens of samples. For a decay lasting, e.g., 500 ps the signal would have to be sampled at time steps of say 10 ps.

At first glance it might seem reasonable to do this with a photo-diode and a fast oscilloscope or some similar electronic transient recorder. However, the required temporal resolution is hard to achieve with ordinary electronic transient recorders. Moreover, the emitted light may be simply too weak to create an analog voltage representing the optical flux. Indeed, the optical

signal may consist of just a few photons per excitation/emission cycle. Then the discrete nature of the signal itself prohibits analog sampling. Even if one has some reserve to increase the excitation power to obtain more fluorescence light, there will be limits, e.g., due to collection optic losses, spectral limits of detector sensitivity or photo-bleaching at higher excitation power. Ultimately, problems would arise when the observed sample consists of just a few or even single molecules, a situation that is absolutely real in confocal microscopy applications.

The solution for these problems is Time-Correlated Single Photon Counting (TCSPC). With periodic excitation, e.g., from a laser, it is possible to extend the data collection over multiple cycles of excitation and emission. One can then accept the sparseness of the collected photons and reconstruct the fluorescence decay profile from the multitude of single photon events collected over many cycles.

4.2. TCSPC technique

The method is based on the repetitive, precisely timed registration of single photons of, e.g., a fluorescence signal [3, 89]. The reference for the timing is the corresponding excitation pulse. As a single photon sensitive detector a Photomultiplier Tube (PMT), Micro Channel Plate (MCP), a Single Photon Avalanche Diode (SPAD) or Hybrid PMT can be used. Provided that the probability of registering more than one photon per cycle is low, the histogram of photon arrivals per time bin represents the time decay one would have obtained from a “single shot” time-resolved analog recording. The precondition of single photon probability can must be met by simply attenuating the light level at the sample if necessary.

Figure 4.1 illustrates how the histogram is formed over multiple cycles. In the example, fluorescence is excited repetitively by short laser pulses. The time difference between excitation and emission is measured by electronics that act like a stopwatch. If the single photon probability condition is met, there will actually be no photons at all in many cycles. In the example this situation is shown after the second laser pulse. It should be noted that (by the laws of quantum physics) the occurrence of a photon or an empty cycle is entirely random and can only be described in terms of probabilities. Consequently, the same holds true for the individual stopwatch readings.

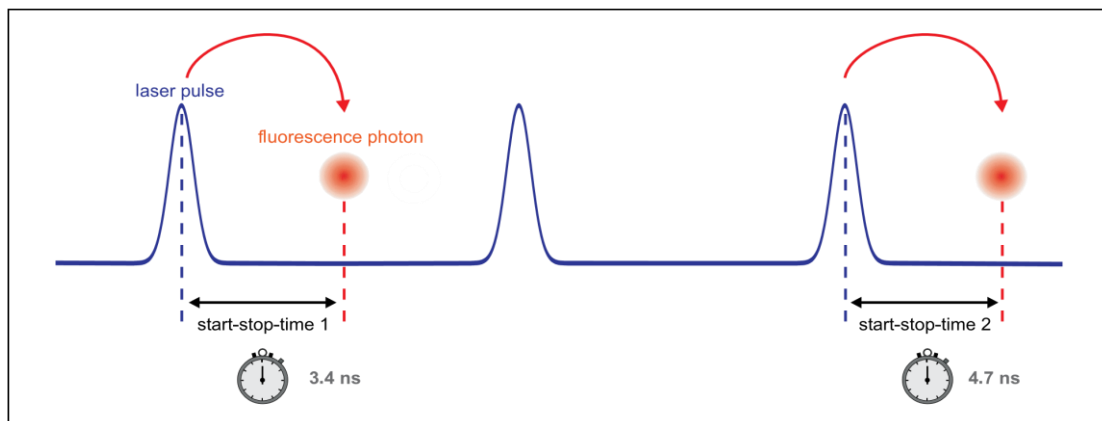


Figure 4.1: Measurement of start-stop times in time-resolved fluorescence measurement with TCSPC.

The stopwatch readings are sorted into a histogram consisting of a range of “time bins”. The width of the time bins typically corresponds to the resolution of the stopwatch but may be chosen wider in order to cover a longer overall time span. The typical result in time-resolved fluorescence experiments is a histogram with an exponential drop of counts towards later times (Figure 4.2).

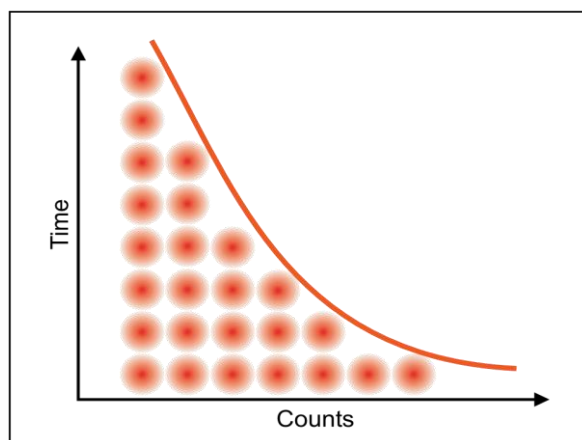


Figure 4.2: Histogram of start-stop times in time-resolved fluorescence measurement with TCSPC.

The reason why there typically is an exponential drop is very similar to that of nuclear decay. As quantum mechanics predict, we have no means of knowing exactly when a nuclear decay will occur. All we can predict is the likelihood of an atomic species to decay in a given period of time. Similarly, all we can predict about the lifetime of an excited state is its statistical expectation. The exponential drop of fluorescence intensity in a single shot experiment with many molecules may be explained as follows: Suppose we begin with a population of 1000 excited molecules. Let the probability of each molecule returning to the ground state be 50 % in the first nanosecond. Then we have 50 % of the excited population after the first nanosecond.

In the next nanosecond of observation we lose another 50 %, and so on. Since the intensity of light is determined by the number of photons emitted in any period of time, it is directly proportional to the surviving population of excited molecules. When the experiment is done with single molecules it is of course no longer meaningful to speak of populations. Nevertheless, the likelihood of observing a photon, i.e., a molecule's return to the ground state as a function of time follows the same exponential drop over time.

It is important to note that we can but need not actually do TCSPC with single molecules. Sufficiently attenuating the light, so that the detector receives only single photons, has the same effect. Indeed, in order to use TCSPC we must attenuate the light to this level. The reason to do so is that a single photon detector can be built with much better time resolution than an analog optical receiver.

In practice, the registration of a photon in time-resolved fluorescence measurements with TCSPC involves the following steps: First, the time difference between the photon event and the corresponding excitation pulse must be measured. For this purpose both optical events are converted into electrical pulses. For the fluorescence photon this is done via the single photon detector mentioned before. For the excitation pulse it may be done via another detector if there is no electrical synchronization signal (sync) supplied directly by the laser. Obviously, all conversion to electrical pulses must preserve the precise timing of the signals as accurately as possible.

The actual time difference measurement is done by means of fast electronics which provide a digital timing result. This digital timing result is then used to address the histogram memory so that each possible timing value corresponds to one memory cell or histogram bin. Finally, the addressed histogram cell is incremented. All steps are carried out by fast electronics so that the processing time required for each photon event is as short as possible. When sufficient counts have been collected, the histogram memory can be read out. The histogram data can then be used for display and, e.g., fluorescence lifetime calculation.

4.2.1. Count Rates and Single Photon Statistics

It was mentioned that it is necessary to maintain a low probability of registering more than one photon per cycle. This is to guarantee that the histogram of photon arrivals represents the

time decay one would have obtained from a single shot time-resolved analog recording. The reason for this is briefly the following: Detector and electronics have a “dead” time for at least some nanoseconds after a photon event. During this time they cannot process another event. Because of these dead times TCSPC systems are usually designed to register only one photon per excitation cycle. If now the number of photons occurring in one excitation cycle were typically > 1 , the system would very often register the first photon but miss the following ones. This would lead to an over-representation of early photons in the histogram, an effect called ‘pile-up’. It is therefore crucial to keep the probability of cycles with more than one photon low (Figure 4.3).

To quantify this demand one has to set acceptable error limits for the lifetime measurement and apply some mathematical statistics. For practical purposes one may use the following rule of thumb: In order to maintain single photon statistics, on average only one in 20 to 100 excitation pulses should generate a count at the detector. In other words: the average count rate at the detector should be at most 1 to 5 % of the excitation rate.

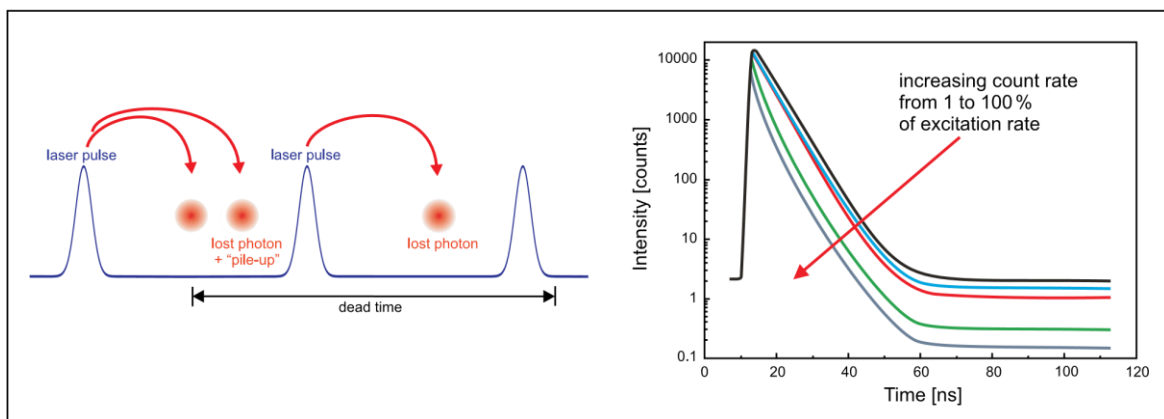


Figure 4.3: Distortion of the TCSPC measurement by pile-up effect and dead time.

It is also worth noting that by virtue of quantum mechanics the actual count arrival times are random, so that there can be bursts of high count rate and periods of low count rates. Bursts of photons may well exceed the average rate. This should be kept in mind when an experiment is planned. Even if an instrument can accommodate the average rate, it may drop photons in bursts. This is why the length of the dead time is of interest too. This quantity describes the time the system cannot register photons while it is processing a previous photon event. The term is applicable to both detectors and electronics. Through pile-up effects dead time can distort the decay histogram and thereby affect the lifetime to be extracted.

4.2.2. Timing Resolution

The characteristic of a complete TCSPC system that summarizes its overall timing precision is its Instrument Response Function (IRF). The basic idea is that if the system is ideal, i.e., has an infinitely sharp excitation pulse and infinitely accurate detectors and electronics, it should have an infinitely narrow IRF. Any deviation from this ideal results in a broadening of the IRF. Before looking into how the individual error contributions add up, the most critical sources are introduced here.

The weakest component in terms of timing resolution in TCSPC measurements is usually the detector. However, as opposed to analog transient recording, the time resolution of TCSPC is not limited by the pulse response of the detector. Only the timing accuracy of registering a photon determines the TCSPC resolution. The timing accuracy is limited by the timing uncertainty the detector introduces in the conversion from a photon to an electrical pulse. This timing error (or uncertainty) can be as much as 10 times smaller than the detector's pulse response. Good but also expensive detectors, notably MCPs, can achieve timing uncertainties as small as 25 ps FWHM. Low cost PMTs may introduce uncertainties of 200 to 400 ps FWHM.

The second most critical source of IRF broadening usually is the excitation source. While most laser sources can provide sufficiently short pulses, it is also necessary to obtain an electrical timing reference signal (sync) to compare the fluorescence photon signal with. Where this signal is derived from depends on the excitation source. With other lasers, e.g., many Ti:Sa lasers, a second detector must be used to derive a sync signal from the optical pulse train. This is commonly done with a fast photo diode. The light for this reference detector must be coupled out from the excitation laser beam, e.g., by means of a beam splitter. The reference detector must be chosen and set up carefully as it also contributes to the overall timing error.

Another source of timing error is the timing jitter of the electronic components used for TCSPC. This is caused by the finite rise/fall-time of the electric signals used for the time measurement. However, the contribution of the electronics to the total timing error usually is relatively small.

The typical approach to measure the IRF is to place a scattering medium in the sample compartment so that there is no fluorescence but only some scattered excitation light reaching the detector. The IRF measurement is not only a means of optimizing and characterizing the

instrument. It also serves as an input to data analysis with “deconvolution” and is therefore a frequent measurement task.

The measured fluorescence decay is the convolution of the “true” physical process of exponential decay with the IRF. With this theoretical model it is possible to extract the parameters of the “true” decay process from the convoluted results in the collected histograms [90]. This is often referred to as “deconvolution” although it should be noted that the term is not mathematically precise in this context. The procedure that most data analysis programs actually perform is an iterative reconvolution.

4.2.3. Experimental Setup for Fluorescence Decay Measurements with TCSPC

Figure 4.4 shows a simple setup for fluorescence lifetime measurements with TCSPC. The laser is running on its internal clock. The light pulses are directed at the sample cuvette, possibly via some appropriate optics. A neutral density filter is used to attenuate the light levels to maintain single photon statistics at the detector. Upon excitation, the fluorescent sample will emit light at a longer wavelength than that of the excitation light. The fluorescence light is filtered out against scattered excitation light by means of an optical cut-off filter. Then it is directed to the photon detector, again possibly via some appropriate collection optics, e.g., a microscope objective or just a lens. The electrical signal obtained from the detector is fed to a pre-amplifier, and then to the TCSPC electronics. In this example the complete TCSPC electronics are contained on a single PC board. The laser driver also provides the electric sync signal needed for the photon arrival time measurement. This signal is also given to the TCSPC electronics.

Of course it is easy to measure long lifetimes with or without reconvolution, since the IRF is of less influence. However, for a precise measurement of short lifetimes one would perform an iterative reconvolution fit taking into account the IRF.

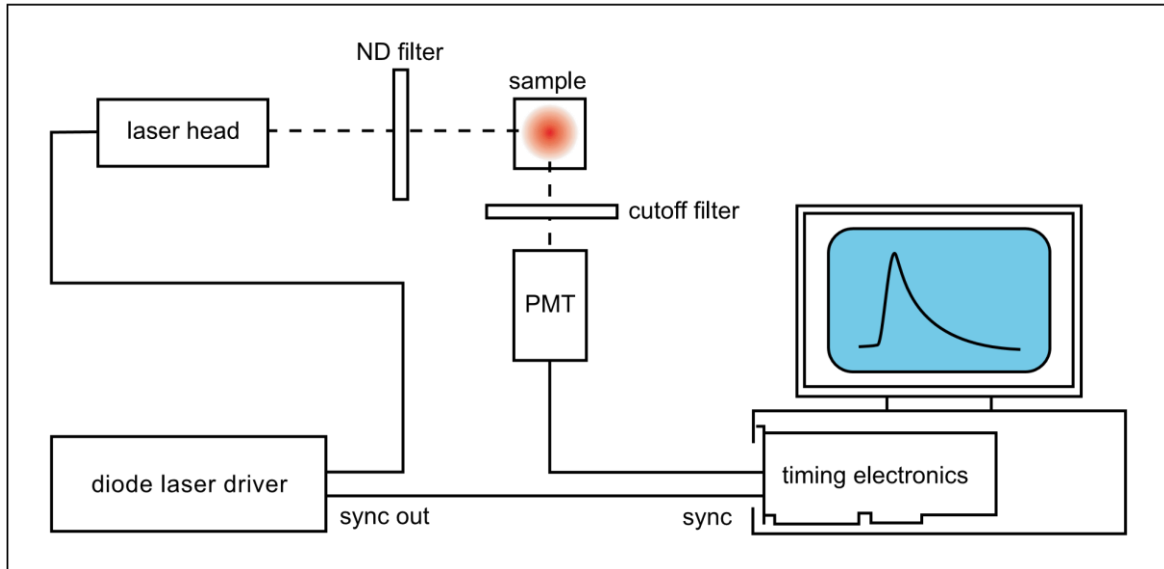


Figure 4.4: Simple experimental setup for fluorescence decay measurements with TCSPC.

4.3. Deconvolution of fluorescence decay profiles

In practice, the excitation pulse is not a delta-function and the instrumentation additionally has a certain electronic response time. This is quantified by the instrument response function, $IRF(t)$, which is the response profile of the instrument to a purely scattering solution. If $IRF(t)$ is considered to be a series of delta-excitation pulses with varying amplitude, then the measured intensity at time t , $N(t)$, is the sum of responses to each delta-excitation pulse up until t . Thus

$$N(t) = \int_0^t IRF(t') I(t-t') dt' \quad (4.1)$$

where $I(t-t')$ denotes the fluorescence intensity from the sample at time t , originating as a response to a delta-excitation pulse at time t' and with amplitude $IRF(t)$. $I(t)$ is described physically using the fluorescence intensity decay models.

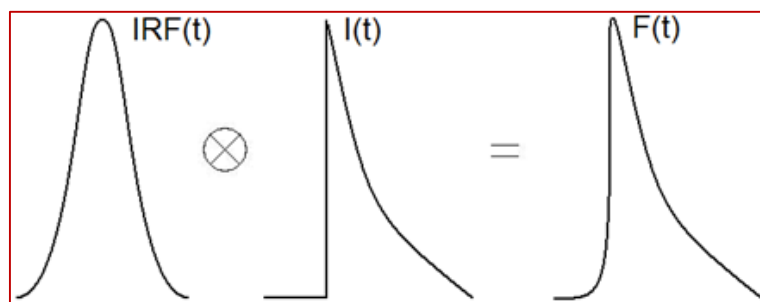


Figure 4.5: Schematic profile of a Gaussian IRF, an exponential decay, and their convolution functions

The equation (4.1) is called the convolution integral (Figure 4.5) and the task is to determine the model, $I(t)$, which yields the best overall fit between $N(t)$ and $IRF(t)$. The fitting procedure is achieved using iterative reconvolution with a least squares analysis. In least-squares the "goodness-of-fit" parameter chi-square is minimized by iteratively optimizing the parameter values of the intensity decay model. There is no actual deconvolution taking place. Rather, the IRF is convoluted with the simulated decay before evaluating chi-square.

4.4. Nanosecond-resolved fluorescence measurements via TCSPC on 5BU

The ns-resolved fluorescence measurements are performed with a Time Correlated Single Photon Counting (TCSPC) system in a collaboration with research group at the Laboratory of Ultrafast Spectroscopy at EPFL. We pump the samples at 266 nm (third harmonic of the Ti:sapphire laser system), with 150 kHz repetition rate, and 3 mW average power. Samples flow into a quartz flow cell of 0.2 mm thickness.

Samples are excited with an average power such that the detected count rate is approximately 1% of the repetition rate, to avoid saturation effects (pile-up effect). The geometry of the excitation is such that the excitation light is prevented to arrive to the monochromator. Detection is performed in a window of 50 ns and no filters are put in front of the monochromator. Corresponding to this window, an IRF of about 200 ps has been measured by detecting the residual light at 400 nm present in the excitation beam that is scattered by the sample.

In Figure 4.6 the spectrum and in Figure 4.7 the kinetic traces for 5BU measured with the TCSPC system are reported. The spectrum is obtained by integrating all counts of the kinetic traces at every wavelength.

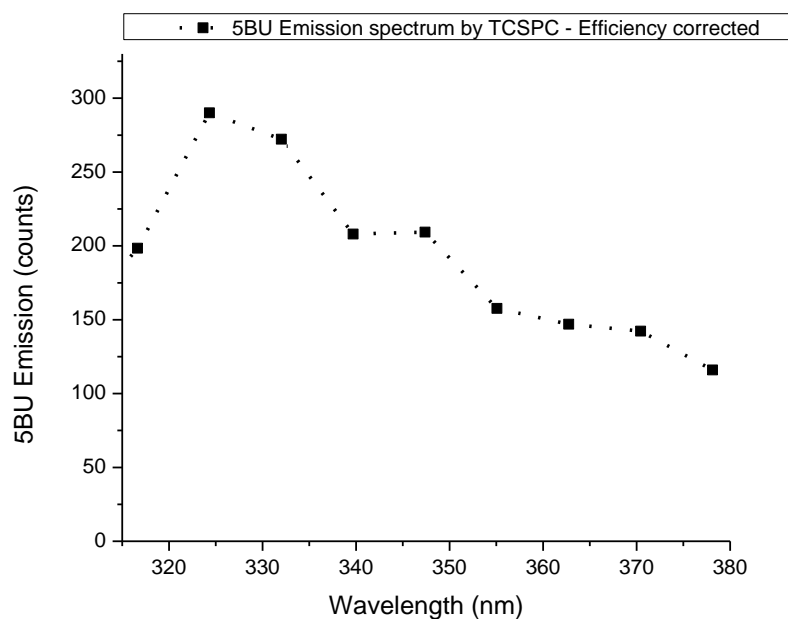


Figure 4.6: TCSPC data for 5BU (a): spectra measured from TCSPC (overall counts are integrated at different kinetic traces).

Kinetic traces of the signal emitted by 5BU at 315 and 365 nm are measured by accumulating data for 1 hour. The temporal dynamics does not change in the measured spectral range. Some of the signal from 5BU is concentrated at very short times and is emitted essentially inside the IRF of the system. There is also some part of it decays more slowly, which can be seen in the plots.

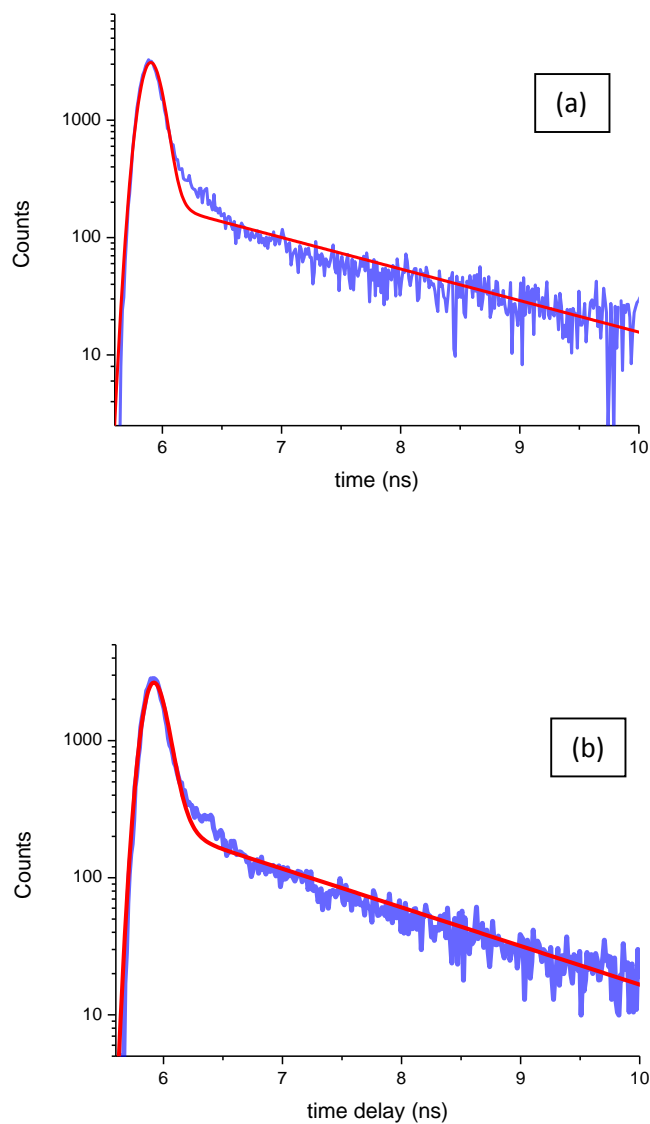


Figure 4.7: TCSPC results on 5BU; Kinetic traces at (a) 315 and (b) 365 nm. The plots in logarithmic scale show the two-exponential nature of the decay curves. Note that this is obtained still without a deconvolution of the IRF.

4.5. Analysis of the signal emitted by 5BU

We fitted the fluorescence signal emitted by 5BU at 315 and 365 nm with a function containing two exponential decays and convoluted with a Gaussian IRF:

$$f(t) = A_1 \text{IRF}(t) \otimes \text{Exp}\left(-\frac{t}{\tau_1}\right) + A_2 \text{IRF}(t) \otimes \text{Exp}\left(-\frac{t}{\tau_2}\right) \quad (4.2)$$

Unfortunately, the IRF in our TCSPC measurements is not exactly a Gaussian function and the convolution should be done numerically with the real IRF. However, this kind of analysis is time demanding and not trivial. The obtained results are shown in Figure 4.7. The time constants, whose estimation has necessarily a statistical error even though it has not been estimated precisely, are reported:

$$\tau_1 = 50 \pm 5 \text{ ps}$$

$$\tau_2 = 1.6 \pm 0.2 \text{ ns}$$

Apart from the longer lifetime that is around 1.6 ns and is well-characterized with these measurements, it turns out that a very fast decay also exists that our estimation for that through fitting procedure is even shorter than the Instrument Response Function of the TCSPC setup. In the next chapter this very fast component is also studied with another technique, fluorescence up-conversion technique, which has a much better temporal resolution and is suitable for shorter decay constants.

4.6. Fluorescence Up-Conversion

Time resolved luminescence spectroscopy is a powerful tool to investigate dynamical behavior of many physical systems in condensed phase. An intense research activity in the past decades have shown that most of non-radiative intramolecular processes as well as most of early intermolecular dynamics occur on the femtosecond to tens of picosecond timescale [91-93]. Since the first experiments with flash lamps (George Porter Nobel prize, 1967), the time resolution has been pushed more and more to these timescales: Nowadays, the most advanced electronic-based detection systems (e.g. fast photomultiplier, time-correlated photon counting, streak camera) reach the picosecond time domain. The subsequent step to fs resolution has been possible only with the advancement of femtosecond pulsed laser technology. This brought a new approach of time-resolved spectroscopy, allowing the development of new techniques based on non-linear optical phenomena, as e.g. sum frequency, four-wave mixing, etc...

The more popular technique is the pump-probe one [94], which consists in probing the changes in absorption after excitation of the sample with a femtosecond pulse. Thanks to a relatively simple implementation it provides both femtosecond resolution and broad-band detection, and gives direct access to ground and excited state dynamics. Indeed, the transient absorption (TA) signal contains contribution from ground state bleaching (GSB), excited state absorption (ESA), and stimulated emission (SE). The overlap of these multiple contributions often makes the interpretation of TA ambiguous, in particular at the earliest times. In this respect, time-gated emission provides a more straightforward signal since it reports only on the emissive, populated excited states. Following the temporal evolution of the emission is therefore the best approach to extract information about excited states relaxation.

4.7. Up-Conversion technique

The concept of femtosecond resolution emission, explained in Figure 4.8, which requires the use of two synchronized pulses, of which the second can be deliberately delayed with the required fs precision. The first pulse is used to excite the sample molecules. The time-dependent emission is then focused onto a non-linear medium. The second gate pulse will mix with the emission, generating a third pulse proportional to the emission intensity. The emission profile is recovered as time slices, with temporal window corresponding to the laser

pulse width. Therefore, varying the delay between the excitation and gate pulse allows full reconstruction of the temporal evolution of the emitting states.

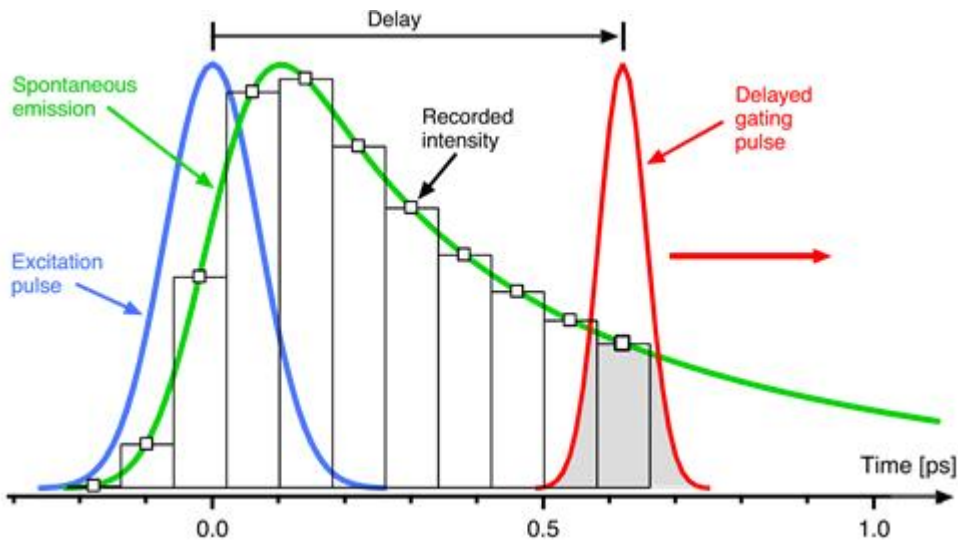


Figure 4.8: Basic principle of time-gated fluorescence techniques. The emitted photons are sliced by the gating pulses in the non-linear medium. The detected signal (squares) directly reflects the time-dependent intensity profile of the spontaneous emission.

Only few techniques allow time-gating of the emission with femtosecond resolution. One is based on the optical Kerr effect [95]: an optical shutter is simulated by two crossed polarizers with an isotropic Kerr medium in between. The emission light is transmitted only when this shutter is activated by a gate pulse that induces optical anisotropy in the Kerr medium. This technique allows both broad-band detection and femtosecond resolution. However, it is not suitable for our requirements, since the detection window does not cover the UV range and the emission polarization is not easily monitored. Another approach, based on non-collinear optical parametric amplification (NOPA) [96], is also not suitable because of a large background contribution and a too narrow spectral detection range.

Finally, the last possibility is the fluorescence up-conversion [97], based on the nonlinear phenomenon of sum frequency (SF) generation. In this technique, the emission is mixed with a delayed gate pulse to generate the SF radiation (Figure 4.9).

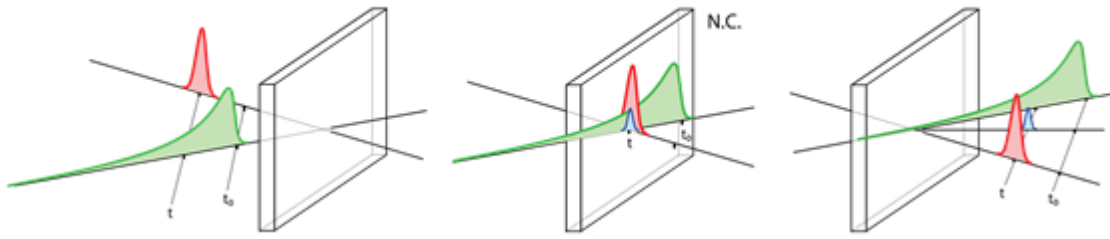


Figure 4.9: Schematic cartoon of the fluorescence up-conversion technique: The sum-frequency signal (blue) is generated only when fluorescence (green) and gate (red) photons are simultaneously present in the non-linear crystal (N.C.).

Owing to the birefringent nature of the non-linear crystal, only a specific emission frequency can be efficiently mixed with the gate frequency for a given crystal angle (phase matching condition). The achievable acceptance bandwidth is inversely proportional to the crystal thickness and playing with this parameter allows to overcome the spectral range limitation. For instance, Schanz et al [98-100]. used a specific non-linear crystal (KDP), thin enough to achieve a large bandwidth. However, this method does not satisfy our requirements. Indeed the sum frequency efficiency of KDP is not high enough in the UV. Moreover, the generated signal intensity would be low since it is proportional to the square of the crystal thickness. We rather employed another method to achieve a broadband detection, which needs the automation of the non-linear crystal phase-matching position. The tilt angle of the crystal was continuously varied during the acquisition at a given delay time, in a way to satisfy the phase-matching condition of all wavelengths of the broad emission spectrum.

4.7.1. Sum frequency generation

Nonlinear optics concerns the nonlinear dielectric response of matter to an applied electric field E . These non-linear contributions to the polarization are described by higher order terms of susceptibility χ [101]:

$$\vec{P} = \varepsilon_0 \left(\chi^{(1)} \vec{E} + \chi^{(2)} \vec{E}^2 + \chi^{(3)} \vec{E}^3 + \dots \right) \quad (4.3)$$

where $\chi(n)$ is the n th order susceptibility. If the electric field is intense enough, nonlinear terms of the polarization P are considered. In our setup, we are using the second order term for the second harmonic generation (SHG), the optical parametric amplification (OPA) and the sum frequency generation (SFG). We are only interested in the sum frequency generation here, at the core of the up-conversion technique. The incident electric fields, corresponding to the fluorescence and gate photons of energy $\hbar\omega_F$ and $\hbar\omega_G$ respectively, are mixed together to produce the up-converted signal of energy $\hbar\omega_S$. Beside the energy conservation law

$$\omega_S = \omega_F + \omega_G \quad (4.4)$$

the momentum conservation law

$$\vec{k}_S = \vec{k}_F + \vec{k}_G \quad (4.5)$$

where k_S , k_F and k_G are the wave vector of the signal, fluorescence and gate beams, constitutes the phasematching condition [100, 102] At this point we need to introduce the phase mismatch parameter Δk , which has to be set to zero to maximize the sum frequency mixing process [97]:

$$|\Delta \vec{k}| = |\vec{k}_S - \vec{k}_F - \vec{k}_G| = \frac{n(\omega_S)}{\lambda_S} - \frac{n(\omega_F)}{\lambda_F} - \frac{n(\omega_G)}{\lambda_G} \quad (4.6)$$

where $n(\omega)$ is the index of refraction at the frequency ω . We can, thanks to the birefringent property of the nonlinear crystal used in our setup, reduce this parameter by tuning the effective refractive index through rotation of the crystal. This condition depends on the polarization of the three beams. We are using the type I phase-matching condition, i.e. with fluorescence and gate electric fields polarized horizontally, implying a vertical polarization of the sum frequency signal.

Another geometrical consideration affects the phase mismatch parameter: the collinearity of the three wave vectors. If the maximum of efficiency is achieved in a perfect collinear configuration (Figure 4.10), we intentionally choose to deviate from this condition, in order to realize a better signal filtering through spatial selection of the up-converted photons.

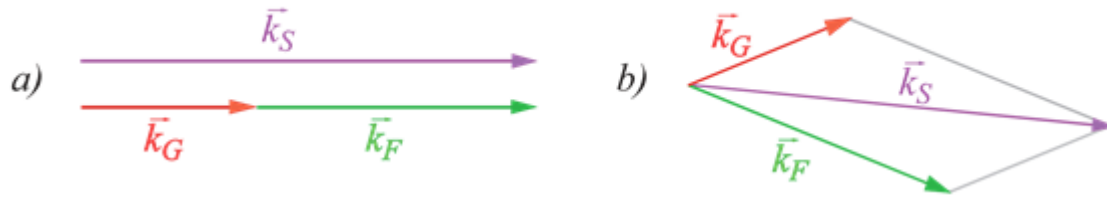


Figure 4.10: a) collinear and b) noncollinear configuration for sum frequency mixing.

Finally, in the low depletion regime, the efficiency of the up-conversion process η is the ratio between the generated and incident numbers of photons, given by the following expression [97, 102, and 103]:

$$\eta = \frac{N_S}{N_F} = \frac{2\pi^2 d_{\text{eff}}^2 L^2 P_G}{c\epsilon_0^3 \lambda_F \lambda_S n(\lambda_F) n(\lambda_G) n(\lambda_S) A} \cdot \frac{\sin^2\left(\left|\Delta\vec{k}\right|L/2\right)}{\left(\left|\Delta\vec{k}\right|L/2\right)^2} \quad (4.7)$$

where d_{eff} is the effective nonlinear susceptibility of the crystal, L its thickness, P_G is the power of the gate beam and A is the overlap area of the mixed beams. The sinc factor in the last equation reflects the effect of a deviation from a perfect phase matching condition, i.e. if $\Delta k = 0$. It gives access to the acceptance spectral bandwidth $\Delta\lambda$. In our experiment, with the use of a 250 μm thick BBO crystal, this value is smaller than 1000 cm^{-1} (~ 25 and $\sim 10 \text{ nm}$ respectively in the Vis and UV), i.e. far too small to cover the entire spectral window we are interested in. As previously mentioned, this limitation is overcome by continuously rotating the crystal during the acquisition, in order to cover a large spectral window.

4.7.2. The up-conversion setup

These measurements have been performed in a collaboration with the ‘‘Laboratory of Ultrafast Spectroscopy’’ at the Swiss Federal Institute of Technology in Lausanne (École polytechnique fédérale de Lausanne; EPFL). This setup at LSU is described in the following:

The 800 nm femtosecond pulses used in our experimental setup were provided by a Ti:Sapphire laser system. The main 800 nm beam was splitted in two branches, one for the pump and the remaining for the gate beam. The excitation pulses were obtained by generating the second

Harmonics of the fundamental (266 nm). The scheme of the time-gated up-conversion setup is presented in Figure 4.11.

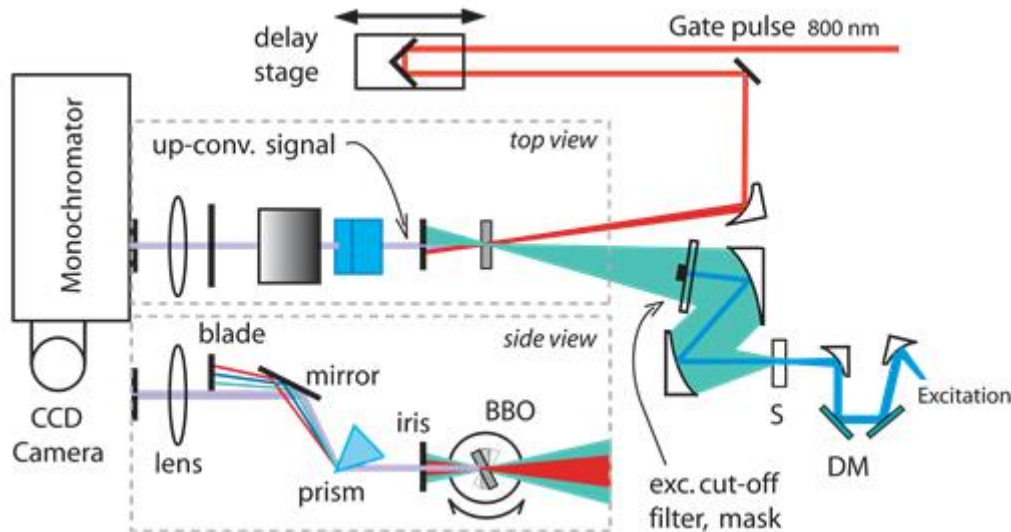


Figure 4.11: Scheme of the time-gated up-conversion experimental setup. The SFG process and the signal filtering parts are shown both from top and side view; realized in the Laboratory of Ultrafast Spectroscopy at EPFL.

After excitation of the sample (S), the spontaneous emission is collected and focused with reflective optics onto a 250 μm thick sum-frequency (SF) crystal. The broad emission spectrum is then time-gated by the delayed 800 nm pulses, throughout the continuous rotation of the SF crystal. After spatial filtering of scattered light, the up-converted signal is dispersed by a grating monochromator and finally detected by a liquid nitrogen cooled, UV-enhanced CCD-camera.

4.7.3. Femtosecond laser system

The ultrafast laser system consists of a set of Coherent oscillator plus amplifier laser. Two Verdi solid-state single frequency Nd:Vanadate laser (diode-pumped) at 532 nm (CW) are pumping the oscillator and the amplifier. The oscillator is a Kerr Lens modelocked Mira-SEED Ti:Sapphire laser that produces wide-bandwidth, femtosecond pulses at 800 nm: Horizontally polarized 3 nJ pulses, created at a repetition rate of 82 MHz. A grating-based stretcher stage broadens the pulses duration to hundreds of ps before seeding the Ti:Sapphire Regenerative Amplifier RegA which selects one pulse at a tunable repetition rate and is set at 150 kHz. After

some round trips in the cavity, each pulse is amplified to a few μ J. The ejected pulses are compressed by a grating-based compressor to 50 fs pulses. These steps are resumed in the Figure 4.12. As a compromise between energy per pulse and average power, we decided to set the repetition rate of the laser system to 150 kHz.

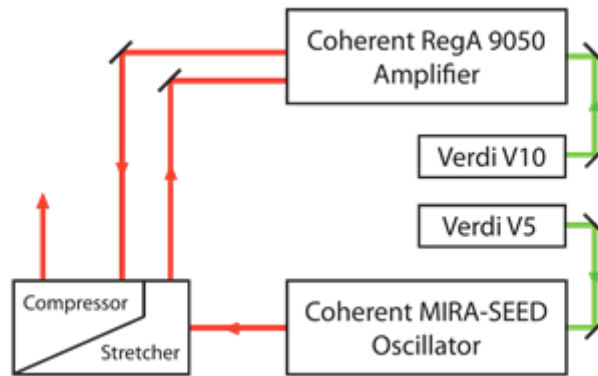


Figure 4.12: Scheme of the Ti:Sapphire oscillator-amplifier femtosecond laser system.

4.7.4. Excitation and gate Beams

The 800 nm pulses leaving the compressor of the main laser system is split in two branches by a 30%/70% beamsplitter. The weaker (reflected) fraction is focused by a lens on a BBO crystal (Beta Barium Borate), in order to obtain the 400 nm SHG signal. Then in the third harmonic generation crystal these 400 nm photons are combined with the fundamental photons at 800 to generate the sum frequency, photons at 266 nm. In both cases parabolic mirrors are used to collimate the generated harmonics and the remaining fundamental was filtered out by two dielectric mirrors. The excitation beam is then focused on the sample. The final average power of this laser beam at 266 nm is about 3 mW with the repetition rate of 150 kHz.

The gate beam is sent in a time delay stage, consisting of a retroreflector mounted on a motorized translation stage, with a feedback position reader. The beam was then focused on the SF crystal.

4.7.5. Sample flow

The high energy per pulse concentrated on a small sample volume (30-40 μm spot diameter) may generate photoproducts, even on very photostable molecules, and prevent us to use a static cell for the experiment. As a result, the sample is flowed through a quartz flow cell, with a speed depending on the sample robustness, excited state lifetime and repetition rate.

The cuvette is also mounted on the sample holder on horizontal motorized translational stages, changing the spot position on the flow cell during acquisition.

4.7.6. Emission collection and time-gating

Emission is collected by a large solid angle parabolic mirror, and focused on the SF crystal with another parabolic mirror (see Figure 4.11). Before the crystal, a long-pass filter (LPF) suited for the excitation wavelength in use, is used to remove the major remaining pump beam intensity. The telescope formed by the two successive parabolic mirrors magnified the excitation spot size by a factor of five, producing an image of the spot of 150-200 μm on the SF crystal. This magnification ratio results from the facts that a large collection angle is needed and that the refocusing is limited by the acceptance angle of the SF crystal. On the other hand, the emission spot size at the SF crystal needs to be slightly smaller than that of the gate, and both spots have to be minimized in order to reduce effects worsening the time resolution as the non-collinear geometry. As a consequence, the magnification ratio is chosen as a compromise between the optimized sum frequency efficiency and temporal response.

The SF crystal is mounted on a motorized rotational stage allowing a rotation amplitude of 40° with respect to the vertical position, corresponding to the phase-matching of a wide wavelength range. The angle is rotated of 20° to cover the 400-700 nm range, whereas it is rotated of 40° to cover the 300-500 nm range. One scan (one rotation) takes 20 seconds.

The non-collinear geometry configuration of the SFG allows an efficient spatial filtering of the main part of emission, gate and residual excitation beams with a diaphragm, positioned after the SF crystal (Figure 4.11). With a fine tuning of its position and aperture size we can select the up-converted signal solely. The signal is vertically dispersed through a quartz prism in order to block with a blade the still remaining scattered light at unwanted wavelengths (Figure 4.11). The up-converted beam is finally focused on the entrance slit of the monochromator by

a UV coated lens. As a compromise between signal intensity, background level due to scattered light and spectral resolution, the slit of the spectrometer is set to between 0.25 and 1 mm. A 600 grooves/mm grating blazed for 300 nm is used to spectrally resolved the up-converted signal, which is detected by liquid nitrogen cooled, CCD camera. On the CCD, the signal is again spatially selected by integrating only the photons acquired in a diagonal strip array of pixels (horizontal dispersion due to the monochromator and vertical dispersion due to the prism).

4.7.7. Data treatment

The data file created by the software monitoring the broadband up-conversion setup is a matrix, with one dimension corresponding to the CCD pixel array, i.e. the wavelength scale, and the other dimension corresponding to the time delay steps. The software delivers also the wavelengths vector (monochromator calibrated with a low pressure mercury lamp) in the up-converted wavelength range. In order to cover the largest time window possible with the smallest number of time steps, specific time files with non-constant step were used.

The raw data matrix is distorted by several effects:

- The high sensitivity of the CCD camera has the disadvantage to also measure cosmic rays, which appear as strong peaks usually localized on one unique pixel but spread over the CCD randomly. These artifacts are removed by replacing the pixel value with the averaged intensity of the neighboring pixel.
- In addition to the electronic background signal from the each pixel, residual scattered light could lead to a wavelength dependent (but time-independent) background. In the time file, several points well before the time zero are acquired, in order to make an averaged spectrum of the background which will be removed to the whole matrix.
- The wavelength file delivered by the software has to be “down-converted”, to obtain the wavelength of the emission before up-conversion. This is done through the formula:

$$\lambda_F = (\lambda_S^{-1} - \lambda_G^{-1})^{-1} \quad (4.8)$$

The presence of dispersive media between the sample and the SF BBO (excitation cut-off filter and flow cell window) induces a wavelength dependent time delay in the emission, due to

group velocity dispersion (GVD). This effect is corrected using an independently measured GVD curve [102, 103].

The data are then corrected for the spectral instrumental response function (irf), and time zero is determined –when possible– on the instantaneous response of the solvent Raman band.

4.7.8. Temporal Response of the setup

The time (*irf*) is inherently related to the excitation and gate pulses duration and is given by the convolution of their time profiles $E(t)$ and $G(t)$, well approximated by gaussians:

$$irf(\tau) = \int_{-\infty}^{+\infty} E(t) \cdot G(t - \tau) dt \quad (4.8)$$

The pulse durations of the laser beams give us the lowest limit of the temporal resolution. The spectral chirp of the fundamental 800 nm beam is compensated by grating compressor (Figure 4.12).

However, two additional effects are contributing to a time elongation of the irf. The first most important contribution stems from the non-collinear geometry adopted to spatially filter out the unwanted excitation and gate beams, resulting in a wave front tilt in the SF crystal. This pulse front tilt increases the spatial overlap of the two beams when scanning the time delays, deteriorating the temporal resolution. The angle between fluorescence and gate beams is set to 5°, as a compromise between signal intensity, filtering and time resolution optimization. Another factor, particularly important in the UV, is the group velocity mismatch (GVM). Due to GVD in the dispersive medium, two interacting pulses with different wavelength do not travel with the same speed. It is the case of the excitation and emission in the sample and the emission and gate beams in the SF crystal. The sample does not contribute much to the GVM effect, because of a quite small wavelength discrepancy between excitation and emission. On the contrary, the SF crystal contributes much more to the GVM since the wavelength of the emission is far from the gate one, in particular for UV detection. The GVM effect can be reduced by the choice of a sufficiently thin SF crystal. For instance, in the UV, the irf can be improved from 370 fs down to 180 fs by reducing the thickness of the BBO from 500 to 250 μm [104].

This irf, finally, is fully described by the up-converted Raman band of a solvent.

4.8. Femtosecond-resolved fluorescence measurements via up-conversion technique on 5BU

4.8.1. Sample preparation

Samples are prepared with 30 mg of 5BU dissolved in 80 mL methanol solution. This concentration provides an optical density of approximately 0.3 at 266 nm in a flow cell of 0.2 mm thickness, which is the desired condition in the up-conversion measurements. Measurements on 5BU are always performed on fresh samples and have lasted no longer than 2 hours. In this way, under the excitation conditions of the up-conversion measurements, we are sure to avoid possible changes of the sample during the measurement, as confirmed by the unaltered static absorption and emission spectra measured before and after the mentioned irradiation time.

4.8.2. Experimental conditions

Similar to the case of TCSPS measurements, the samples is pumped at 266 nm, with 150 kHz repetition rate and 3 mW average power. Samples flow into a quartz flow cell of 0.2 mm thickness. Wavelength - time delay (2D) plots in the range 280-390 nm have been measured for fresh 5BU sample.

The red part of the spectrum is measured by putting a long pass filter at 290 nm to block the pump and reduce the background noise. The spectral response of the system in this spectral region is corrected by measuring the fluorescence of two reference organic dyes; 2,5-diphenyloxazole (PPO), and para-terphenyl (PTP).

In order to measure the blue part of the spectrum, no filter is used to block the pump: this provides more noisy results. The spectral response of the system in this spectral range is corrected by measuring the fluorescence of a reference dye emitting more in the blue; 1,2-diphenylacetylene (DPA).

The group velocity dispersion in the resulting 2D plots is then corrected. In the end the two plots are linked at around 325 nm. A region where the two plots are overlapped is identified. Here, the fluorescence signal in both plots is compared and brought to the same value. Then,

the final plot is obtained by reconstructing this intermediate region: in particular, one attributes a linearly changing weight to the signal belonging to the two plots when passing from the blue to the red region.

The IRF of the system is determined by measuring the temporal evolution of the Raman signal scattered from water. It provides an IRF of 300 fs.

4.8.3. Up-conversion results on 5BU

We first looked only at the fluorescence emitted by 5BU at 310 nm and observed that the signal detectable with fluorescence up-conversion goes to zero in the first 10 ps, as confirmed by Figure 4.13.

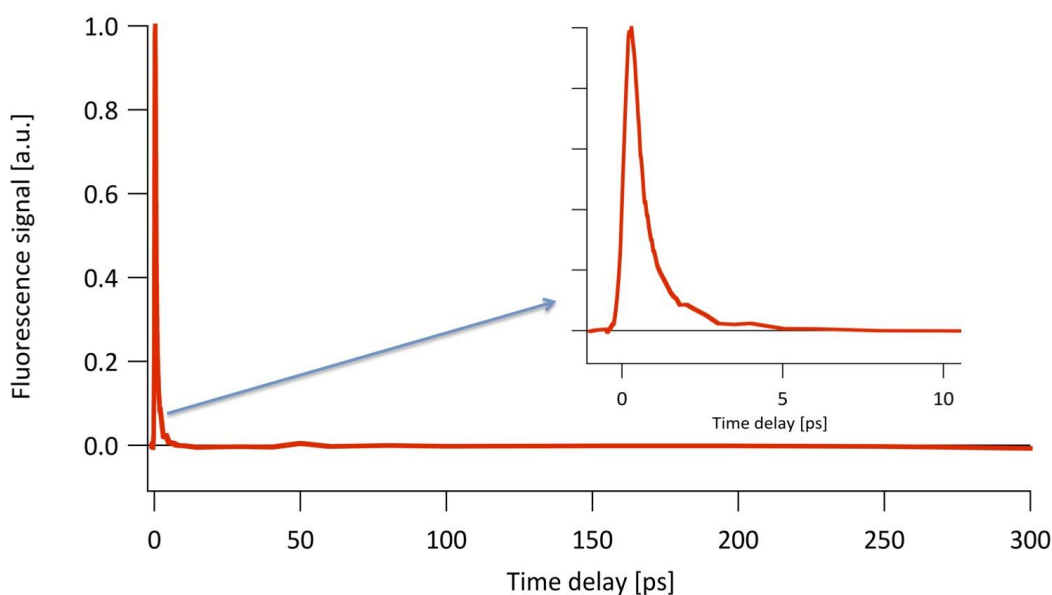


Figure 4.13: Kinetic trace at 310 nm for the signal emitted by 5BU.

Then, we measured the complete 2D plot for 5BU in the region 280-390 nm, which is shown in Figure 4.14. Corresponding transient spectra and kinetic traces are reported in Figure 4.15. The blue part of the plot is noisier, because of the measurement conditions described above.

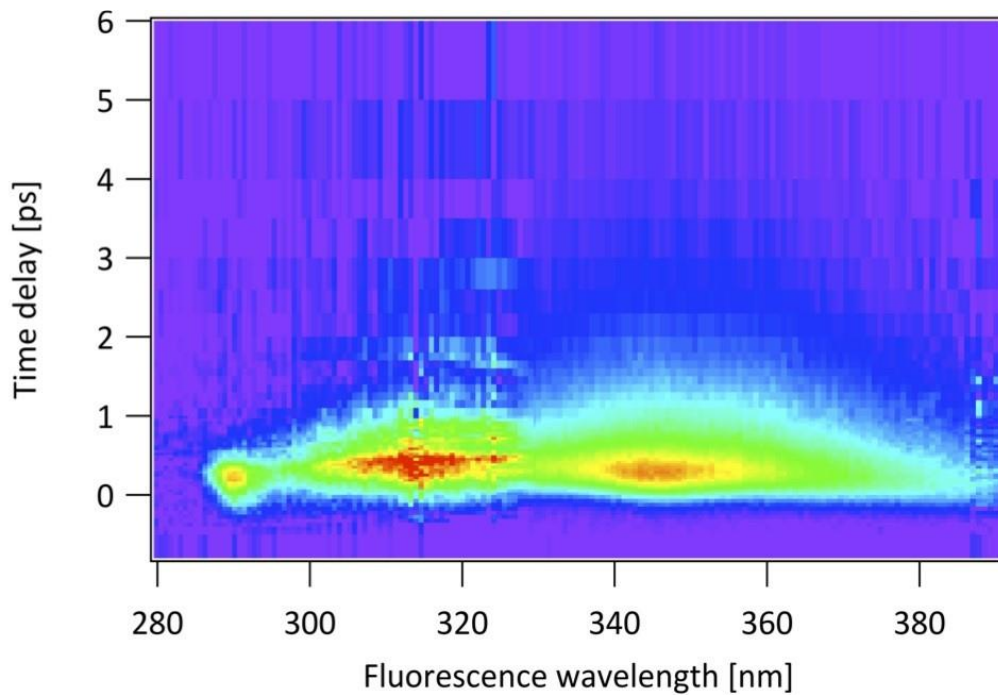


Figure 4.14: Wavelength-time delay plot of 5BU.

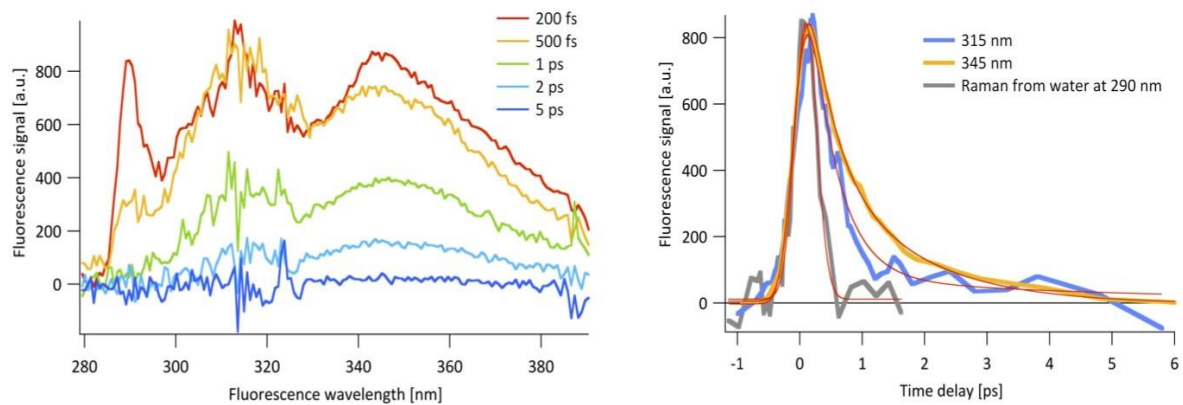


Figure 4.15: Data from plot wavelength - time delay of 5BU. Left: transient spectra. Right: kinetic traces.

The accumulation of signal at 295 nm corresponds to the Raman scattering of the excitation light. The main result of this measurement is that the emission at ultrafast time scales from photoexcited 5BU is limited to some picoseconds. The 5BU emission is characterized by the appearance of two bands peaked approximately at 315 and 350 nm already at short time delays.

The band in the blue seems slightly narrower with respect to the one in the red and shows at short time delays (spectra at 200 fs and 500 fs) a slightly higher relative weight with respect to the other one. At other time delays the two bands have similar level of signal.

The decay at 315 nm is slightly faster than at 350 nm. A single exponential fit provides a decay of 0.5 ps in the blue part and 0.8 ps in the red one. At 5 ps the signal is almost zero at all wavelengths.

The appearance of a strong band at 350 nm is very surprising, considering that it is not present in the steady-state emission. The presence of the relatively strong signal in the red part of the spectrum have been confirmed by different measurements repeated in this region.

We calculated a number of photons absorbed by a single 5BU molecule per excitation pulse of 0.006, making very unlikely the possibility that we are observing 5BU molecules photo-converted into 56BU, considering the low probability of photo-cyclization calculated in the previous chapter.

4.8.4. Measurements of 5BU fluorescence lifetime at low concentration

We have investigated the dependence of the dynamics of the 5BU fluorescence on the sample concentration. These tests can shed light on the eventual formation of aggregates at higher concentration. In particular, we have measured the signal emitted at 315 nm and at 360 nm, corresponding to the two emission bands observed in the 2D plots described above, from 5BU samples with dilution factors of 10 and 100 with respect to the solution adopted in the previous up-conversion measurements (30 mg in 80 ml MeOH). This levels of dilution have been chosen in order to perform measurements with a reasonable S/N ratio.

In Figure 4.16 the kinetic traces at both wavelengths for the samples with dilution factor 1, 10 and 100 are shown. At both wavelengths the dynamics does not change with the concentration. A solution with dilution factor of 1000 has also been tested: in this case the kinetic traces at the two wavelengths (not reported in Figure 6) are very noisy, especially the one at 315 nm, because of the very low level of detected signal. However, the traces even for such low concentrated solution essentially confirm the same dynamics.

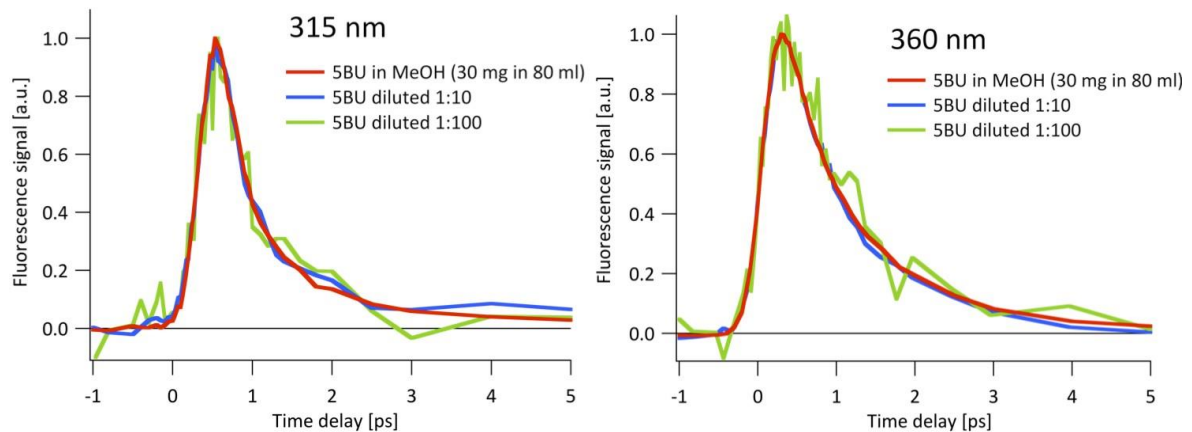


Figure 4.16: Kinetic traces at 315 nm (left) and 360 nm (right) of the signal emitted by 5BU for dilution factors 1, 10 and 100.

In Figure 4.17 (left) the maximum values of fluorescence are reported at both wavelengths as a function of the sample concentration and are normalized to the maximum of them. At a specific wavelength the measurements are performed with the flow cell at a fixed position and with a quite constant value of the pump power. Thus, the efficiency for the measurements of the three different concentration values can be considered approximately the same. The signal emitted by the 5BU increases linearly with the concentration.

These results do not show aggregation effects at the first concentration we used; that would have produced a concentration-dependent dynamics or a nonlinear drop of the fluorescence signal at 360 nm.

Figure 7 (right) compares the dynamics of 5BU at the two considered wavelengths for the not diluted sample. This measurement confirms the results reported in Figure 4.15 with better statistics.

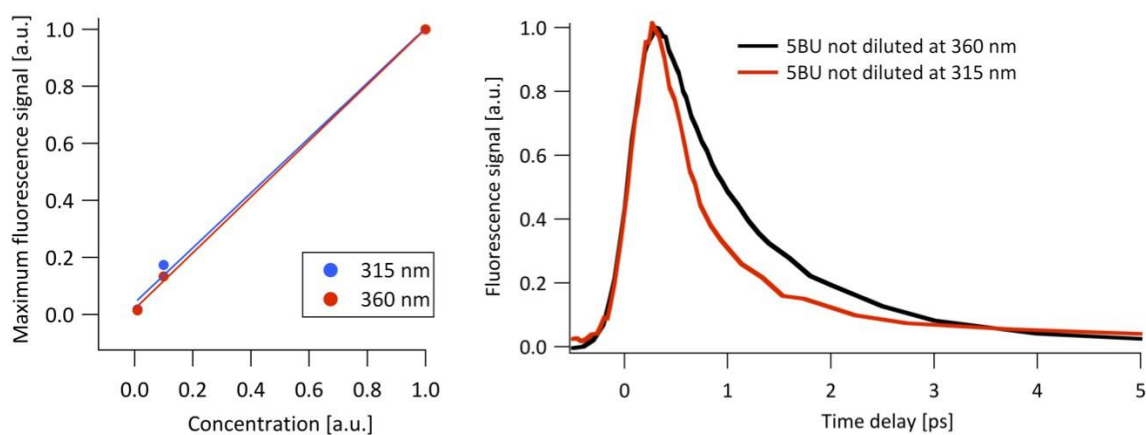


Figure 4.17: (Left) Maximum value of the fluorescence signal as a function of the concentration of the 5BU sample. Errors have the size of the markers. The experimental points at the two wavelengths for the dilution factors 1 and 100 overlap. (Right) Comparison between the kinetic traces at 315 nm and 360 nm for the not diluted 5BU sample.

4.9. Interpretation of the Time-Resolved experiments

The “fast” features (fluorescence decay lifetimes of about 0.5 and 0.8 picoseconds) evidenced in Upconversion experiments are associated to the part of the Wave Packet decay on the $S_{\pi\pi^*}$ surface populated by the photoexcitation

The “slow” features (nanosecond decay lifetime measured by time-correlated single photon counting technique) is always due to transition from the $S_{\pi\pi^*}$ state, but related to the part of the excited state population that is first trapped in the S_2 minimum, and in a nanosecond time scale with a nonradiative decay to $S_{\pi\pi^*}$ and from there to S_0 through fluorescence.

The above mentioned deactivation routes from the excited states of 5BU molecule to its ground state is shown in figure 4.18.

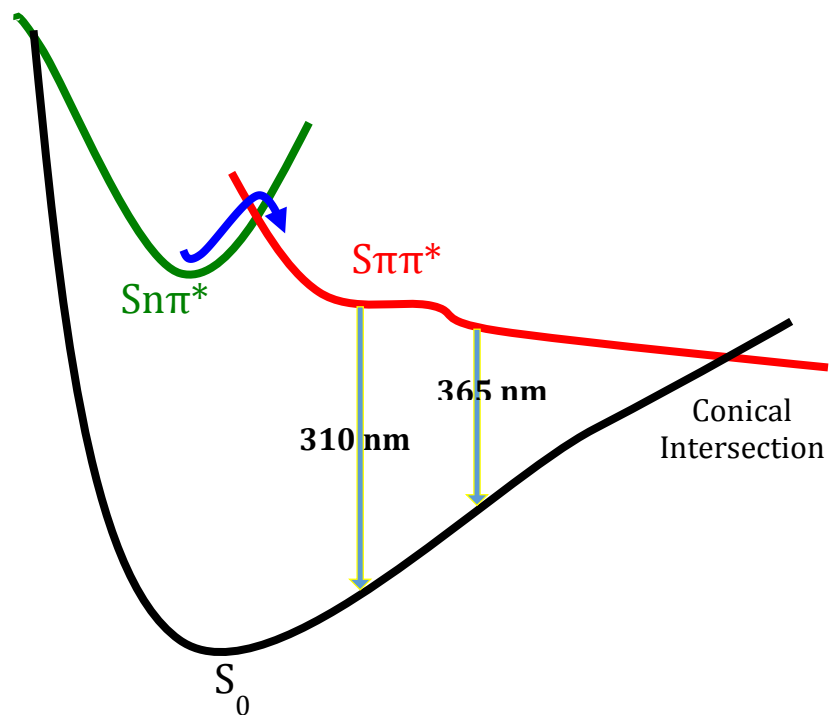


Figure 4.18: Potential Energy Surface (PES) of ground state (S_0) and the first two excited states ($S_{\pi\pi^*}$ and $S_{n\pi^*}$) for 5BU molecule, and the deactivation routes.

Chapter 5

Temporal and Spectral Characterization of Femtosecond UV Pulses

- 5.1. *Femtosecond UV pulses*
- 5.2. *Experimental setup*
- 5.3. *Analysis of the results*
- 5.4. *Pulse duration and chirp*
- 5.5. *Spectral characterization*
- 5.6. *Linear optical methods for characterization of femtosecond UV pulses*

5.1. Femtosecond UV pulses

The key role of femtosecond laser systems in the study of molecules is mentioned in the previous chapters. Ultrashort laser pulses in the UV domain were especially important in our experiments; where their features determine important parameters of the apparatus. Despite such a widespread use, the characterization of UV fs pulses turns out to be still much more demanding than what happens for the visible and near infrared spectral windows.

Several methods, used in the visible and near infrared, in fact, fail in the deep UV, below 300 nm wavelength, due to the lack of suitable crystals needed for implementing autocorrelator-like devices to measure the pulse duration and, possibly, to characterize the pulse temporal shape [105]. When seeking for a second-order autocorrelator to retrieve the pulse duration, the resulting second harmonic would be in the vacuum UV (VUV) and therefore hard to handle in any case, imposing very thin nonlinear crystals, characterized by a low conversion efficiency, to avoid severe GDD in the deep UV [106-109]. Other techniques can also be implemented, such as sum-frequency or difference-frequency generation, but they require an additional auxiliary pulse of comparable shortness and known duration [105, 110]. Lately, however, a shaper-assisted cross-correlation setup was introduced that does not need external references, additional pulses and spectrometers. This device employs a two

dimensional shaper that works in the UV and uses a solar blind multiplier as nonlinear detector [111].

As a matter of fact, for spectroscopic studies and day to day application a much simpler and cheaper setup is needed to monitor UV pulse length and possibly retrieve any temporal chirp. A number of techniques have been tested to directly characterize UV pulses based on the induction of transient-gratings (TG), on self-diffraction (SD) or polarization gating (PG), successfully transferred to the UV spectral region [112, 113].

For spectroscopic applications to bulk materials, especially in liquid phase, two-photon absorption (TPA) [114] induced by fs pulses of even moderate energy can be an effective method to realize a simple, user friendly, and cheap autocorrelator. In this case pump and probe pulses, both derived from the pulse to be characterized, are spatially overlapped into a suitable nonlinear medium. Both beams are individually depleted due to TPA occurring into the medium, but when temporal overlap is achieved between the two pulses an additional TPA contribution arises with one photon absorbed from each beam. This two-beam contribution constitutes the autocorrelation signal [105, 115]. Besides being cheap and simple to implement, TPA based methods have also the advantage to be tuneable in a broad spectral window: for example, in [116] the authors claimed TPA-based autocorrelator is applicable in the 220 nm – 550 nm spectral range, whereas fs pulses in the range 195 nm – 330 nm have been characterized in [105].

We implemented a TPA-based autocorrelator - potentially also crosscorrelator - to measure the duration and the chirp of UV fs pulses at approximately 260 nm. We compare the measured value of the UV pulse duration with its Fourier limit, which was directly retrieved by measuring the spectrum of the UV pulses. We find the pulse to have a non-negligible chirp.

Moreover, we also characterize the spectral features of the UV pulse transmitted through the sample, and find that both spectral FWHM and center of gravity, i.e. central wavelength, are modulated as a function of the time delay between pump and probe.

We also used a linear method as a high-resolution alternative to spectrometry for the determination of the minimum duration of UV femtosecond pulses. This is typically an essential information to extract the amount of chirp of such pulses. This method is based on the spatial interference of the pulse beam with itself, and on the quantitative estimation of fringes visibility.

5.2. Experimental setup

We set up a TPA-based autocorrelator to measure UV femtosecond pulse duration and used a solid crystalline medium, such as quartz (suprasil), as TPA target having a TPA coefficient $\beta \approx 2 \times 10^{-11}$ cm/W at 264 nm when measured with 200-fs pulses [117]. We stress here that the choice of quartz as TPA, despite its β coefficient is much lower than that of other materials, especially liquids such as methanol and water, was dictated, by its easy availability and by the characteristic of quartz and transparent media to have the coherent electronic part of the TPA transient signal as dominant with respect to the other two components, i.e. sequential absorption and Raman [118]. This makes retrieving the chirp of the pulse easier with quartz than with liquids. This is obtained by analyzing the spectral features of pulses transmitted through the TPA target, as we will show in the end of the fifth section. In fact, the shape of the TPA signal versus time delay between pump and probe is typical in crystalline media, and is essentially determined by the instantaneous electronic response of the material [119].

A layout of our experimental setup is shown in Figure 5.1. 1030-nm fundamental pulses emitted at 2 kHz repetition rate by a custom version of a PHAROS laser source, based on the Yb:KGW active medium (Light Conversion [120, 121]), carrying between 0.5 and 1 mJ pulse energy with a duration of about 170 fs, were converted into IV harmonic pulses (≈ 257 nm) by two sequential frequency doubling BBO-based stages (HIRO).

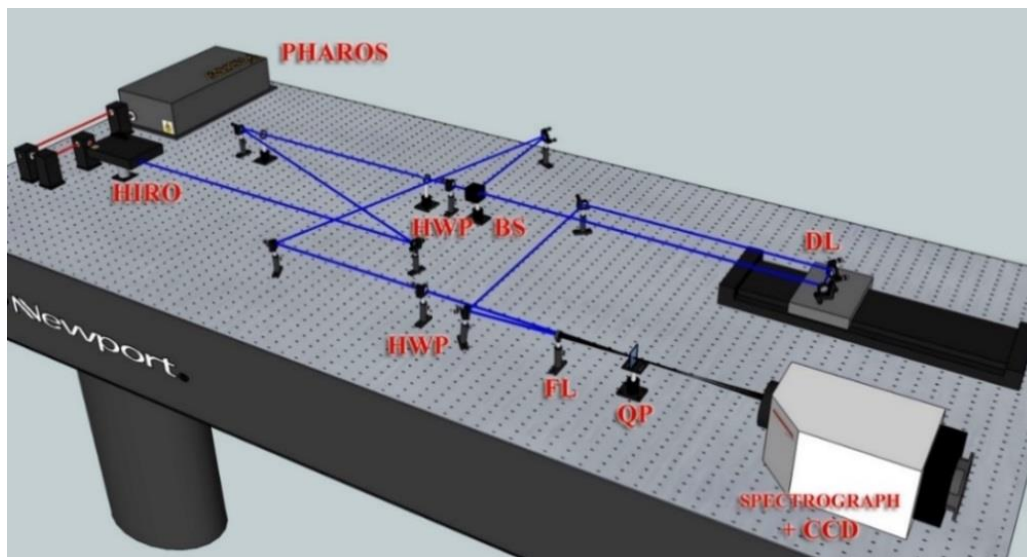


Figure 5.1: General view of the experimental setup of the TPA-based autocorrelator.

Differently from most common cases, we carry out a temporal characterization of the IV harmonic pulses for high conversion efficiencies, corresponding to quite high energy pulses.

Such pulses are typically needed in nonlinear spectroscopy and nonlinear optics experiments. As a consequence, a non-negligible chirp arises which lengthens such pulses and makes necessary to combine a non-trivial pulse duration measurement with an accurate determination of the spectral bandwidth. The conversion efficiency in the first nonlinear stage is $\approx 35\%$, whereas that one in the second stage ranges between ≈ 20 and 30% . These regimes are far from the so called Lowest-Order-Perturbation-Theory (LOPT) case [122], where the intensity of the 2-nd harmonic, I_2 , scales as $I_2 \approx I^2 \cdot L^2$ in terms of the intensity of the fundamental, I , and the length, L , of the nonlinear generating medium. In our regime the duration of the SH pulse, τ_2 , is not related anymore to the duration, τ , of the fundamental by the simple relation $\tau_2 \approx \tau/\sqrt{2}$, which holds rigorously true for Gaussian-like pulses.

The energy of the UV pulses typically ranged within approximately 50 – 150 μJ . UV pulses were then sent to the TPA-based autocorrelator. The UV beam was first split into two beams by means of a BBO, 8-mm side, polarizer beam-splitter cube (BS in the Figure 5.1). A lambda-half waveplate (HWP) was placed just before the beam-splitter in order to rotate the polarization of the incoming beam in such a way to adjust the intensity ratio between the two beams in the nonlinear medium. Pump and probe beams, forming an angle of about 2° , were focused by means of a 40-cm focal length fused silica lens (FL) which implied a ≈ 3 cm Rayleigh length. A fused silica plate (QP), acting as the nonlinear medium, was not placed right at focus, but rather some ≈ 20 cm far apart from focus in order to reach the appropriate pulse intensity range and ensure for the two beams to be spatially overlapped all along the interaction region. The estimated overall peak intensity in the plate fell within the ≈ 50 -150 GW/cm^2 range, depending on the particular experimental condition chosen for the experiment, the beam radius and the retrieved actual pulse duration being ≈ 0.5 mm and ≈ 250 fs, respectively. The temporal overlap of the pump and probe pulses was achieved by a 60-cm optical delay line (DL) based on a computer-driven motorized micropositioner with a resolution of $0.1 \mu\text{m}$ and unidirectional repeatability of $0.2 \mu\text{m}$. Another HWP is inserted in the probe path before combining the two pulses into the suprasil plate, in order to make parallel pump and probe polarization. The TPA signal was measured by detecting the absorption of the only probe pulse by a high efficiency analysis/detection apparatus specifically meant for UV radiation. This is constituted by a spectrograph equipped with a grating, having 600 gr/mm and blazed for 300-nm radiation, and a cooled tinned back illuminated CCD, sensitive in the UV range. The overall quantum efficiency of the detection apparatus at 260 nm was estimated to be $\approx 35\%$, resulting from the 50% efficiency of the grating and the excellent 70% quantum efficiency of the CCD. The CCD has 1024x122 pixels, each being a square of $24\text{-}\mu\text{m}$ side, and is interfaced to a

computer controlling the data acquisition procedure. Each data point is the average over only ten laser shots, so to be fast in storing the signal in each selected experimental condition, thanks to the high stability of our laser source. In fact, the fluctuation and possible drift of the pulse IR energy was confined within 1% on the typical measurement session, and continuously monitored shot by shot during the whole experiment. This suggests that even the UV pulse duration was likely pretty stable all along the measurement, making more stable the TPA signal level itself and, in turn, the reliability of the measurement procedure.

5.3. Analysis of the results

A typical autocorrelation curve of our 257-nm pulse is shown in Figure 5.2(a). The shape of the curve, with two left and right side overshoots surrounding a main central two-photon absorption peak around a zero delay time, $t_d = 0$, is typical of transparent media [119], where the electronic part of the transient non-resonant response to excitation is 5-6 times higher in magnitude than that from low-frequency vibration [119, 123]. In particular, in fused silica high-frequency vibrations are weak and the transient response mainly contains the instantaneous electronic contribution to the medium optical density [119]. The measured transmittance ratio refers to the area of the transmitted probe spectrum in the presence of the pump pulse normalized to the transmitted spectrum with no pump. This typical shape also represents a first indication of the presence of a consistent linear chirp, as for chirp-free pulses the fused silica response would be expected to resemble a dispersive-like curve behavior roughly centered at $t_d = 0$. The modulation of the TPA signal versus t_d can be physically ascribed to the dynamical interplay in the fast electronic TPA response, where electrons absorb one photon per pulse from both pump and probe, due to the chirp-induced spectral modulation of the pulses versus t_d . In such conditions the TPA frequency-dependent signal, $A(\omega, t_d)$, can be best-fitted by a function of the form [118]:

$$A(\omega, t_d) = c_1 F_{ac}(\omega, t_d) + c_2 \frac{\partial}{\partial t_d} F_{ac}(\omega, t_d) + c_3 \frac{\partial^2}{\partial t_d^2} F_{ac}(\omega, t_d) \quad (5.1)$$

where the autocorrelation function, $F_{ac}(\omega, t_d)$, reads:

$$F_{ac}(\omega, t_d) = \left| \int dt e^{-i\omega t} E(t) E(t - t_d) \right|^2 \quad (5.2)$$

c_1 , c_2 , and c_3 being best-fit coefficients and $E(t)$ the electric field of the pulse in the temporal domain. For Gaussian temporal shapes, as assumed here below, Eq. (2) essentially simplifies to $F_{ac}(\omega, t_d) \approx \exp\{-t_d^2/\tau_p^2\}$, τ_p being the pulse duration, i.e. the FWHM of the intensity, and $t_d = 0$ was set at the transmittance minimum.

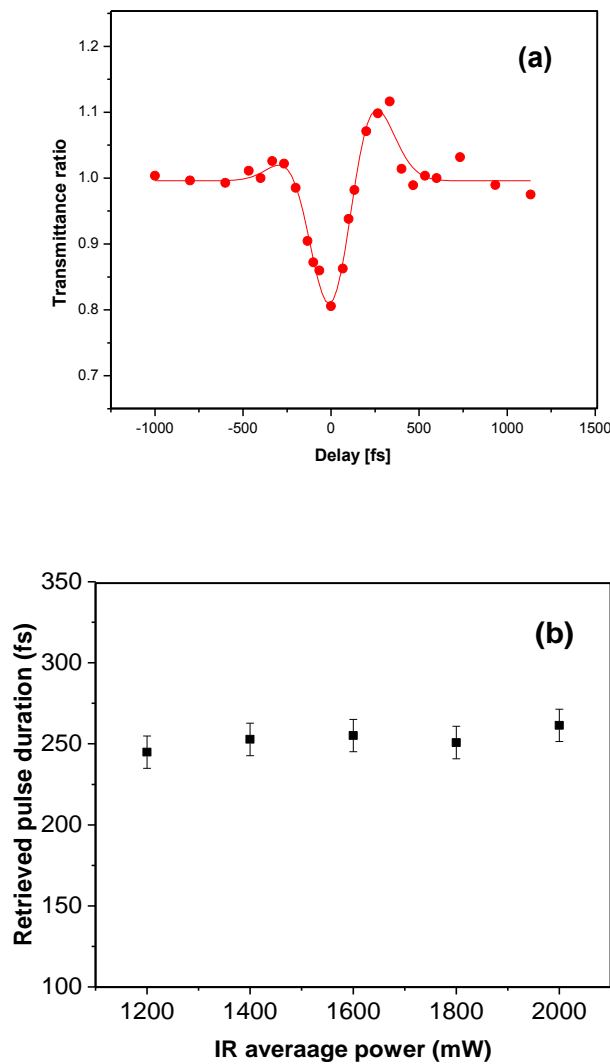


Figure 5.2. (a) Typical curve of the sample transmittance versus the delay time between the pump and probe pulses. Solid line is the best fit to the experimental points obtained by using the fitting function described through the text. (b) Retrieved pulse duration versus the fundamental IR average pumping the HIRO harmonic generator module.

In the Figure 5.2(b) we report the retrieved pulse duration as a function of the average IR power delivered by the PHAROS system to the harmonic generator. This power corresponds to a IR intensity in the first doubling stage in the 100 – 200 GW/cm², the IR beam waist on the

BBO crystal being ≈ 1 mm. For such intensities, with a measured flat conversion efficiency to the II harmonic amounting to about 35 %, the intensity of the 2nd harmonic beam onto the 2nd BBO crystal ranged within ≈ 7 -20 GW/cm², resulting in a conversion efficiency from the 1st to the 4th harmonic moderately increasing from ≈ 11 to 13%.

It is interesting noticing that the conversion efficiency from 1030 to 515 nm is nearly flat and equal to about 35% over the entire investigated range of the fundamental peak intensity, whereas for the fourth harmonic generation process, which results from two serial 2nd harmonic generation stages, it linearly increases from ≈ 5 to ≈ 12 % below 120 GW/cm², while it saturates above such a IR peak intensity (figure 5.3). This is an indication that the first doubling stage operates in a fully saturated regime where significant depletion of the fundamental pulse occurs within the nonlinear crystal, whereas the 2nd doubling stage reaches such regime only above 120 - 130 GW/cm². Running the harmonic generator in this regime, where the highest harmonic pulse energies are reached, can be necessary when specific nonlinear optics applications are pursued, such as atmospheric nonlinear optics and filamentation [124] or nonlinear biophotonics [125], which can demand for relatively high energy UV laser pulses.

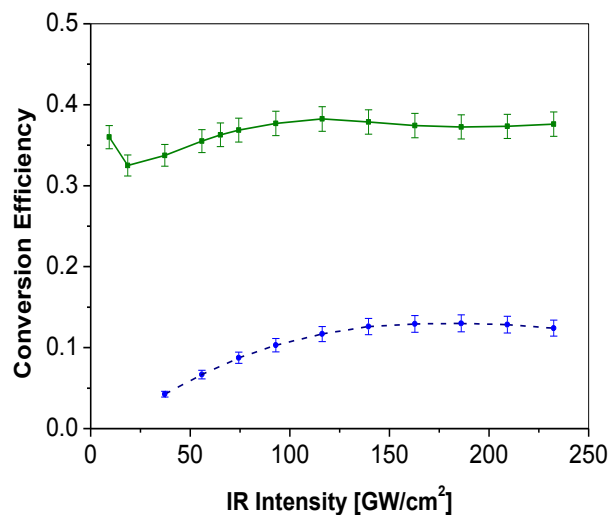


Figure 5.3. Measured conversion efficiency of 2nd (515 nm, green squares – solid line) and 4th (257 nm, blue circles – dashed line) harmonic versus fundamental peak intensity.

5.4. Pulse duration and chirp

The measured pulse duration amounted to about 250 fs with an uncertainty of ± 10 fs over the entire investigated range of IR fundamental intensities. Such determination was then corrected for systematic pulse lengthening due to GDD into the crossed optics of the setup. If τ_p is the measured pulse duration and $\tau_p^{(0)}$ the non-stretched duration of the pulse entering the TPA setup, their relation for Gaussian pulses can be written as [105, 122]:

$$\tau_p = \tau_p^{(0)} \sqrt{1 + \left(\frac{4 \ln 2 L \lambda_0^3}{2 \pi c^2 \tau_p^{(0)2}} \frac{d^2 n(\lambda_0)}{d\lambda^2} \right)^2} \quad (5.3)$$

By considering that $d^2 n(\lambda=257 \text{ nm})/d\lambda^2$ is about $20 \mu\text{m}^{-2}$ for BBO and $8 \mu\text{m}^{-2}$ for fused silica [105] and that the beams travels through 8 mm BBO thickness in the splitter and an overall 6 mm of fused silica, including waveplates and the focusing lens, we estimate the total pulse lengthening due to GDD to be ≈ 7 fs, so that $\tau_p^{(0)} \approx 240 \pm 10$ fs.

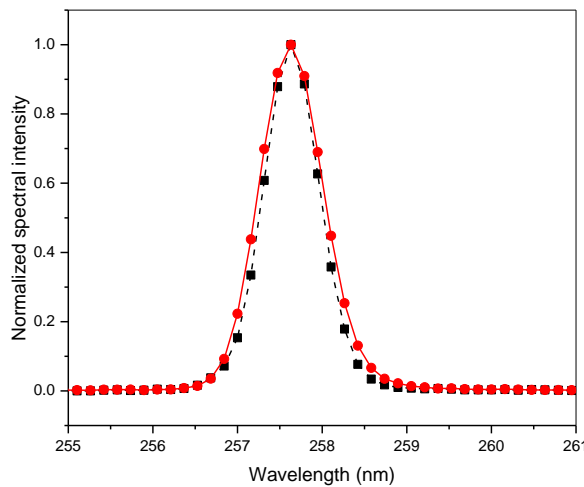


Figure 5.4. Measured power spectra of the 4th harmonic pulses for 1200 mW (red circles, solid line) and 100 mW (black squares, dashed line).

We then measured the UV pulse spectrum in order to find out the Fourier limit for the pulse duration, $\tau_p^{(F)}$. This was carried out by replacing the grating of the spectrograph with a UV-dedicated grating having 1200 gr./mm blazed at 330 nm, thus giving a spectral resolution of ≈ 0.16 nm. A typical spectrum is shown in Figure 5.4 for the 4th harmonic pulse generated when the average power of the fundamental IR radiation pumping the harmonic generator is 1.2 W (red circles) in comparison with the spectrum of the minimum-energy UV pulse, obtained

when the harmonic generator is pumped by 100 mW of 1030 nm radiation. The comparison allows one to rule out the influence of other nonlinear effects but TPA, possibly occurring into the target and the other optics of the setup which could spectrally broaden or distort the pulse, such as self- and cross-phase modulation. A Gaussian best fit of the measured spectra gives a FWHM of 0.88 and 0.77 nm, for 1.2 W and 0.1 W IR pumping respectively. This indicated that SPM and XPM are indeed negligible in our case, despite the peak intensity of focused pump and probe pulses achieved the considerable value of $\approx 100 \text{ GW/cm}^2$. The measured value of 0.88 nm for the FWHM of the pulse spectrum yields a $\tau_p^{(F)} \approx 110 \text{ fs}$, which is less than half the $\tau_p^{(0)}$ value, demonstrating that the pulse is consistently chirped. In fact, it is well known that the occurrence of chirp leads to a duration-bandwidth product exceeding the Fourier limit by a factor $\sqrt{1 + a^2}$ [30], with the “ a ” parameter given, in terms of pulse durations, by:

$$a = \sqrt{\left(\frac{\tau_p^{(0)}}{\tau_p^{(F)}}\right)^2 - 1} \approx 1.97. \quad (5.4)$$

By assuming a Gaussian temporal shape of the chirped pulse:

$$E(t) \propto \exp\left\{-2\ln 2(1 + ia)\frac{t^2}{\tau_p^{(0)^2}}\right\} = \exp\left\{-2\ln 2\frac{t^2}{\tau_p^{(0)^2}} + i(\omega_0 t + \alpha t^2)\right\} \quad (5.5)$$

ω_0 being the pulse carrier angular frequency, we can work out the overall chirp coefficient, α :

$$\alpha = \frac{2\ln 2 \cdot a}{\tau_p^{(0)^2}} \approx 4.7 \times 10^{-5} \text{ fs}^{-2}. \quad (5.6)$$

To determine the origin of the chirp, we first checked that the IR fundamental pulse is indeed chirp-free, thereby finding that the chirp actually occurs into the harmonic generator module. Here the initial IR pulse is first frequency doubled passing through a 0.8 mm thick BBO nonlinear crystal; then, the resulting 2nd harmonic is converted into the 4th harmonic in a second 0.4 mm thick BBO crystal. It is important for our aim to work out the so-called nonlinear interaction length, L_{NL} , and the dispersion length, L_D^{SHG} for the two nonlinear stages. The former represents the length of the nonlinear crystal such that depletion of the fundamental pulse for conversion into 2nd harmonic becomes non-negligible, whereas the latter indicates the length of the crystal beyond which the walk-off between second harmonic and fundamental pulses, owing to different group velocities, becomes non-negligible. These lengths are defined as [122, 126]:

$$L_{NL} = \frac{2n(\omega)c}{\omega\chi^{(2)}(\omega)E_0} \quad \text{and} \quad L_D^{SHG} = \frac{\tau_{IN}}{|v_2^{-1} - v_1^{-1}|} \quad (5.7)$$

where $n(\omega)$ and $\chi^{(2)}(\omega)$ are the refractive index and the 2nd order susceptibility of the crystal, respectively; E_0 and τ_{IN} stands for the input electric field amplitude and duration, respectively; v_1 and v_2 are the group velocities of fundamental and 2nd harmonic, respectively. By using the values for $n(\omega)$ and $\chi^{(2)}(\omega)$ of the BBO that can be found in the literature [127], and a group velocity mismatch, $v_2^{-1} - v_1^{-1}$, of 100 fs/mm and 680 fs/mm for the 1st and 2nd doubling stage [30 and references therein], respectively, we estimate for the two stages the values of L_{NL} and L_D^{SHG} , normalized to each crystal length, given in Table 5.1:

	L_{NL}/L	L_D^{SHG}/L
I stage	≈ 0.3	≈ 2.13
II stage	≈ 1.31	≈ 0.63

Table 5.1: Estimated values of the nonlinear, L_{NL} , and dispersive, L_D^{SHG} , lengths normalized to the length of each nonlinear crystal of the doubling stage.

Interestingly, in the first doubling stage the group velocity mismatch can be neglected whereas the nonlinear interaction length is approximately one third of the crystal length. In this condition the fundamental IR pulse is depleted significantly within the 0.8-mm BBO thickness. No parametric back-conversion is possible for a transform limited pulse [126]; therefore, the BBO generates, in this case, chirped SH pulses having nearly the same temporal pulse profile and duration of the pumping pulses. We can, then, assume that the second harmonic pulse, centered at 515, lasts approximately as the IR pulse, i.e. $\tau_{II} \approx 170$ fs, and is also chirped, the resulting chirp being essentially due to SHG in the saturation regime:

$$a_{I \text{ stage}} = \sqrt{\left(\frac{\tau_{II}}{\tau_p^{(F)}}\right)^2 - 1} \approx 1.18. \quad (5.8)$$

In the 2nd stage, instead, $L_{NL} > L$ and $L_D^{SHG} < L$. This implies that, due to a strong group velocity mismatch typical of UV pulse propagation, an additional pulse lengthening of ≈ 70 fs is generated in the second stage corresponding to an additional chirp of:

$$a_{II \text{ stage}} \approx \sqrt{\left(\frac{\tau_p^{(0)}}{\tau_{II}}\right)^2 - 1} \approx 0.65. \quad (5.9)$$

5.5. Spectral characterization

We also characterized some interesting spectral features of the probe transmitted through the sample. In Figure 5.5 we report as a function of the delay between pump and probe the spectral FWHM of the probe (a) normalized to its value in absence of the pump pulse, and the centre of gravity of the probe spectrum (b). Interestingly, both quantities are modulated versus the time delay between pump and probe.

The FWHM is first narrowed by $\approx 2.5\%$ compared to that of the probe in absence of the pump for negative delay, i.e. when the probe comes first, then it is broadened by $\approx 8\%$ when the time delay is zero and pump and probe are perfectly overlapped, to be again narrowed by $\approx 5\%$ when the pump comes ahead. We attribute this behavior to the interplay between the chirp of the incoming pulse and SPM and XPM induced in the nonlinear medium when pump and probe are temporally overlapped and the overall intensity reaches its highest value. In fact, when the probe comes first (negative delay), due to the chirp of the pulses, the overlap is realized between the probe blue trailing and pump red leading edge. One photon per each pump and probe pulse constitutes the event contributing to the TPA signal. Since TPA favors the absorption of photons having the same frequency [119], and the pump is more intense than the probe in the 2:1 ratio, we can conclude that more photons on the red side of the spectral bandwidth are absorbed in this case, resulting in a narrowed transmitted spectrum. For zero delay between pump and probe each frequency component can be equally absorbed to contribute to TPA, but SPM and XPM due to higher overall intensity reached into the quartz give a nearly symmetric spectral broadening which, in fact, is in good agreement with that reported in Figure 5.4 for the incoming pulse.

Finally, when the pump comes ahead and the time delay is positive, again a spectrally selective absorption mechanism has to be invoked working the other way round compared to negative delay, and leading to a narrowing mechanism similar to that occurring for negative delay.

This interpretation is perfectly coherent with the results reported in Figure 5.5 (b). In fact, for negative delays we observe a blue shift of the transmitted probe spectrum, in agreement with the argument of the spectrally selective absorption induced by the chirp. When $t_d = 0$ the selective absorption is not working anymore: as a consequence no shift is observed, whereas a red shift is observed for $t_d > 0$.

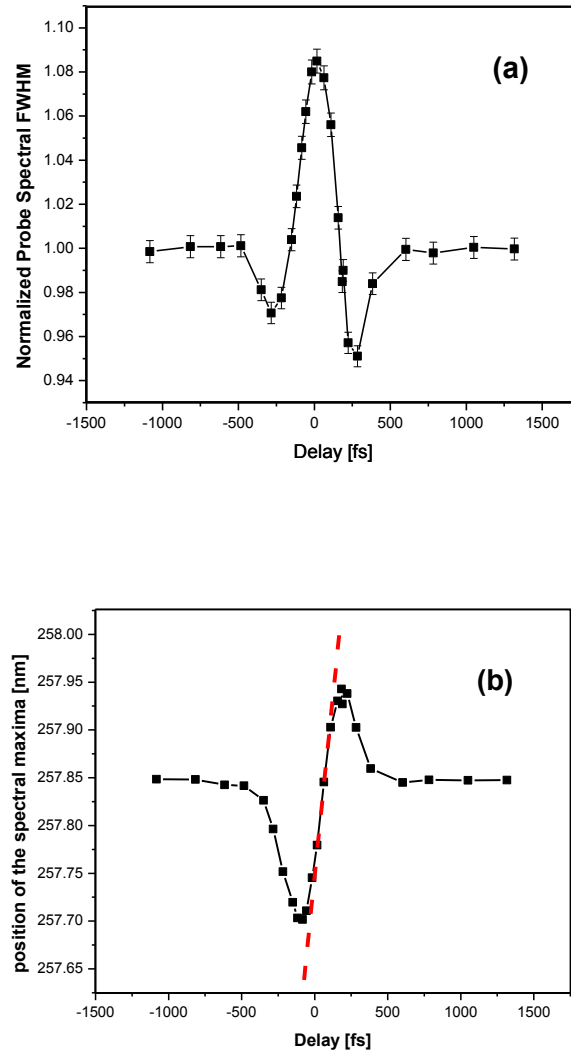


Figure 5.5: (a) Normalized FWHM of the probe spectrum versus time delay and (b) Position of the spectral maximum of the probe spectrum versus time delay. The red dashed straight line corresponds to the curve slope at $t_d = 0$.

As $2\alpha t/\omega_0 \ll 1$, it is easy to define an instantaneous wavelength for the chirped pulse, $\lambda(t)$, as:

$$\lambda(t) \approx \lambda_0 \left(1 - \frac{2\alpha t}{\omega_0} \right) \quad (5.10)$$

$\lambda_0 = 257.85$ nm being the pulse carrier wavelength. Therefore, by estimating the slope of the transmitted spectral peak at $t_d = 0$, and reminding the conversion factor between actual time appearing in the pulse duration and time delay between the two pulses to be $dt = dt_d/\sqrt{2}$, we can retrieve the chirp coefficient to give:

$$\alpha \approx 3.2 \times 10^{-5} \text{ fs}^{-2} \quad (5.11)$$

This estimate of α is in fairly good agreement with what found in Eq. (6). The underestimation of the α value in Eq. (5.11) is to be attributed to the effect of SPM and XPM which symmetrically broaden the bandwidth around $t_d = 0$ and partly cover the spectral shift of the transmitted spectrum induced by the initial chirp.

We also stress that this new way to estimate the chirp of the pulse does not require the combined measurement of the autocorrelation and pulse spectrum.

5.6. Linear optical methods for characterization of femtosecond UV pulses

We split UV pulses into two replica by means of a polarized beam splitter. The incoming polarization is selected by a half-wave plate (WP) to have the same intensity in the two beams. One of the pulses is reflected by the mirrors on our motorized translation stage (DL) in order to control the relative delay between the two pulses.

These two beams are then guided to hit a UV-sensitive CCD in a nearly collinear configuration, forming an angle of about 2 degrees. They spatially overlap on the CCD and when the pulses are also superimposed in time, they generate an interference pattern as shown in figure 5.6.

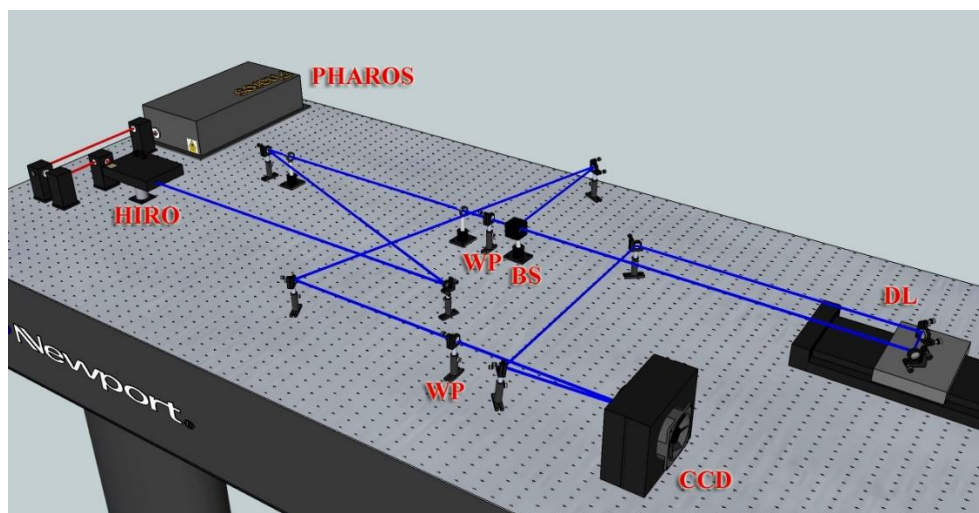


Figure 5.6: Scheme of the realized first-order interferometric autocorrelator for UV femtosecond pulses.

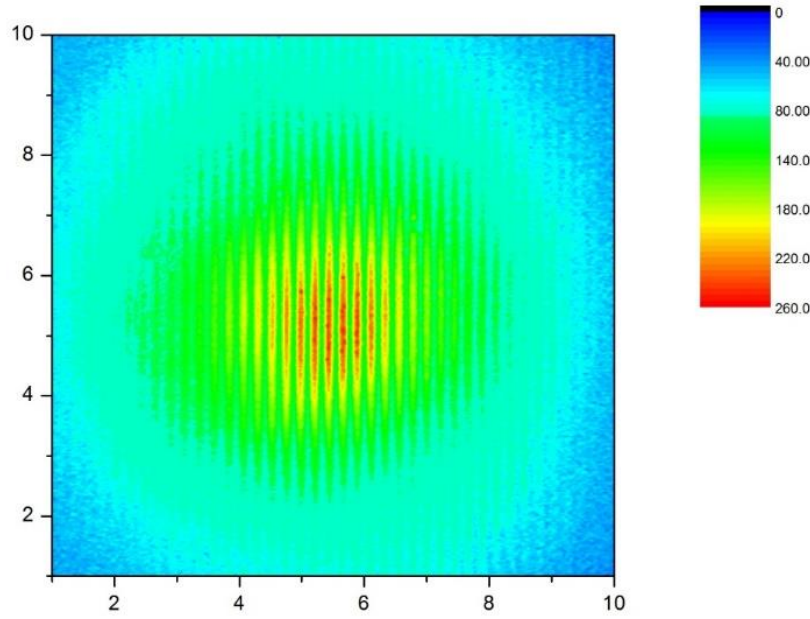


Figure 5.7: Typical interference pattern of 257-nm femtosecond pulses captured by the UV-sensitive CCD.

The measured visibility in the interference pattern as a function of the delay between the two pulses gives the coherence length of the pulses [122], but also can be used to retrieve the minimum pulse duration, i.e. the duration Fourier limit, being equivalent to measuring the pulse spectrum [122, 128]. The visibility is defined as:

$$\text{Visibility} = \frac{I_{\max} - I_{\min}}{I_{\max} + I_{\min}} \quad (5.12)$$

The intensity gradient $I_{\max} - I_{\min}$ can be either measured by selecting a single spatial point in the wavefront and finely changing τ within an optical cycle of the pulse, or can be evaluated at fixed delay by considering the spatial modulation of the intensity along the wavefront, which are due to change in the optical path of the two interfering beams. While the first method demands for subcycle temporal resolution of the delay line, the latter, which we setup, requires a UV-sensitive CCD with a suitable spatial resolution.

Then, the visibility of the interference pattern can be estimated from the spatial maxima and minima of the measured intensity for each delay. To this purpose we extract from the 2D interferogram (figure 5.7) the only horizontal projection (see figure 7.8) corresponding to the center of the pattern as we measure there the best contrast.

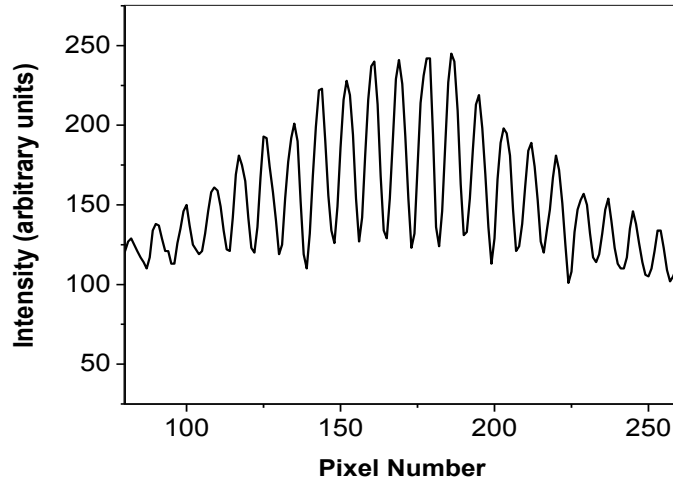


Figure 5.8: Intensity of the interference pattern along its horizontal diameter.

It is worth mentioning that we observe a visibility of approximately 0.3 – 0.4 which matches the 2:1 realized ratio in peak intensity of the two interfering pulses. Then, a few central cycles of such oscillation, where the amplitude of the oscillation is almost constant, can be fitted with a sine function of the form $I(x) = y_0 + A \cdot \sin(x)$, as shown in figure 5.9. The maximum and minimum intensities can be deduced from the fitting procedure. In this case, for instance:

$$y_0 = 186.26 \quad \text{and} \quad A = 56.56$$

$$I_{\max} = 186.26 + 56.56 = 242.82 \quad \text{and} \quad I_{\min} = 186.26 - 56.56 = 129.7$$

$$\text{Visibility} = \frac{242.82 - 129.7}{242.82 + 129.7} \approx 0.30 \quad (5.13)$$

The estimated uncertainty of the read visibility for each delay is typically 4-5 % as obtained by the fitting procedure.

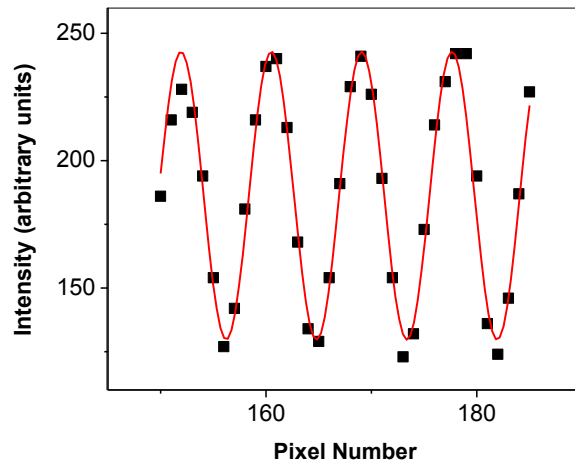


Figure 5.9: A few central oscillations of the waveform represented in figure 5.8 and (red bold line) the sine-like best-fit.

The measured visibility as a function of the delay between the two pulses is reported in figure 5.10 along with its Gaussian fit. The FWHM of this Gaussian is 222 ± 20 fs; and to retrieve the pulse duration, assumed a Gaussian form for the amplitude of the electric field, we get 111 ± 10 fs. We remind here, indeed that when measuring the first-order autocorrelation function (amplitude autocorrelation) of Gaussian pulses the FWHM of the final pulse is half the FWHM of the autocorrelation.

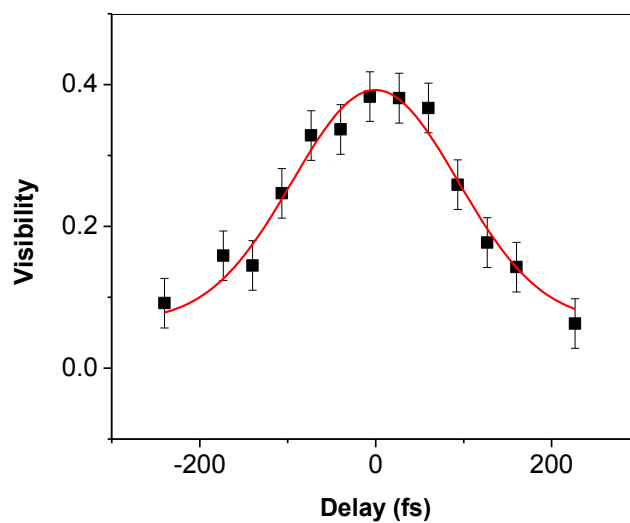


Figure 5.10: Visibility as a function of the delay and corresponding Gaussian best-fit (red bold line).

Conclusions

The motivation for the research reported in this thesis relies in the importance of understanding the molecular mechanism leading to covalent bond (cross-link) formation between DNA and protein. In fact, DNA-protein cross-link is a fundamental process in molecular biology to identify the partners in the interactions between DNA and protein. Thus, in a reductionist approach we chose a model system like 5-benzyluracil (5BU) to mimic the proximity of the DNA base to the protein. In this scheme uracil and benzene play the role of the DNA base and the aromatic residue of a protein, respectively, whereas the cross-link is given by the cyclization of 5BU which leads to 5,6BU.

In agreement with the previous literature, we measured the quantum yield of the UV induced photocyclization (QY_{ph}) of 5BU finding a value of 2.1×10^{-3} when 5BU is dissolved in methanol. A significantly higher value of $QY_{ph} = 1.4 \times 10^{-2}$ has been found when methanol has been replaced by water demonstrating the role of the molecular conformation in the photocyclization process. The steady-state spectroscopic characterization of 5BU and 5,6BU has been carried out in view of the design of a future experiment aimed at capturing the photocyclization dynamics. We have observed that both absorption and fluorescence of 5BU and 5,6BU differ quite enough so that either of the two may be considered for pump-probe

experiment. For both species the measured spectra are in agreement with the theoretical calculation.

Given the low QY_{ph} there is a question about the competing relaxation channels of the excited 5BU other than those leading to 5,6BU. Thus, we have characterized the fluorescence of 5BU in the nanosecond range by means of a standard technique (Time Correlated Single Photon Counting) finding the presence of ultrashort fluorescence lifetime, which could only be measured by a more sophisticated technique like fluorescence up-conversion. Given the short wavelength range of the 5BU fluorescence (300 to 360 nm), such an experiment has been carried out at the unique facility available in the Laboratory of Ultrafast Spectroscopy at EPFL (École polytechnique fédérale de Lausanne), providing a value for the 5BU fluorescence lifetime of 0.5 and 0.8 picoseconds for its two emission bands at around 315 and 350 nm, respectively.

The need to use femtosecond pulses in the UV range has required a somehow unconventional technique for their characterization. Thus, we have temporally characterized a relatively high-energy chirped femtosecond pulses in the Naples lab by setting up a simple, cheap, and quick autocorrelator based on two photon absorption in a fused silica window. The measurements have revealed that such a method is capable to provide an accurate measurement of the UV pulse duration; and that, when coupled with the measurement of the UV pulse spectrum, it is possible to extract also the pulse chirp. With this as well as with the spectroscopic characterizations performed in this thesis a pump-probe experiment, which will disclose the photocyclization process, can be eventually be designed.

Bibliography

- [1] Markus Sauer, Johan Hofkens, and Jörg Enderlein, Handbook of Fluorescence Spectroscopy and Imaging From Single Molecules to Ensembles, 2011 WILEY-VCH, ISBN: 978-3-527-31669-4
- [2] Bernard Valeur; Molecular Fluorescence: Principles and Applications; 2001 Wiley-VCH Verlag GmbH; ISBNs: 3-527-29919-X
- [3] Joseph R. Lakowicz; Principles of Fluorescence Spectroscopy; 2006, Springer; ISBN-10: 0-387-31278-1
- [4] Robert Boikess, Rutgers; Chemical Principles for Organic Chemistry, 1st Edition, the State University of New Jersey, ISBN-10: 1285457692
- [5] Frank Jensen; Introduction to Computational Chemistry, John Wiley & Sons Ltd, 2007; ISBN-13 978-0-470-01186-7
- [6] Kang, Hyuk; Kang Taek Lee; Boyong Jung; Yeon Jae Ko; Seong Keun Kim;. J. Am. Chem. Soc. 124 (44)
- [7] Pfeifer GP, You Y-H, Besaratinia A. 2005. Mutations induced by ultraviolet light. Mutat. Res. 571:19–31
- [8] De Gruijl FR. 1999. Eur. J. Cancer 35:2003–9

- [9] Crespo-Hernández CE, Cohen B, Hare PM, Kohler B. 2004. *Chem. Rev.* 104:1977–2019
- [10] Voet D, Gratzer WB, Cox RA, Doty P. 1963. *Biopolymers* 1:193–208
- [11] Callis PR. 1983. *Annu. Rev. Phys. Chem.* 34:329–57
- [12] Daniels M, Hauswirth W. 1971. *Science* 171:675–77
- [13] Vigny P. 1971. *C. R. Acad. Sci. Ser. D* 272:3206–9
- [14] Pecourt J-ML, Peon J, Kohler B. 2000. *J. Am. Chem. Soc.* 122:9348–49
- [15] Ismail N, Blancafort L, Olivucci M, Kohler B, Robb MA. 2002. *J. Am. Chem. Soc.* 124:6818–19
- [16] Shukla MK, Leszczynski J. 2007. *J. Biomol. Struct. Dyn.* 25:93–118
- [17] Langer H, Doltsinis NL, Marx D. 2005. *ChemPhysChem* 6:1734–37
- [18] Barbatti M, Lischka H. 2007. *J. Phys. Chem. A* 111:2852–58
- [19] Hudock HR, Levine BG, Thompson AL, Satzger H, Townsend D, et al. 2007. *J. Phys. Chem. A* 111:8500–8
- [20] Groenhof G, Schafer LV, Boggio-Pasqua M, Goette M, Grubmuller H, Robb MA. 2007. *J. Am. Chem. Soc.* 129:6812–19
- [21] Matsika S. 2004. *J. Phys. Chem. A* 108:7584–90
- [22] Perun S, Sobolewski AL, Domcke W. 2006. *J. Phys. Chem. A* 110:13238–44
- [23] Merchán M, González-Luque R, Climent T, Serrano-Andrés L, Rodríguez E, et al. 2006. *J. Phys. Chem. B* 110:26471–76
- [24] Gustavsson T, Banyasz A, Lazzarotto E, Markovitsi D, Scalmani G, et al. 2006. *J. Am. Chem. Soc.* 128:607–19
- [25] Perun S, Sobolewski AL, Domcke W. 2005. *J. Am. Chem. Soc.* 127:6257–65
- [26] Serrano-Andrés L, Merchán M, Borin AC. 2006. *Proc. Natl. Acad. Sci. USA* 103:8691–96
- [27] Crespo-Hernandez, C. E.; Cohen, B.; Hare, P. M.; Kohler, B. *Chem. Rev.* 2004, 104, 1977-2020
- [28] Peon, J.; Zewail, A. H. *Chem. Phys. Lett.* 2001, 348, 255-262

- [29] Gustavsson, T.; Sharonov, A.; Markovitsi, D. *Chem. Phys. Lett.* 2002, 351, 195-200
- [30] Gustavsson, T.; Sharonov, A.; Onidas, D.; Markovitsi, D. *Chem. Phys. Lett.* 2002, 356, 49-54
- [31] Onidas, D.; Markovitsi, D.; Marguet, S.; Sharonov, A.; Gustavsson, T. *J. Phys. Chem. B* 2002, 106, 11367-11374
- [32] Sharonov, A.; Gustavsson, T.; Carre', V.; Renault, E.; Markovitsi, D. *Chem. Phys. Lett.* 2003, 380, 173-180
- [33] Fujiwara, T.; Kamoshida, Y.; Morito, R.; Yamashita, M. *J. Photochem. Photobiol. B: Biol.* 1997, 41, 114-121
- [34] Pecourt, J.-M. L.; Peon, J.; Kohler, B. J. *Am. Chem. Soc.* 2001, 123, 10370- 10378
- [35] Pal, S. K.; Peon, J.; Zewail, A. H. *Chem. Phys. Lett.* 2002, 363, 57-63
- [36] Sharonov, A.; Gustavsson, T.; Marguet, S.; Markovitsi, D. *Photochem. Photobiol. Sci.* 2003, 2, 1-5
- [37] Malone, R. J.; Miller, A. M.; Kohler, B. *Photochem. Photobiol.* 2003, 77, 158
- [38] Cohen, B.; Crespo-Hernandez, C. E.; Kohler, B. J. *Chem. Soc., Faraday Discuss.* 2004, 127, 137-147
- [39] Brady, B. B.; Peteanu, L. A.; Levy, D. H. *Chem. Phys. Lett.* 1988, 147, 538-543
- [40] Marian, C. M.; Schneider, F.; Kleinschmidt, M.; Tatchen, J. *Eur. Phys. J., D: Atom., Mol. Opt. Phys.* 2002, 20, 357-367
- [41] Improta, R.; Barone, V. *J. Am. Chem. Soc.* 2004, 126, 14320-14321
- [42] Matsika, S. J. *Phys. Chem. A* 2004, 108, 7584-7590
- [43] Saigusa H. 2006. *J. Photochem. Photobiol. C* 7:197-210
- [44] de Vries MS, Hobza P. 2007. *Annu. Rev. Phys. Chem.* 58:585-612
- [45] Fischer I. 2003. *Chem. Soc. Rev.* 32:59-69
- [46] Markovitsi D, Gustavsson T, Talbot F. 2007. *Photochem. Photobiol. Sci.* 6:717-24
- [47] Canuel C, Mons M, Piuze F, Tardivel B, Dimicoli I, Elhanine M. 2005. *J. Chem. Phys.* 122:074316

- [48] Blancafort L. 2007. *Photochem. Photobiol.* 83:603–10
- [49] Marian CM. 2005. *J. Chem. Phys.* 122:104314
- [50] Satzger H, Townsend D, Zgierski MZ, Patchkovskii S, Ullrich S, Stolow A. 2006. *Proc. Natl. Acad. Sci. USA* 103:10196–201
- [51] Hare PM, Crespo-Hernández CE, Kohler B. 2007. *Proc. Natl. Acad. Sci. USA* 104:435–40
- [52] Hare PM, Crespo-Hernández CE, Kohler B. 2006. *J. Phys. Chem. B* 110:18641–50
- [53] Middleton CT, Cohen B, Kohler B. 2007. *J. Phys. Chem. A* 111:10460–67
- [54] Cohen B, Hare PM, Kohler B. 2003. *J. Am. Chem. Soc.* 125:13594–601
- [55] Kuimova MK, Dyer J, George MW, Grills DC, Kelly JM, et al. 2005. *Chem. Commun.* 2005:1182–84
- [56] Quinn S, Doorley GW, Watson GW, Cowan AJ, George MW, et al. 2007. *Chem. Commun.* 2007:2130–32
- [57] Hare PM, Middleton CT, Mertel KI, Herbert JM, Kohler B. 2008. *Chem. Phys.* 347:383–92
- [58] Nibbering ETJ, Fidler H, Pines E. 2005. *Annu. Rev. Phys. Chem.* 56:337–67
- [59] Chris T. Middleton, Kimberly de La Harpe, Charlene Su, Yu Kay Law, Carlos E. Crespo-Hernández,² and Bern Kohler; *Annu. Rev. Phys. Chem.* 2009. 60:217–39
- [60] Cadet J, Vigny P. 1990. The photochemistry of nucleic acids. In *Bioorganic Photochemistry*, ed. HMorrison, pp. 1–272. New York:Wiley
- [61] Salet C, Bensasson R, Becker RS. 1979. *Photochem. Photobiol.* 30:325–29
- [62] Merchán M, Serrano-Andrés L, Robb MA, Blancafort L. 2005. *J. Am. Chem. Soc.* 127:1820–25
- [63] Climent T, González-Luque R, Merchán M, Serrano-Andrés L. 2007. *Chem. Phys. Lett.* 441:327–31
- [64] Meisenheimer, K. M.; Koch, T. H. *Crit. Rev. Biochem. Mol. Biol.* 1997, 32 (2), 101-140
- [65] Wang, W. Y. *Photochemistry and Photobiology of the Nucleic Acids*; Wiley: New York, 1976

- [66] Morrison, H. *Bioorganic Photochemistry*; Wiley: New York, 1990
- [67] Shetlar, M. D. *Frontiers of Photobiology*; International Congress Series, 1993, 1021, 67-72 and references therein
- [68] Russmann, C.; Stollhof, J.; Weiss, C.; Beigang, R.; Beato, M. *Nucl. Acids Res.* 1998, 26, 3967-3970
- [69] Guangxing Sun, Christopher J. Fecko, Robert B. Nicewonger, Watt W. Webb, and Tadhg P. Begley; *ORGANIC LETTERS*, 2006, Vol. 8, No. 4, 681-683
- [70] Barker, S.; Weinfeld, M.; Murray, D. *Mutat. Res.* 2005, 589, 111-135
- [71] Jean-Ruel, H.; Cooney, R. R.; Gao, M.; Lu, C.; Kochman, M. A.; Morrison, C. A.; Miller, R. J. D.; *J. Phys. Chem. A* 2011, 115, 13158-13168
- [72] Aldoshin, S. M.; Yur'eva, E. A.; Sanina, N. A.; Krayushkin, M. M.; Tsyganov, D. V.; Gostev, F. E.; Shelaev, I. V.; Sarkisov, O. M.; Nadtochenkoa, V. A.; *Russ. Chem. Bull. Int. Ed.* 2011, 60, 1118-1127
- [73] Siewertsen, R.; Renth, F.; Temps, F.; Sönnichsen, F. *Parallel*; *Phys. Chem. Chem. Phys.* 2009, 11, 5952-5961
- [74] Natali, M.; Giordani, S.; *Chem. Soc. Rev.* 2012, 41, 4010-4029
- [75] Kistler, K. A.; Matsika, S. T.; *J. Chem. Phys.* 2008, 128, 215102
- [76] Micciarelli, M.; Altucci, C.; Della Ventura, B.; Velotta, R.; Toşa, V.; Pérez, A. B. G.; Rodríguez, M. P.; de Lera, A. R.; Bende, A. *Phys. Chem. Chem. Phys.* 2013, 15, 7161-7173
- [77] Improta, R.; Barone, V.; *J. Am. Chem. Soc.* 2004, 126, 14320-14321
- [78] Markovitsi, D.; Gustavsson, T.; Banyasz, A.; *Mutat. Res.* 2010, 704, 21-28
- [79] Barbatti, M.; Aquino, A. J. a; Szymczak, J. J.; Nachtigallová, D.; Hobza, P.; Lischka, H.; *Proc. Natl. Acad. Sci. U. S. A.* 2010, 107, 21453-21458
- [80] Valeur, B. *Molecular Fluorescence: Principles and Applications*; Wiley-VCH Verlag GmbH: Weinheim, 2001; pp. 353-355
- [81] Lakowicz, J. R. *Principles of Fluorescence Spectroscopy*; Third Edit.; Springer: New York, 2006
- [82] Daniels, M.; Hauswirth, W. *Science* 1971, 171, 675-677

- [83] M. Micciarelli, M. Valadan, B. Della Ventura, G. Di Fabio, L. De Napoli, S. Bonella, U. Rothlisberger, I. Tavernelli, C. Altucci, R. Velotta; *The Journal of Physical Chemistry*; 118, 4983–4992; (2014)
- [84] Santoro F, Barone V, Gustavsson T, Improta R (2006) *J Am Chem Soc* 128:16312
- [85] Banyasz A, Karpati S, Mercier Y, Reguero M, Gustavsson T, Markovitsi D, Improta R (2010) *J Phys Chem B* 114:12708
- [86] Gustavsson T, Banyasz A, Lazzarotto E, Markovitsi D, Scalmani G, Frisch MJ, Barone V, Improta R (2006) *J Am Chem Soc* 128:607
- [87] Mercier Y, Santoro F, Reguero M, Improta R (2008) *J Phys Chem B* 112:10769
- [88] Gustavsson T, Sarkar N, Lazzarotto E, Markovitsi D, Barone V, Improta R (2006) *J Phys Chem B* 110:12843
- [89] O'Connor, D.V.O., Phillips, D., "Time-correlated Single Photon Counting", Academic Press, London, 1984.
- [90] O'Connor, D.V.O., Ware, W.R., Andre, J.C. , *J. Phys. Chem.* 83, 1333-1343, 1979
- [91] D. J. Nesbitt and R. W. Field, *Journal of Physical Chemistry* 100 (31), 12735 (1996)
- [92] B. Bagchi and B. Jana, *Chemical Society Reviews* 39 (6), 1936 (2010)
- [93] A. H. Zewail, *Journal of Physical Chemistry A* 104 (24), 5660 (2000)
- [94] S. A. Kovalenko, A. L. Dobryakov, J. Ruthmann, and N. P. Ernsting, *Physical Review A* 59 (3), 2369 (1999)
- [95] B. Schmidt, S. Laimgruber, W. Zinth, and P. Gilch, *Applied Physics B-Lasers and Optics* 76 (8), 809 (2003)
- [96] P. Fita, Y. Stepanenko, and C. Radzewicz, *Applied Physics Letters* 86 (2) (2005)
- [97] 299 J. Shah, *Ieee Journal of Quantum Electronics* 24 (2), 276 (1988)
- [98] R. Schanz, S. A. Kovalenko, V. Kharlanov, and N. P. Ernsting, *Applied Physics Letters* 79 (5), 566 (2001)
- [99] L. J. Zhao, J. L. P. Lustres, V. Farztdinov, and N. P. Ernsting, *Physical Chemistry Chemical Physics* 7 (8), 1716 (2005)
- [100] H. R. Schanz, Humboldt-Universität zu Berlin, 2002

- [101] D. F. Zernike and J. E. Midwinter, *Applied Nonlinear Optics*. (Wiley, New York, 1973)
- [102] G. Zgrablic, Ecole Polytechnique Fédérale de Lausanne, 2006
- [103] O. Bräm, Ecole Polytechnique Fédérale de Lausanne, 2006
- [104] A. Cannizzo, O. Bram, G. Zgrablic, A. Tortschanoff, A. A. Oskouei, F. van Mourik, and M. Chergui, *Optics Letters* 32 (24), 3555 (2007)
- [105] C. Homann, N. Krebs, and E. Riedle, *Appl. Phys. B* 104, 783-791 (2011)
- [106] N. Krebs, R. A. Probst, and E. Riedle, *Opt. Expr.* 18, 6164-6171 (2010)
- [107] C. Homann, P. Lang, and E. Riedle, *J. Opt. Soc. Am. B* 29, 2765-2769 (2012)
- [108] P. Baum, S. Lochbrunner, and E. Riedle, *Appl. Phys. B* 79, 1027-1032 (2004)
- [109] B. Zhao, Y. Jiang, K. Sueda, N. Miyanaga, and N. Kobayashi, *Opt. Expr.* 17, 17711-17714 (2009)
- [110] A. E. Jailaubekov and S. E. Bradforth, *Appl. Phys. Lett.* 87, 021107 (2005)
- [111] J. Möhring, T. Buckup, and M. Motzkus, *Opt. Lett.* 35, 3916-3918 (2010)
- [112] S. Backus, J. Peatross, Z. Zeek, A. Rundquist, G. Taft, M. M. Murnane, and H. C. Kapteyn, *Opt. Lett.* 21, 665-667 (1996)
- [113] D. J. Kane, A. J. Taylor, R. Trebino, and K. W. DeLong, *Opt. Lett.* 19, 1061-1063 (1994)
- [114] D. N. Nikogosyan and D. A. Angelov, *Chem. Phys. Lett.* 77, 208-210 (1981)
- [115] A. Dragomir, J. G. McInerney, D. N. Nikogosyan, and A. A. Ruth, *IEEE J. of Quantum Elec.* 38, 31-36 (2002)
- [116] J. I. Dadap, G. B. Focht, D. H. Reitze, M. C. Downer, *Opt. Lett.* 16, 499-501 (1991)
- [117] A. Dragomir, J. G. McInerney, and D. N. Nikogosyan *Appl. Opt.* 8, 4365-4376 (2002)
- [118] S. A. Kovalenko, A. L. Dobryakov, J. Ruthmann, and N. P. Ernsting, *Phys. Rev. A* 59, 2369-2384 (1999)
- [119] I. Kang, S. Smolorz, T. Krauss, and F. Wise, B. G. Aitken, and N. F. Borrelli, *Phys. Rev. B* 54, R12641-R12644 (1996)
- [120] the producer website, <http://www.lightcon.com/>

- [121] <http://www.atlas-eu.com/index.html>
- [122] J.-C. Diels and W. Rudolph, "Ultrashort Laser Pulse Phenomena," Elsevier, 2nd Edition, 3rd Chapter (2006)
- [123] R. Hellwarth, J. Cherlow, and T-T. Yang, *Phys. Rev. B* 11, 964-967 (1975)
- [124] J. Kasparian and J.-P. Wolf, *Opt. Expr.* 16, 466-493; 2008; and references therein
- [125] C. Altucci, A. Nebbioso, R. Benedetti, R. Esposito, V. Carafa, M. Conte, M. Micciarelli, L. Altucci, and R. Velotta, *Laser Phys. Lett.* 9, 234-239 (2012)
- [126] J.-y Zhang, J. Y. Huang, H. Wang, K. S. Wong, and G. K. Wong, *J. Opt. Soc. Am. B* 15, 200-209 (1998)
- [127] D. N. Nikogosyan, *Appl. Phys. A* 52, 359-368 (1991)
- [128] Trebino, R., "Frequency_resolved Optical Gating: The Measurement of Ultrashort Laser Pulses," Springer, (2000)